



**Università
degli Studi
di Ferrara**

**DOTTORATO DI RICERCA IN
"SCIENZE DELL'INGEGNERIA"**

CICLO XXXII

COORDINATORE Prof. Stefano Trillo

**Numerical approaches to the study of organic
Rankine cycle systems for decentralized applications**

Settore Scientifico Disciplinare ING-IND/08

Dottorando

Dott. Randi Saverio

(firma)

Tutore

Prof. Pinelli Michele

(firma)

Anni 2016/2019

Abstract

Organic Rankine Cycle systems (ORCs) are a well-known technology to obtain useful work from energy sources whose temperature and thermal power are too low for being exploited with conventional steam Rankine cycles: this is possible because water is replaced by an organic fluid, which is characterized by a lower ebullition temperature, allowing its vaporization and consequent expansion for smaller thermal inputs. Because of this, ORCs make it possible to generate power from a broad series of heat sources, such as low-temperature, renewable energy ones (as in geothermal and solar fields), industrial processes in which hot streams are present and heat rejected by engines through their flue gases. ORCs can also be used for heat and power applications meaning that, in addition to the electrical energy, also the low-grade heat rejected by the cycle (e.g. at the condenser) is used, for example for district heating or just to warm a single flat or house. When the user requires a limited power output, or when the heat source thermal power is limited, micro-scale ORCs have to be used, which are characterized by an electrical power output in the order of 10 kWe and, with respect to the systems of greater size, pose additional issues in terms of choice of the cycle layout, of the components and of the working fluid since manufacturing and maintenance costs have to be kept the lowest possible to allow for an acceptable payback period. Given this, since a few components are specifically designed to operate in this power range, it is common to use off-the-shelf devices, like compressors used as expanders. Then, it would be useful to study the behavior of these single cycle components and their interaction when part of a micro-ORC system, especially when the thermal conditions vary during cycle operations, such as when the electrical load increases or the temperature of the heat source or the cold one decreases.

In this thesis, the study of the ORC technology has been conducted by focusing on those systems and their components which are to be used for power generation in the micro range. An approach based on numerical simulations of the main components of the cycle, as the expander and the heat exchangers, has been of great use to understand what are the main phenomena which affect the performance of an entire system, such as pressure pulsations of

the working fluid or its leakages inside the expander. It has been possible to observe this latter issue by working on an experimental micro-ORC test stand which has been operated to test the performances of a prototypal scroll expander: the heat source of the cycle was a hot stream of air, simulating engine flue gases, and the working fluid was circulated in the system by means of a prototype scroll pump.

Before showing the results of the numerical analysis of the single devices, an innovative approach of modeling via Computational Fluid Dynamics (CFD) simulations the behavior of an entire system is reported, since it can provide useful information about how the system layout or the working conditions of a given component can affect the operations of the other devices in the cycle. At first, an idealized cycle has been simulated to study the feasibility of the solution and then a portion of an ORC system has been discretized and the flow field characteristics computed. In those cases in which great computational resources are not available, another possibility has been investigated. By connecting the simulations of the single devices by means of a Python script, it is shown the feasibility of an approach in which the different parts of the system are simulated by means of different 3D CFD tools, allowing for different grid and solver set-up for each of these devices, and letting the behavior of a given component of being conveniently reflected on the one operating downstream of it.

Sommario

I cicli Rankine a fluido organico (ORC) sono una tecnologia che viene notoriamente utilizzata per ottenere lavoro utile da quelle fonti energetiche le cui temperatura e potenza termica sono troppo basse per poterle sfruttare con i convenzionali cicli Rankine: questo è possibile sostituendo l'acqua con un fluido organico, caratterizzato da un'inferiore temperatura di ebollizione che quindi ne consente la vaporizzazione e la conseguente espansione per input termici inferiori. Grazie a ciò, tramite il loro utilizzo è possibile ottenere potenza utile da sorgenti termiche come quelle rinnovabili (ad esempio solare e geotermico), processi industriali in cui flussi termici a bassa temperatura sono presenti così come i gas di scarico dei motori a combustione interna. Inoltre, sistemi ORC possono essere utilizzati per applicazioni cogenerative, in modo da poter fornire all'utilizzatore, oltre all'energia elettrica, anche il calore a bassa temperatura scartato dal ciclo a scopo, ad esempio, di riscaldamento domestico o distrettuale. Quando la potenza richiesta o quella disponibile sono limitate, vengono utilizzati i cicli ORC di taglia micro, caratterizzati da una potenza generata nell'ordine dei 10 kWe i quali, rispetto ai sistemi di taglia maggiore, pongono ulteriori vincoli in termini di scelta del layout d'impianto, tipo di componenti e fluido di lavoro, in quanto i costi di produzione e manutenzione devono essere ridotti il più possibile per consentire all'utente di ammortare le spese sostenute pur con tali valori di potenza generata. Per questo motivo, in tali sistemi è solito l'impiego di componenti non specificatamente progettati per queste applicazioni, come ad esempio compressori volumetrici usati come espansori. È pertanto interessante studiare il comportamento di suddetti componenti per questo utilizzo in condizioni fuori progetto, soprattutto durante i transitori.

In questa tesi, lo studio dei sistemi ORC è stato condotto focalizzandosi proprio sugli apparati di taglia micro; un approccio basato sullo sviluppo di simulazioni numeriche dei componenti principali del sistema, come espansore e scambiatori di calore, è stato utile per comprendere quali siano i fenomeni principali che condizionano le prestazioni di un intero ciclo, come ad esempio le pulsazioni di pressione del fluido di lavoro o le sue fughe all'interno dell'espansore. È stato possibile osservare soprattutto quest'ultimo aspetto

operando su un sistema prototipale ottimizzato per il recupero di energia dai gas di scarico di motori a combustione interna, adottante macchine di tipo scroll sia come espansore, sia come pompa.

Prima di mostrare i risultati numerici relativi all'analisi dei singoli componenti del ciclo, verrà riportato un approccio originale riguardante, tramite l'utilizzo dello strumento della fluidodinamica computazionale, la simulazione di un intero sistema. In questo modo, è possibile capire come il di questi layout o le condizioni operative di un certo componente influenzino il funzionamento degli altri componenti del ciclo. Per prima cosa, si è simulato un sistema idealizzato per verificare la fattibilità dell'approccio, poi una porzione di un sistema reale è stata discretizzata e di questa è stato determinato il campo di moto all'interno dei componenti. In quei casi in cui le risorse computazionali per svolgere questo tipo di simulazioni non siano disponibili, verrà proposto un ulteriore metodo d'analisi in cui le simulazioni fluidodinamiche dei singoli componenti sono state interfacciate fra loro tramite uno script Python, in modo tale da riflettere una variazione delle condizioni al contorno di un certo componente sul funzionamento di quello posto a monte o valle dello stesso.

Index

I.	Abstract.....	I
II.	Sommario.....	III
III.	Index	V
IV.	List of figures.....	IX
V.	List of tables	XV
1.	Why Organic Rankine Cycle systems	1
1.1	Introduction.....	1
1.2	ORC systems applications	3
1.2.1	Waste heat recovery.....	4
1.2.2	Combined heat and power	5
1.2.3	Solar fields.....	6
1.3	System layouts	7
1.3.1	Classic ORC	7
1.3.2	Recuperated ORC	8
1.3.3	Pumpless ORC.....	9
1.4	Cycle components.....	10
1.4.1	Heat exchangers.....	10
1.4.2	Expansion machines	14
1.4.3	Pumps	23
1.5	Working fluids	24
2.	An actual micro-ORC system.....	27
2.1	Introduction.....	27

2.2	Test stand characteristics	27
2.3	Instrumentation	28
2.4	Main components.....	29
2.4.1	Expander.....	29
2.4.2	Recuperator.....	30
2.4.3	Condenser and liquid receiver	31
2.4.4	Pump.....	32
2.4.5	Evaporator	32
2.5	Ancillary systems.....	33
2.5.1	Air stream (heat source)	33
2.5.2	Air stream (heat sink)	35
2.5.3	Pump electrical system	35
2.5.4	Expander electrical system	36
2.6	Results.....	37
3.	WOM approach	45
3.1	Introduction.....	45
3.2	WOM concept.....	50
3.2.1	Introduction to system modeling.....	50
3.2.2	Simulation set-up.....	51
3.2.3	Mesh and numerical model.....	53
3.2.4	Results	56
3.3	WOM development.....	59
3.3.1	From the concept to an actual application	59
3.3.2	Numerical model	61
3.3.3	Results: Pump behavior	66
3.3.4	Results: System behavior.....	70
4.	Analyses of the single components	77
4.1	Introduction.....	77

4.2	Study of the heat exchange inside a simplified evaporator.....	77
4.2.1	Numerical model	78
4.2.2	Results: Liquid mass fraction	80
4.3	Analysis of an oil-free scroll expander	82
4.3.1	Test stand.....	83
4.3.2	Numerical model	84
4.3.3	Results: CFD-calculations of pressure and velocity fields.....	87
4.4	Analysis of an Oldham-ring scroll expander	90
4.4.1	Numerical model	90
4.4.2	Results: Mass flow.....	94
4.4.3	Results: Pressure and velocity fields	96
4.5	Analysis of a lubricated single screw expander	99
4.5.1	Numerical model	100
4.5.2	Results: Inlet distributor	106
4.5.3	Results: Oil – rotor interaction	108
4.6	Analysis of an oil-free single screw expander	113
4.6.1	Numerical model	113
4.6.2	Results: Pressure field	115
4.6.3	Results: Flow field.....	118
5.	An alternative approach to Whole ORC Modeling	125
5.1	Introduction.....	125
5.2	Software employed	126
5.3	Python script	128
6.	Conclusions	131
VI.	Acknowledgements	XVII
VII.	References	XIX
VIII.	Appendix A – Python script.....	XXXI
IX.	Appendix B – Java script.....	XXXVII

List of figures

Figure 1: waste heat recovery from a truck engine [9].....	4
Figure 2: biomass-powered micro CHP system, from [12].....	6
Figure 3: solar-powered ORC system schematics, from [16]	7
Figure 4: standard ORC system. Left: system schematics, right: qualitative T-S diagram (from [17]).....	8
Figure 5: recuperated ORC system. Left: system schematics, right: qualitative T-S diagram (from [17]).....	9
Figure 6: variation of the power provided by the system as a function of time (from [20])	10
Figure 7: left: gasketed plate heat exchanger; right: detail of the gasket around a fluid port	11
Figure 8: plates, gaskets and leakages paths for a gasketed PHE (adapted from [23])	11
Figure 9: counterflow, 1 pass - 1 pass plate HE scheme (from [23]).....	12
Figure 10: tube-and-fin heat exchanger scheme (left, from [23]) and actual component (right)	13
Figure 11: microchannel heat exchanger model; on the left: magnification of microtubes	14
Figure 12: under-expansion (left) and over-expansion (right), from [29].....	16
Figure 13: disassembled scroll machine; stator (left), rotor (right).....	17
Figure 14: left to right: expansion process in a scroll expander, adapted from [28].....	18
Figure 15: screw machine; left: actual device; right: rotors profile (from [32])	19
Figure 16: single-screw machine layouts, adapted from [33]	20
Figure 17: single-screw expander: complete machine (left), screw and starwheels (from [35], right)	21
Figure 18: different piston expanders. Swashplate (top left), rotary (top right), gerotor (bottom left), rolling piston (bottom right).....	23

Figure 19: wet (top-left), isentropic (top-right) and dry (bottom) saturated vapor curves on a T-s diagram, from [46]	25
Figure 20: Herrick Labs micro-ORC system.....	27
Figure 21: Scroll expander	30
Figure 22: microchannel evaporator.....	33
Figure 23: left: air-flow amplifier, from [54]; right: actual device installed in the system.	34
Figure 24: 15-kW heat torch.....	34
Figure 25: condenser axial fan. Left: from manufacturer catalogue, right: as installed on the condenser	35
Figure 26: motor-pump assembly.....	36
Figure 27: from the left: pump motor inverter, 24 V DC power supply, braking transistor, expander motor inverter, heat torch controller	37
Figure 28: performance curves of the expander electrical motor – generator, from its datasheet [56].....	38
Figure 29: air mass flow rate for about 80 minutes of data acquisition	40
Figure 30: air mass flow rate for about 17 minutes of data acquisition	40
Figure 31: expander mechanical power as a function of expander	42
Figure 32: expander filling factor as a function of the expander rotational speed	43
Figure 33: Expander isentropic efficiency as a function of the expansion ratio	43
Figure 34: left: ORC system [66], right: P&I diagram.....	51
Figure 35: CFD model of the system presented in Figure 34.....	52
Figure 36: detail of mesh in one heat exchanger	54
Figure 37: detail of the expander mesh	55
Figure 38: pressure (left) and temperature (right) fields inside the circuit.....	56
Figure 39: change in fluid state in the evaporator (left) and condenser (right)	57
Figure 40: p-h diagram of the simulated ORC system, transformation in the duct upstream the evaporator magnified	58
Figure 42: temperature profile inside the evaporator (left) and condenser (right) as a function of the normalized height of the heat exchangers	59
Figure 43: simulated system section, with details of the internal geometry.....	61

Figure 44: detail of the mesh on the regenerator (left) and Coriolis flow meter inlet (right)	62
Figure 45: detail of the mesh for the stationary parts of the pump (left) and for the rotating domain (right).....	62
Figure 46: engagement process	62
Figure 47: gaps between tooth flank and pump housing	64
Figure 48: polar diagram of tooth head – pump casing gap width (left) and detail of the numerical grid for the same gap type (right)	64
Figure 49: relief groove. Upper and lower ports communicating (left), suction and discharge ports isolated (right).....	65
Figure 50: comparison between simulation results and experimental data	67
Figure 51: mass flow rate as a function of wheel angular position; on top, the reference angular position is showed	68
Figure 52: leakages through axial (left) and tooth (right) gaps, represented by means of velocity vectors.....	68
Figure 53: from top-left, clockwise: position of the pressure probes at the inlet and outlet sections; pressure plot on a plane perpendicular to wheels axes, with two black crosses indicating the position of the pressure probes; pressure measured with the exhaust probe as a function of wheel angular position; pressure measured with the intake probe as a function of wheel angular position	69
Figure 54: plots of the pressure field and velocity vectors on an axial section of the regenerator outlet duct for the case of $\alpha=0^\circ$ (top) and $\alpha=16.5^\circ$ (bottom) wheel angular positions.....	70
Figure 55: layout of the simulated domain with the positions of the two pressure probes .	72
Figure 56: pressure traces at the inlet (left) and at the outlet (right) of the Coriolis flow meter as a function of the wheel angular position	73
Figure 57: force acting on the CFM as a function of the wheel angular position (left) and its Fast Fourier Transformation (right).....	73
Figure 58: logic diagram for controlling an increase in the temperature of the hot source.	74
Figure 59: gas mass fraction for working conditions A (left), B (middle) and C (right) as reported in Table 11.....	75

Figure 60: mass flow rate of refrigerant delivered from the pump for the three cases reported in Table 11, as a function of the angular position of the wheels	76
Figure 61: geometry of the heat exchanger. A transversal section is showed on the right .	78
Figure 62: computational grid of the modeled heat exchanger. Global mesh (top), transversal section showing the polyhedral cells at the core and prismatic layers near the walls (bottom – left), magnification of the mesh in the axial direction (bottom – right)	79
Figure 63: liquid volume fraction on the walls of the exchanger after 1.0 second	80
Figure 64: liquid volume fraction on the walls of the exchanger after 1.5 seconds	81
Figure 65: liquid volume fraction inside the exchanger after 1.5 seconds	82
Figure 66: liquid volume fraction on the outlet section of the exchanger after 1.5 seconds	82
Figure 67: scroll machine (red circle) installed on the test stand	84
Figure 68: fluid model of the scroll expander; moving spiral (left) and stator (right)	84
Figure 69: sketch of a flank gap (left) and representation of background and overset grids, from [80] (right).....	85
Figure 70: representation of the fluid domain by means of overset mesh method (left) and detain of the mesh in narrow gaps (right).....	86
Figure 71: pressure plotted on planes perpendicular to expander rotational axis for two different values of rotational speed	87
Figure 72: velocity magnitude plots on planes perpendicular to expander rotational axis .	88
Figure 73: magnification of the recirculation zone	89
Figure 74: volumetric flow as a function of the normalized angular position	89
Figure 75: average values of the volumetric flow rate at the outlet of the machine. Actual values (left) and dimensionless ones (right)	89
Figure 76: defeatured geometry.....	91
Figure 77: section showing the position of the Oldham ring	92
Figure 78: mesh on a section perpendicular to moving spiral orbiting axis, for a given instant	93
Figure 79: R245fa mass flow rate at the inlet (solid line) and outlet (dashed line) of the machine.....	95

Figure 80: detail of the mesh in radial (left) and axial gaps (right). Magnification of the right-hand side picture is lower to show the relative dimensions of the prism layers with respect to the base grid.....	95
Figure 81: pressure traces at the inlet (solid line) and at the outlet (dashed line) ports	97
Figure 82: pressure inside the expander during its operation	98
Figure 83: static pressure during one revolution of the scroll shaft, values are in [Pa]	98
Figure 84: axial component of the velocity at the outlet of the machines, values are in [m/s]	99
Figure 85: single screw expander. From top-left, clockwise: real-world geometry; 3D-CAD model; detail of the meshing region; CAD model of the admission duct	101
Figure 86: fluid model of the single-screw expander	102
Figure 87: view of the inlet duct with the upper and lower inlet ports highlighted (cyan)	103
Figure 88: numerical grid of the inlet distributor, with the lower suction port grid magnified	106
Figure 89: numerical grid of the rotating parts (left) and on a section plane normal to starwheels axes (right)	106
Figure 90: flow streamlines in the inlet distributor	108
Figure 91: trajectories of the oil droplets. 0.50 μm (left), 5.0 μm (center) and 50 μm (right)	108
Figure 92: oil film thickness on the distributor surfaces after 0.5 s from injection start...	108
Figure 93: relative position between the screw rotor and the inlet port (red trace) for the considered instant	109
Figure 94: oil film thickness on the screw walls; the upper inlet port is highlighted in pink	110
Figure 95: absolute static pressure on the main rotor surface	110
Figure 96: mixture streamlines inside the expander	111
Figure 97: oil film evolution in the expander during time	112
Figure 98: computational mesh, with a detail of the prism layers near the boundaries of the domain	114
Figure 99: total pressure on the screw rotor for several angular positions.....	116

Figure 100: pressure profile at the upper suction port as a function of screw rotor angular position	117
Figure 101: positions of the virtual probes (left) and resulting pressure trend during expansion as a function of rotor angular position(right)	118
Figure 102: clearances in the meshing region	118
Figure 103: velocity magnitude of the refrigerant flowing to the upper admission port...	119
Figure 104: velocity magnitude of the refrigerant flowing to the lower admission port...	120
Figure 105: mass flow rate pulsation at the inlet of the machine as a function of the angular position of the screw rotor	120
Figure 106: flow recirculation behind the main rotor (left) and across the clearance between the groove and the housing (right).....	122
Figure 107: flow escaping through the clearance between the main rotor and the housing: velocity (left) and pressure (right) fields	122
Figure 108: pressure trends at the admission ports (top) and torque (bottom) at the screw shaft as a function of the main rotor angular position	123
Figure 109: interactions between the CFD tools	127

List of tables

Table 1: sensors main data.....	29
Table 2: sensors main data, continued.....	29
Table 3: Swep brazed-plate heat exchanger main specifications	31
Table 4: Climetal condenser main specifications	31
Table 5: Temprite liquid receiver main specifications	32
Table 6: evaporator main specifications	33
Table 7: ORC system testing conditions	41
Table 8: main properties of system components	53
Table 9: model boundary conditions and refrigerant properties.....	55
Table 10: thermodynamic properties of refrigerant in relevant sections of the circuit	57
Table 11: ORC system operating conditions after hot source temperature increase.....	75
Table 12: 1,1,1,2-Tetrafluoroethane (R134a) fluid properties	80
Table 13: oil-free compressor characteristics	83
Table 14: boundary conditions and geometric characteristics.....	93
Table 15: single screw expander geometric characteristics (from [34])	102
Table 16: model properties and boundary conditions	105
Table 17: oil droplets distribution	107

Why Organic Rankine Cycle systems

1.1 Introduction

Nowadays, pollutant emissions are a major concern among public opinion. CO₂ concentration in the atmosphere has reached a level never met before: 2017 data reports emissions for 32.3 Gt [1], while 33.4 Gt are given for 2018 [2], leading to an average concentration of 407.4 ppm in the atmosphere [3]. PM, NO_x, UHCs are other pollutants which contribute to greenhouse effect and are released from human activities at an unexpected rate, even because of the underestimation of pollutant potentiality for each of industrial and residential-driven activities, together with transportation. Among these sectors, energy production and industrial processes account for more than 60 % of global CO₂ emissions [1]. Above this, industrial activities reject a great amount of heat in the surrounding environment, perturbing its equilibrium when talking about aquatic habitat: 3000 MWe is the estimated power generation from the heat released in the sole EU-12 [4]. The fact is that the majority of this heat is rejected at a temperature below 250 °C, making its exploitation really complex. Apart from thermoelectric generators, which still represent a niche due to their high cost-per-Watt, when such a low temperature heat source is available, small scale organic Rankine cycle systems (ORCs) are the way which is usually chosen to generate mechanical or electrical energy. From the previous sentence, it is important to focus on the word “small”. In fact, different sizes of these systems are available, from few kW to MW, but the solutions available in the smaller power range are far more scarcer than the ones relative to the latter, mainly because of the delayed profitability of an investment, which can reach 3500 \$/kW [5]. In fact, this is reflected by the limited capacity in the range 1 kW – 100 kW installed worldwide: just 4.95 MWe_l, compared to a total of more than 2000 MWe_l [6]. In order to consider ORCs for decentralized power production it is necessary to find new technologies which enable the harvesting of low-temperature heat sources, keeping their cost as low as possible, both when implementing and maintaining the system. In doing so, it can be curious that the first ORCs ever made were in the micro range of power, and not for stationary applications at all.

The first commercial applications of a system using an organic fluid (ether) took place in the 19th century, for ship propulsion. The main problem of such a system was given by the sealing techniques of that time, which were not so good: leaks of this flammable gas were a common issue and led to the loss of at least one of the ships equipped with this propulsive system, leading to the dismissal of this idea or, at least, of this working fluid. At the end of that century, the idea of propelling ships by means of a system with greater efficiency than a standard steam cycle led to the patent of the naphtha launch by Ofeldt [7]. The clever idea was to use this hydrocarbon as both the working fluid for the cycle, the fuel for the burner and the lubricant. The absence of high-pressure steam in this apparatus made possible the operation of the launch without the presence of a qualified engineer as the operator, making this solution a commercial success, at least until internal combustion engines became sufficiently reliable and light, together with improvements in steam cycle. In those years, in fact, better sealing techniques led to an increase in the maximum allowable pressure inside the system and the development of the steam turbine, which surmounted the limitations of the steam engine, gave the death blow to non-aqueous fluids, at least for half a century.

In the 1930s, Luigi d'Amelio designed a solar ORC system which employed a 3.7 kW turbine using chloroethane as working fluid, but soon after his studies seem to have been forgotten, until during 1960s, in Israel, new studies were carried out taking into consideration what d'Amelio found during his work, that is the importance of fluid molecular weight in order to reduce the number of turbine stages and the revolution speed of the expander. In fact, Tabor and Bronicki [8] understood that several properties of the fluid are of paramount importance in designing a system: number of atoms in the molecule, boiling point, thermal stability and so on. In particular, they focused their work in obtaining a cycle with dry expansion, to avoid turbine blade erosion; the result was a recuperated cycle with a 3-kW turbine operating with monochlorobenzene. It is worth noticing that all these cycles were of the solar type. From this point on, during 1970s and 1980s numerous companies were established and systems with power of several hundreds of kilowatts were built.

In the last ten years, interest in the power range up to 10 kW has risen again mainly for automotive applications and decentralized power generation for domestic applications, to reduce the environmental impact and the efficiency of power generation. In this low power range, however, just a few companies operate with commercial products: as reported by Tocci et al. [6], less than ten on a world basis. Considerations about the ratio between the cost of the working fluid and the various system components and their reliability and safety

is of paramount importance in this range, leading the designers of such systems to tread a narrow path between these requirements.

Refrigerant selection is just the first choice the designer has to make, since also the expander and the pump, as well as the heat exchangers, have to be chosen wisely taking into account the type of fluid and the operating conditions. The problem is that, as reported by the same authors of a few lines above [6], the choice of the most appropriate expander in micro systems is a problem that still has to be resolved. For this reason, almost each ORC system manufacturer is developing his own expander, which can be of two types: volumetric or dynamic. The next paragraph will give more information about them.

1.2 ORC systems applications

As stated in the previous paragraph, the Organic Rankine Cycle is named after the nature of the working fluid, which is not water but a substance with a higher molecular mass. Because of this, the components which are needed to produce work from a hot source are the same of a standard water cycle: the condenser, the pump, and the heat exchangers (evaporator and condenser in case of dry fluid expansion, the recuperator can be installed when using wet substances or when limits on the maximum temperature at the inlet of the condenser exist). Then, depending on the available heat source, different technologies for these parts are recommended. When considering systems with a net power output below 10 kWe, the cost of the entire apparatus is often more important than its total efficiency, so the designer has usually to choose off-the-shelf components. In doing so, the nature of the heat source has to be taken into account: in fact, several environmental phenomena and anthropic activities release heat:

- Geothermal sites;
- Waste heat recovery;
- Solar fields;
- Combined heat and power (CHP) applications,

and for each one of these the output of the expander can be mechanical or electrical. When considering micro systems, the first entry of the previous list disappears, because geothermal ORC systems are economically sustainable only for sizes around and above several hundreds of kW. Thus, in the next paragraphs a few words on the other three energy sources will be spent.

In fact, there are two main drawbacks in applying ORC systems to vehicles: system complexity and absence of steady-state operations, with the former tightly linked to the latter. Since vehicles do not operate with a fixed load, attention has to be paid in harvesting heat at the engine exhaust since variation in the heat source temperature can be steep, leading to hot spots in the evaporator. Again, the use of a heat transfer fluid would be beneficial in terms of system stability, but would increase its cost, complexity and size. Heat recovering from the radiator and the exhaust gas recirculation valve can be done, then, but temperatures are lower, thus the net power output of the cycle would be lower. The unsteadiness of the driving cycle leads also to complex control of the system since, to maintain almost constant pressure and temperature at the expander inlet, the rotational speed of both pump and expander must be continuously adjusted: this implies that both these components should be linked to electric machines, in order for the engine control module to easily vary the speed. But this is more expensive than linking the pump and expander to the engine belts by means of clutches: this is another reason which makes clear why these small systems applied to vehicles are still at a prototypal stage, even in those applications such as long-haul trucks in which the engine load should be more constant during the driving cycle. At this point, and considering the “mobile application” of these cycles still immature, it seems clear that in the case of limited recoverable power in order to increase the global efficiency of the system it is better to use also the heat rejected by the ORC system itself for other purposes, such as heating house, offices, swimming pools and so on. In this way, we are speaking about combined heat and power (CHP) applications.

1.2.2 Combined heat and power

This method of using ORC systems is the most adapt in case of decentralized power generation. The main difference with respect to the other ORC application consists in using also the heat rejected at the condenser, at the evaporator or at the outlet of the heat source as-is, depending on the user heat demand, system complexity and the priority of heat request with respect to electrical output. In literature are reported cases in which electrical power is generated by means of ORCs coupled to biomass and natural gas-fueled furnaces, even in the lower power ranges (see, for example, references [10] and [11]); a scheme of a biomass micro-ORC CHP system is reported in the next picture.

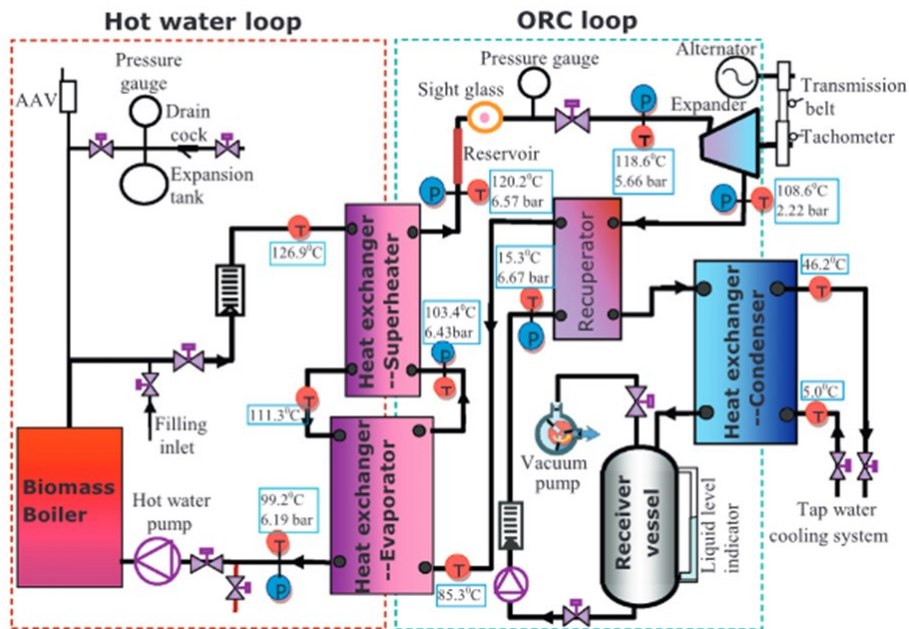


Figure 2: biomass-powered micro CHP system, from [12]

In a system such the one reported above, nearly 90 % of the thermal energy of boiler flue gases is transferred to the ORC heat transfer fluid: apart from reasons related to heat exchangers efficiency, this value is limited by the acid dew point of the gases, which must not be reached to avoid the corrosion of the heat exchanging element. This aspect shall be taken into account especially when considering domestic micro-CHP applications, since maintenance is often postponed or avoided: during 2014, in Italy, more than 120 accidents happened for issues related to inadequate servicing [13].

1.2.3 Solar fields

In these systems, solar radiation is collected or reflected into a heat collection element [14], where light is converted into heat which is then transferred to the heat transfer fluid, similarly to the WHR case. Typically, this fluid is not the ORC system working fluid, but it is an intermediate one which is transported to the cycle evaporator and then recirculated, as visible in Figure 3. While this is always true for medium and large size ORC systems, when dealing with just some kW of power direct steam generation is the preferred approach. With this configuration, the ORC system working fluid is vaporized inside the solar collector, avoiding the cost for a heat transfer fluid pump and for the evaporator [15], but increasing the one for the collector itself, since it has to withstand high pressures. Several technologies for the collectors have been developed in the years and all but the salt-gradient solar pond, the parabolic dish reflector (because of their cost) and the solar central tower are suitable for micro systems applications:

- Flat plate collector (FPC);
- Parabolic trough collector (PTC);
- Compound parabolic collector (CPC);
- Evacuated tube collector (ETC);
- Linear Fresnel collector (LFC).

The use of ORC systems is particularly profitable for the latter, since LFCs require a lower investment cost with respect to the other solutions and their lower optical performance, which reflects in a lower temperature of the heat transfer fluid, fits with the requirement of having relatively low temperatures for the ORC working fluid (below 300 °C). Small-scale solar-powered ORC systems are, in fact, mainly used for off-the-grid applications in remote areas, where electricity or mechanical power have to be generated by means of internal combustion engines, emphasizing the need of a cheap and robust system.

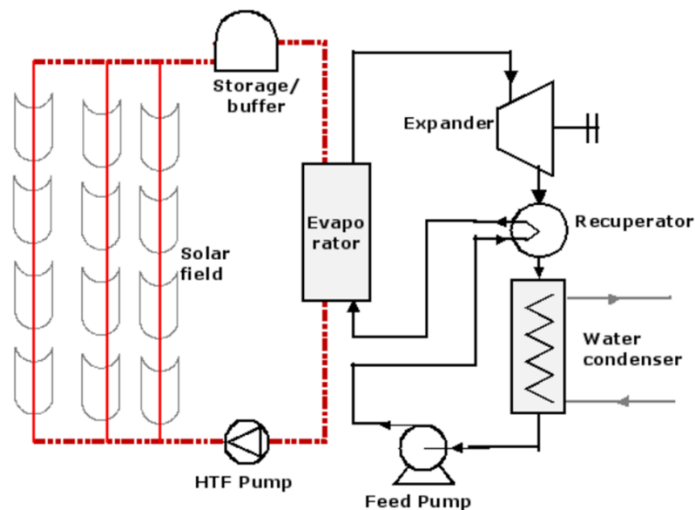


Figure 3: solar-powered ORC system schematics, from [16]

1.3 System layouts

1.3.1 Classic ORC

The classic layout for an Organic Rankine Cycle system is the subcritical one (see Figure 4), in which four main components are present: pump, evaporator, expander and condenser. In these systems the working fluid, after being pressurized by the pump, is heated in the evaporator until the organic medium vaporize, up to the saturation temperature or above, becoming superheated vapor. This fluid is then expanded, harvesting mechanical work at the shaft of the expander and then is brought back to the liquid state in the condenser, where at the outlet of this device is put back in circulation by the pump, which closes the cycle.

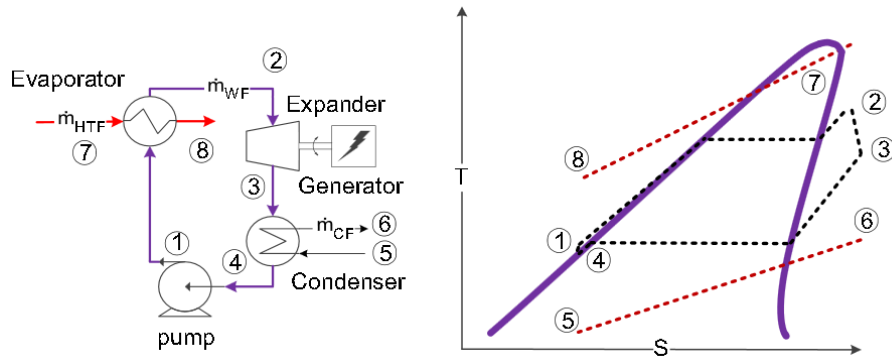


Figure 4: standard ORC system. Left: system schematics, right: qualitative T-S diagram (from [17])

From this layout several others have been developed, to better match the temperature of the working fluid with the one of the heat source and to increase the difference between the temperatures of heat addition and heat rejection [17]. The fact is that no one of the proposed, innovative layouts have already been scaled to the required dimensions and power output required for micro applications, since the smallest flash cycles (OFCs) or trilateral cycles (TC) are for power outputs greater than 100 kWe (the system with the smallest output adopting one of these technologies, which has been found in literature, is the 120 kWe trilateral flash cycle reported in [18]). This happens mainly because these approaches require or a two-phase expander (TC), or a flash evaporator (OFC), which are costly devices, if compared to the ones usually employed in micro-scale systems. On the other hand, but still at a prototypal stage, the pumpless Rankine cycle (PRC) is a promising technology which allows the system to work, as suggested by its name, without the pump. For these reasons, in the following lines the classic ORC layout modified by adding a recuperator and the PRC layout will be shown.

1.3.2 Recuperated ORC

The simplest modification from the layout showed in the previous paragraph is given by adding a recuperator, to preheat the working fluid before its admission in the evaporator by using the vapor at the exit of the expander. In this way the thermal efficiency of the cycle is increased, as stated in [19], because of the increase of the heat transfer average temperature to the cycle and the simultaneous decrease of the temperature of the heat released to the environment via the condenser. The resulting system layout is showed in Figure 5: it can be seen, from point 2 of the T-S diagram, that the fluid must be superheated before its admission in the expander. For this reason, caution should be used when superheating a dry fluid, since it is possible to still have vapor in this state also at the exhaust of the expander, increasing the load of the condenser. Another aspect which has to be considered is the smaller pressure

drop through the expander because of the presence of this device, which can cause a reduction in the available work at its shaft.

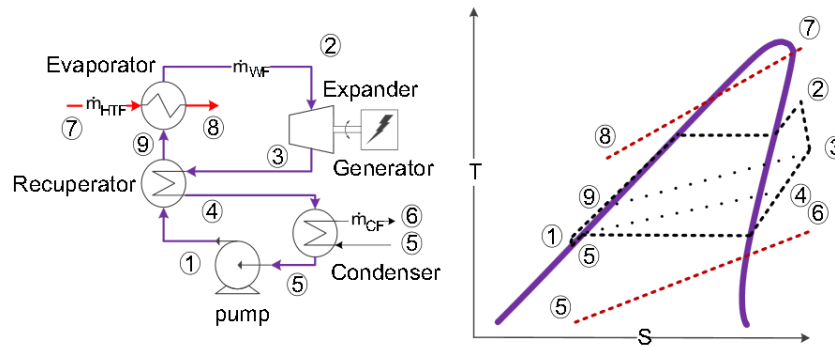


Figure 5: recuperated ORC system. Left: system schematics, right: qualitative T-S diagram (from [17])

1.3.3 Pumpless ORC

Even if the pump is not the aim of the vast majority of the studies reported in literature, its behavior greatly influences the performance of the entire system, with the final effect of reducing the net power available at the shaft of the expander. Moreover, pump has to be placed in the lowest level of the system, to avoid fluid cavitation for certain working conditions which can be encountered in systems with variable temperature heat source: this poses a limit on the possible configurations which can be adopted for the packaging of the different components, which is an aspect of great importance for systems which have to be generally placed in domestic or recreational facilities because of their limited power output. In light of all these considerations, Yamada et al. [20] tried to overcome all these issues by proposing a type of pumpless ORC system (PRC) composed by two heat exchangers, an expander and a set of valves. The authors used these valves to switch the heat exchangers between the evaporator and the expander mode, by modifying the flow of the heat carrier. For this reason, the mean power provided by the expander is not constant as in a typical ORC but intermittent, as it is possible to see from the graph of Figure 6, where a qualitative graph which shows how the time in which the system produces useful work is less than the total working time is reported. In their work, they performed an experimental test campaign on a prototypal system using R245fa refrigerant as the working fluid, where a scroll machine was considered for the expander and the two heat exchangers were of the brazed-plate type: both the heat source and the heat sink were water. Power generation with such a system was not trivial because of the characteristics of the heat source and sink, which was water for both the thermal reservoirs: for the former, the fluid was supplied at 90 °C with a flow rate of 0.12 m³/h, while 0.48 m³/h of water was supplied to the condenser at 20 °C.

The interesting fact is that even if the average power generated by the expander was of just 20 W, when they compared their PRC with an ORC under the same working conditions (with the only addition of the working fluid pump) they found that their PRC system presented a negative value for the net power of 8 W (meaning that the electrical valves required a consumption of 28 W), while the comparable ORC requested more than ten times more energy: -84 W of net power production because of the presence of the pump. The same findings on a similar set-up have also been validated by Gao et al. [21], making it clear how this is a promising technology to generate work from heat sinks whose temperature is below 100 °C.

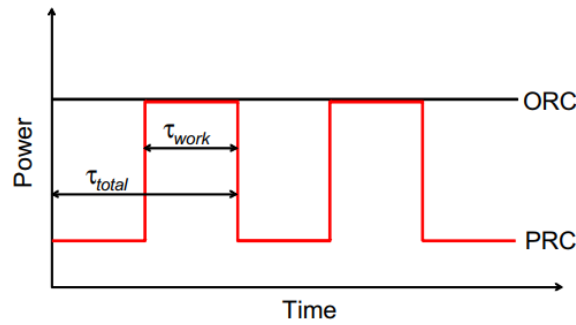


Figure 6: variation of the power provided by the system as a function of time (from [20])

1.4 Cycle components

1.4.1 Heat exchangers

Below 10 kW the use of shell-and-tube heat exchangers, which are usually adopted in systems with a power output in the MW range, is avoided due to their dimensions, cost and low global heat transfer coefficient [22]. Then, the choice is between plate heat exchangers and the ones with an even higher heat transfer surface area, such as the tube-fin and plate-fin ones.

1.4.1.1. Plate heat exchangers

Plate Heat Exchangers (PHEs) are usually built with flat, metal plates on which a certain pattern is engraved. These plates are made from stainless steel but, if required by the application, also titanium, graphite, Ni-Cr alloys and polymers, for low-temperature applications. Fluid leakages are prevented by using gaskets or by brazing or welding the plates, depending on the tightness or application required. For pressures below 1 MPa and temperatures lower than 200 °C, gasketed PHEs can be adopted, see Figure 7.

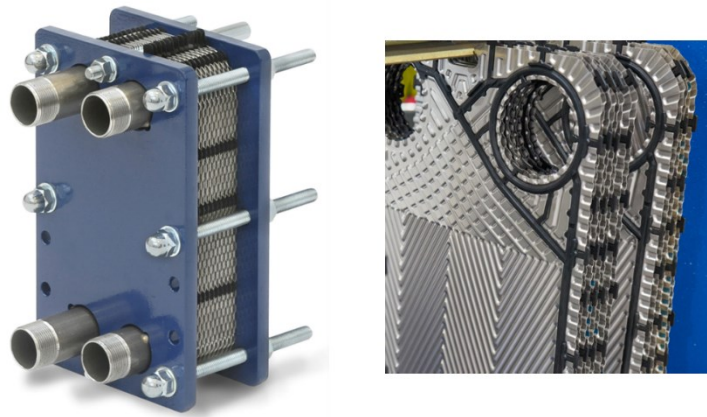


Figure 7: left: gasketed plate heat exchanger; right: detail of the gasket around a fluid port

In Figure 7 a small-size heat exchanger is showed on the left, together with a detail on the arrangement of the gaskets around a corrugated plate and a fluid port. The seals pattern is designed in order to separate the two fluids in the case of a leak and, in some models, to let the leaking fluid dripping outside the exchanger, in order to the system operator to detect the problem. This expedient is reported on the right-hand side of Figure 8.

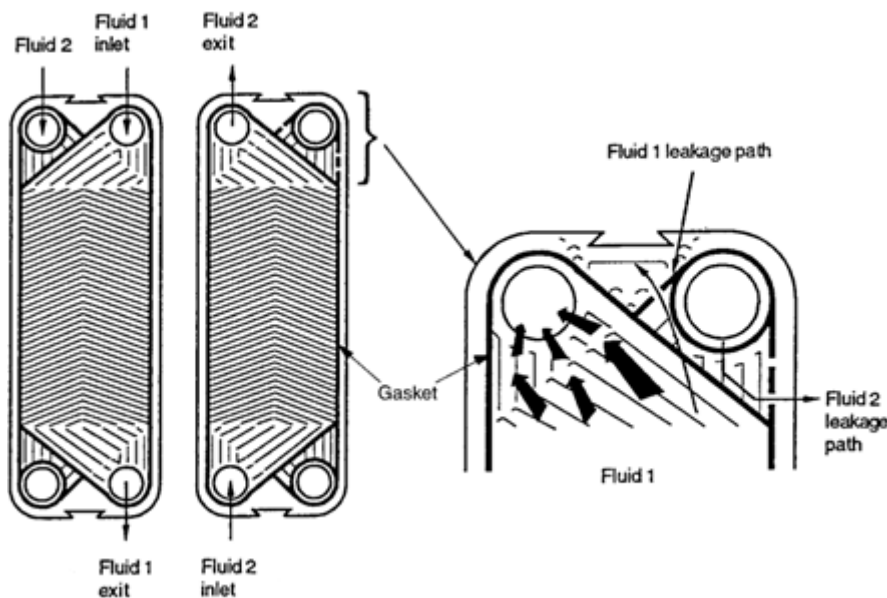


Figure 8: plates, gaskets and leakages paths for a gasketed PHE (adapted from [23])

In Figure 8 is also visible a different type of plate grooves with respect to the one showed in the previous picture. These grooves are needed to create tortuous passages for the fluid, in order to increase the heat transfer rate and to improve the rigidity of the plates. Furthermore, thanks to these details, fouling of the device is up to 25 % lower than the one encounterable in shell-and-tube exchangers [23]. Because of these aspects, more than sixty different geometries for water passages have been proposed during the years, leading to high thermal

effectiveness (even more than 90 %) and, for a given heat request, to an heat exchanging surface up to one third of a shell-and-tube exchanger. As for the plate material, also the one of the gaskets has to be chosen taking into consideration the compromise between cost, durability and suitability with the fluids being used in the component. These exchangers are usually designed in a one pass – one pass counterflow arrangement, meaning that there is a sequence of gasketed and ungasketed ports throughout the axial length of the exchanger, as reported in Figure 9. This happens because, in this way, all the inlet and outlet ports can be placed on the same fixed cover, allowing for the disassembly of the exchanger for cleaning or repairing purposes without removing the pipes which are connected to the device.



Figure 9: counterflow, 1 pass - 1 pass plate HE scheme (from [23])

As reported at the beginning of this paragraph, gaskets are the weak point of these exchangers: they limit maximum pressures and temperatures of the working fluid, they can lead to spills of refrigerant, which are to be avoided because of the health hazard, the environment damage and cost itself of the leaked substance and, furthermore, they are not able to deal with corrosive fluids. To overcome these issues, plate heat exchangers where these gaskets have been replaced with welds have been developed. For applications where compact devices are needed, plates are not welded but brazed, and the exchanger which is obtained is usually directly mounted on piping, without the need of a frame, leading to a lighter product. Obviously, as in the case of welded devices, this PHE cannot be opened for cleaning or other purposes, limiting its applicability to systems in which fouling is negligible. Because of the reduced dimensions and limited effectiveness (the heat exchanger effectiveness is the ratio between the actual heat transfer rate and the theoretical, maximum heat transfer rate), which is around 60 %, in several occasions plate heat exchangers are not the right choice for a given application, mainly when one has to deal with high thermal loads and there is no room for a bigger plate exchanger. For these reasons, fins are added to the exchangers, as a way to increase the heat exchanging surface. This type of exchangers can be classified in two categories: tube-fin and plate-fin heat exchangers. It has to be noticed that these types of exchangers are usually employed for gas-to-gas or liquid-to-gas heat transfer, even if there are some rare two-phase fluid-to-liquid applications.

1.4.1.2. Tube-fin heat exchangers

When one fluid has a higher pressure or heat transfer coefficient than the other, this type of exchangers is usually employed. In this device, heat from the hot fluid is passed to the cold one by means of the fins placed on the pipes, thus we are considering conduction heat transfer. Pipes are, generally, of round or rectangular shape (see Figure 10) and fins are attached to them with one amongst several methods, such as bonding, brazing, soldering and so on. These joining techniques are adopted also to link the tubes to the two headers and condition the maximum allowable fluid pressure inside the pipes (since inside these parts the fluid with the highest pressure has to flow). The area density of these devices can reach values greater than $3000 \text{ m}^2/\text{m}^3$, which is nearly 4 times of the plate HEX one. But there are times in which even more compact heat exchangers are required, for example in mobile applications (condensers for vehicle air conditioning system). In these cases, plate-and-fin exchangers are usually employed.

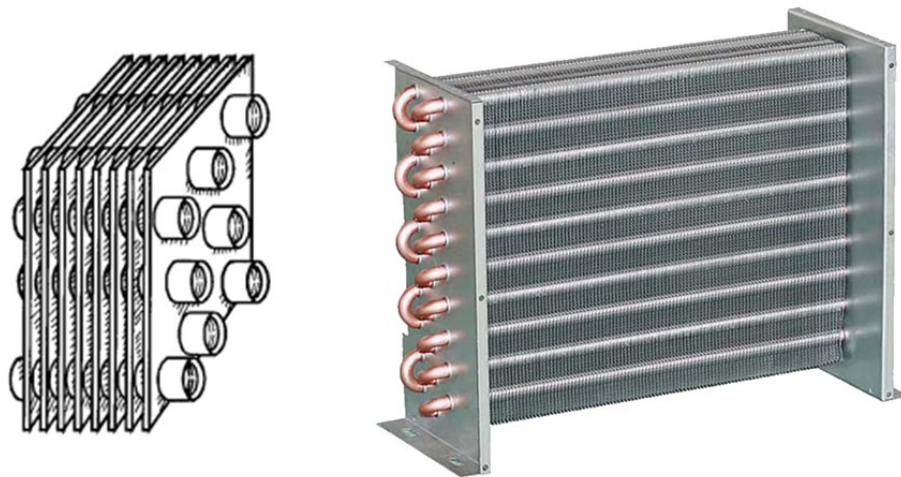


Figure 10: tube-and-fin heat exchanger scheme (left, from [23]) and actual component (right)

1.4.1.3. Plate-fin heat exchanger

With peak area density values of almost $6000 \text{ m}^2/\text{m}^3$, fin-and-plate heat exchangers are widely used where compactness is one of the priorities. In their simplest concept, corrugated fins are inserted between two parallel flat surfaces and the fluids flows across the fins' openings, each one on a different side of the plates. Nowadays, geometries are much more complex, but the working principle remains the same; an innovative type of such HEXs is given by the microchannel one. This layout, as the name suggests, is characterized by the fact that one of the fluid being in the liquid phase passes through tubes with a diameter smaller than 1 mm [24]: this tubes are arranged as a stack within a same surface, this is why

they belongs to the fin-and-plate category, see Figure 11. The point in reducing up to these values the diameter of the fluid passages stays in the definition of the heat transfer coefficient for internal flow: this coefficient is proportional to the inverse of the diameter of the tube, thus a decrease in this dimension is desired in applications where high thermal power has to be dissipated in a limited volume. This has also a beneficial effect on the refrigerant charge and on the weight of the apparatus, since less fluid is required: the latter makes the supporting frame unnecessary, like the small-size PHEs introduced in paragraph 1.4.1.1.

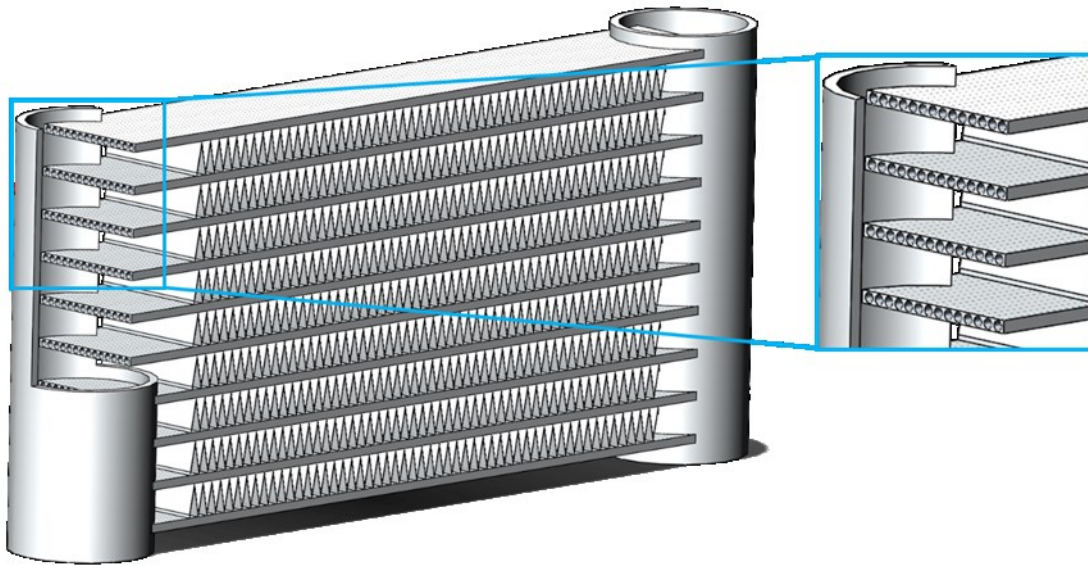


Figure 11: microchannel heat exchanger model; on the left: magnification of microtubes

1.4.2 Expansion machines

1.4.2.1. Introduction

The net power output of the ORC system strongly derives from the type of the various components chosen for its operation. While in paragraph 1.4.1 several properties of the more common heat exchangers for micro-ORC applications were depicted, in the following lines properties and criteria of choice for the expansion machine will be showed.

First of all, for application below 10 kWe, the use of a turbine is uncommon: in [25] the authors show that below this power limit volumetric expanders are used the most, and a similar result is showed by other researchers in [26]. In fact, for low working fluid mass flow rate, typical for systems of this size, radial machines have to rotate at excessively high speeds to produce a decent amount of power at their shaft. High velocities require expensive bearings, which increase the cost the solution. The alternatives to radial machines are axial turbines, which are even more costly [27] and, since organic fluids show low values for the speed of sound, experience high values of the Mach number, which lower turbine efficiency.

In light of these considerations, positive displacement machines seem the most appropriate in this power range. These devices are characterized by the presence of one or more translating or rotating parts inside a stationary housing. The pressurized fluid enters the machine and displaces those boundaries: in this way, while work can be collected at the rotating shaft of the machine, the volume of the working chamber increases and fluid pressure decreases. When this happens, it is possible that in the last phases of expansion some droplets of liquid appear in the gas phase: this fact is tolerated by these types of devices, while is not by turbomachines. Another couple of aspects make volumetric expanders attractive: their low rotational speed, making it possible to directly match the machine to the alternator if electricity has to be generated and their reliability, since they are usually derived from compressor applications. The latter, on the other hand, can cause some decrease in efficiency, if the machine is adopted as-is. In fact, when choosing the expander for a given system, one has to care about expander internal volume ratio and the system volume ratio: where the latter depends on system operating conditions, the former is defined as the volume at the end of the expansion process divided by the one at the end of the suction process [28]. When the expander volume ratio is lower than the system one, under-expansion occurs, meaning that at the outlet of the machine we will find fluid with a pressure greater than the one in the discharge line of the entire system; the opposite happens in case of over-expansion (see Figure 12). This is the most important source of losses in case of an off-the-shelf expander, which decrease the isentropic efficiency, but unfortunately other issues such as internal leakages, friction and heat losses take place. To reduce leakages it is not possible to decrease gaps between surfaces over a certain value, for reasons regarding both operating conditions and manufacturing techniques; furthermore, oil-free machines have wider gaps than lubricated ones, because the moving elements are prone to a greater thermal expansion than the latter: it is then strongly recommended the use of some oil. Anyway, moving surfaces do not come into contact because are linked to synchronized gears or others timing devices so the main objective of oil injection is to seal the various gaps. This oil can be mixed to the working fluid and circulated in the entire system or it can be injected in the expander and separated from the refrigerant at the outlet of the machine but each one of these solutions has its pros and cons: the circulation of oil in all the pipes and components allows for a simpler, cheaper and smaller system layout, without the need of an oil separator, while on the other hand it decreases the performance of the heat exchangers, because of the film deposits on their walls. Volume ratio and lubrication characteristics are just two of the various parameters to consider when dealing with volumetric machines; others are:

- Pressure ratio: the ratio between the value of the pressure at the end of the suction process and the one at the end of the expansion process;
- Filling factor: similar to volumetric efficiency, is computed as the mass flow rate of the working fluid at the inlet of the machine divided by the theoretical flow rate (product of rotational speed, suction volume and density of the fluid);
- Isentropic efficiency: ratio between the actual value of the power produced by the expander and the theoretical one, where the latter is calculated as the product between the mass flow rate and the isentropic enthalpy drop across the machine;
- Displacement;
- Rotational speed: together with the displacement, it gives the mass flow rate processed by the machine and, as reported at the beginning of the paragraph, it influences the level of vibrations.

The volumetric expanders which are employed the most are the scroll, screw (both single and twin), piston and vane machines. In the next paragraphs, the benefits and disbenefits of these different types of positive displacement expanders will be showed.

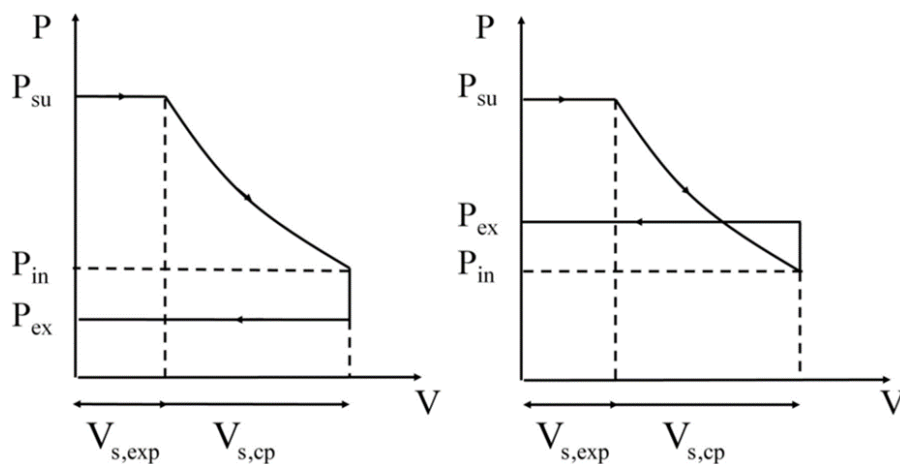


Figure 12: under-expansion (left) and over-expansion (right), from [29]

1.4.2.2. Scroll expanders

In the last decade, the use of scroll machines as expanders for micro-ORC systems has increased due to their few moving parts, compact structure reliability, non-excessive level of noise and vibrations and, mainly, their low purchase and maintenance costs. A scroll machine is visible in Figure 13, where the two spirals are shown: the fixed one on the left and the mobile one on the right. The mobile part does not rotate, but it translates around the

fixed one following a circular path: in order to obtain this a component, named Oldham ring, is placed between the two spirals, or more often behind the moving one.



Figure 13: disassembled scroll machine; stator (left), rotor (right)

Scroll machines, as other positive displacement devices, are categorized into three main classes: hermetic, semi-hermetic and open-drive devices. The difference between these classes stays in how work at the shaft of the machine is harvested: in hermetic machines the assembly of the scroll, the electrical machine and the shaft connecting them is enclosed in an housing whose parts are welded together, so the assembly is not serviceable. Semi-hermetic machines still have all the components assembled inside the same housing, but the outer shell is composed by parts which are joined together with removable connections; open drive expanders are the one in which the volumetric machine and the electrical generator are not installed in the same housing, thus to transfer work from the former to the latter seals are required on the shaft exiting the housing on the expander side, to prevent working fluid leakages. Alternatively, the coupling between the expansion device shaft and the generator one can be obtained thanks to a magnetic device: in this case no leakages of fluid are expected, since no hole is present on the housing of the expander to let the shaft pass through, but losses can originate from eddy currents which creates a torque opposed to the one which is transferred by the shaft, decreasing the available power at the generator [30]. In expansion mode, the fluid enters in the middle of the machine and is discharged at its periphery. From the inlet port to the outlet one, fluid decreases its pressure by moving the spiral, creating chamber with increasing volume. At first, the suction chamber is divided into two parallel expansion chambers whose duration, in terms of angular position of the shaft, depends on the volume ratio of the machine. At the end of the expansion process these two chambers connect to the discharge line, leading to a “perfect” expansion if the discharge pressure is the same as the one in the discharge line or an under- or over-expansion, as explained before. A scheme of the expansion process inside one of these machines is showed in Figure 14.

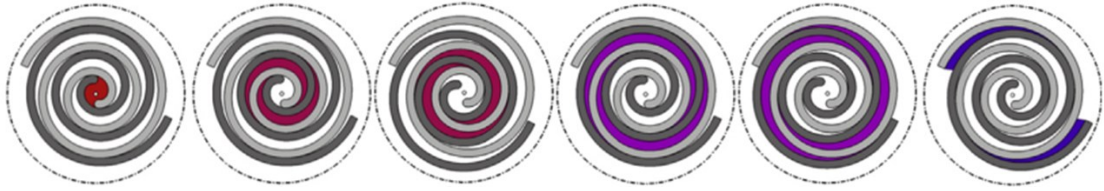


Figure 14: left to right: expansion process in a scroll expander, adapted from [28]

When considering the performance of this type of machines, it must be considered that the volumetric efficiency is reduced by fluid leakages which take place in two different locations of the machine, namely from the axial gaps and radial (or flank) gaps. The first ones are given by the clearance between the machine housing and the moving spiral, while the radial ones are given by the distance between the flanks of the orbiting spiral and the ones of the fixed scroll.

1.4.2.3. Screw expanders

As for all the volumetric machines, also these devices were born as compressors and then they have been adapted to gas expansion. There are two types of screw expanders: twin-screw and single-screw ones. Each one has its own advantages and drawbacks.

Twin-screw machines were born with the patent of Lysholm in 1935, even if their first concept was deposited almost sixty years before, in 1878, by Krigar. In such devices two rotors, each one with helical teeth, engages: one is called “male” rotor because of its lobes, the other “female” because of its valleys. These two meshing shafts are enclosed in an housing which, during rotors movement, defines a series of working chambers in which the fluid is compressed, or is expanded, from the inlet to the outlet ports of the machine, which are placed at both the extremities of the two rotating shafts. An example of such a machine is reported in Figure 15, together with a section depicting lobes and valleys profile. The number of lobes and valleys depends on considerations regarding machine dimensions and cost, as reported by [31]: in fact, for a given application, the designer ought to minimize these two parameters by maximizing the swept volume, to obtain a compact machine.

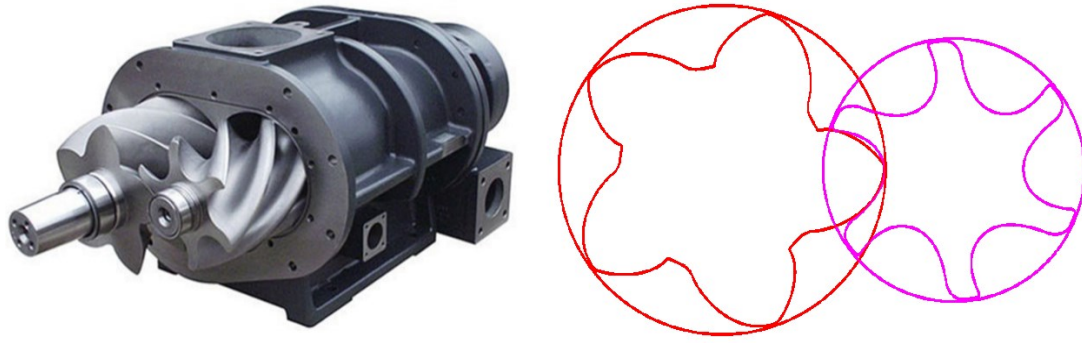


Figure 15: screw machine; left: actual device; right: rotors profile (from [32])

This volume is proportional to the length of the rotors and inversely proportional to the number of lobes. The fact is that rotors with few lobes have a small shaft diameter, so the high-pressure gas leads to shaft deflection. In applications where high pressure ratios are required it is then necessary to increase the number of lobes, making bulkier shafts [31], but since economical constraints emerge when trying to reach the optimum value for each expansion ratio, a few types of rotor profiles with accordingly-sized shafts diameter have been standardized, and the most common configuration is given by six valleys on the female rotor and four lobes on the male one. Since, as reported before, in micro ORC systems the minimization of the Total Cost of Ownership (TCO) is often the main driver for choosing its layout, its components and the working fluid, the fact that twin-screw expanders require manufacturing techniques capable of machining the rotors with high accuracy, both in oil-flooded (since female rotor is in contact with the male one) and oil-free (the two screws must not contact each other) machines, has pushed the researchers to find a similar device with a lower cost. This has been found in the single-screw expander.

The single-screw machine has been introduced in the 1960s by Zimmern [33], because of the need of a compact, cheap and silent compressor using air or refrigerant as the working fluid able to run without lubricant to seal the gaps between the various components. In fact, in the original concept, these interstices were sealed by means of the same fluid being compressed, but in liquid phase. This fact highlights the great compatibility of these devices with substances in their liquid state, making it suitable of being adopted as an expander for ORC systems. Single-screw machine consists, in its common application, of a screw which engages with two gaterotors, symmetrically mounted with respect to the main rotor. Other layouts exist, as shown in Figure 16, but the CP type (cylindrical screw, planar gaterotors, the one on the top-right in the following picture) is the most employed for fluid compression or expansion.

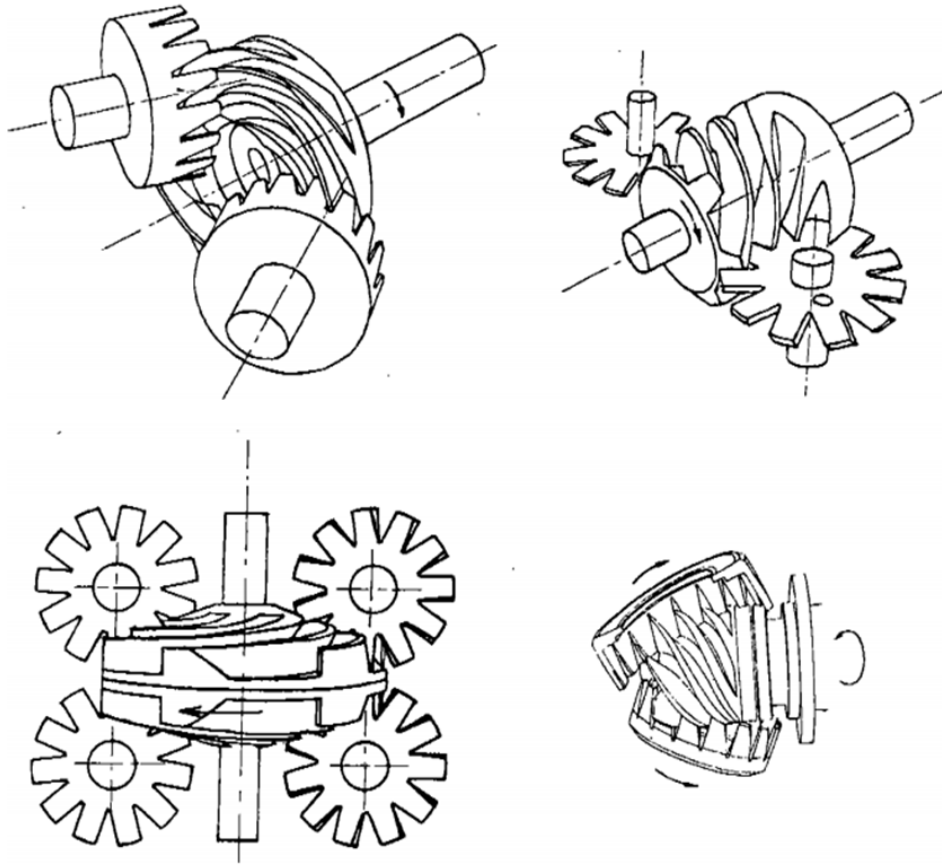


Figure 16: single-screw machine layouts, adapted from [33]

Since the meshing between the three components defines a working chamber on each side of the screw, fluid expansion is symmetrical with respect to the main rotor rotational axis making it possible, also thanks to other geometrical features in the high-pressure zone of the casing, to have a screw which is not subjected to both radial and axial loads, increasing bearings duration. As in the twin-screw machine, the swept volume per revolution can be controlled by reducing or increasing the number of grooves of the screw. A geometry which is commonly encountered in literature (see, for example, Ziviani et al. [34] and Zhang et al. [35]) is the one characterized by a screw with six grooves and the two starwheels with eleven teeth, as visible in Figure 17.

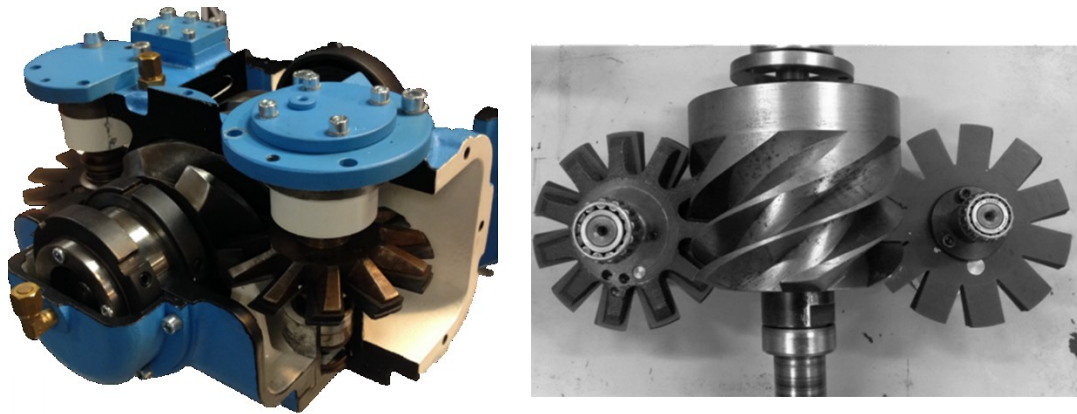


Figure 17: single-screw expander: complete machine (left), screw and starwheels (from [35], right)

1.4.2.4. Vane expanders

The vane machine is a very versatile device, since it is used also to pump liquids (like oil in power-steering or automatic-gearbox applications), besides compressing or expanding gases. The first applications of this device in ORC systems are reported in [36], where the authors also reported a limited efficiency due to overheating and thermal expansion of the vanes, which can lock up during machine operations. In fact, a vane expander is composed by a cylindrical rotor which rotates inside a stator, but the former axis is offset with respect to the latter one. In the rotating part, a certain number of vanes is placed, and these rectangular-shaped components are pushed against the housing walls by means of springs or pressurized hydraulic fluid, delimiting the various expansion chambers. Great care has to be taken into choosing which of the two mechanisms because, while springs offer a better volumetric performance of the machine since the vane is always pushed against the housing, friction losses are greater than the other case, leading to a decrease of isentropic efficiency [28]. Given this, one has to take great care in increasing the volume ratio of the expander, since in doing so the number of vanes must be increased. To decrease friction losses and the consequent temperature increment, oil injection is the most obvious expedient; this, as reported for the other expanders in the previous paragraph, has also the merit of decreasing working fluid leakages across the machine: vane expander in fact has several leakage paths, which can contribute to up to 20 % of the total power losses [37], and more than 60 % are given by pressure drop at the inlet port.

1.4.2.5. Piston expanders

Piston expanders employed in ORC systems are not only based on the well-known reciprocating scheme, but other families do exist, such as rotary piston (or Wankel, after their inventor), gerotor, swashplate, and rolling piston machines [38]. In truth, the traditional

“automotive-type” mechanism is not widely adopted as an expander since it shows a complex construction with a greater number of components with respect to other machines (above which intake and exhaust valves), it accept a lower fraction of liquid at both the inlet and outlet of the machine, vibrations and thus noise are greater than other piston machines, it shows high friction losses and thus low efficiency and it cannot operate without lubricant. Furthermore, these machines are heavy also because of the need of the crank train, to convert the linear motion of the piston in rotating motion for the user. Given all these drawbacks, other mechanisms have been developed; in particular, to avoid the use of the crankshaft, axial-type machines have been introduced [28]. Among these, the swashplate expander (Figure 18, top-left) bases its origins on the swashplate compressor, which is used for automotive air conditioning applications. In this device, not only a single piston exists, but several of them are connected, in a circular fashion, to the machine shaft, parallelly to it, by means of rods: these rods are linked to a plate which tilts with respect to the shaft in a way that allows these components to both slide and rotate. Apart from a reduction in the size of the entire machine, the other advantage of such a mechanism, which seems extremely complex, is given by the fact that the angle of which the plate is allowed to tilt can be adjusted during expander operation, making it possible to change the pistons stroke and thus the displacement of the machine. Even if piston expanders carry with them all the issues listed above, they could be of aid in case very high expansion ratios are required, since Daccord et al. [39] reported one of these machines operating on a pressure ratio of 50.

Rotary piston expanders (Figure 18, top-right) can be of interest because of their low vibrations and noise, together with small dimensions and low weight. The piston, as conceived by Wankel, is of a near-triangular shape and, being its rotational axis offset from the axis of the housing, during its rotation it creates volumes which are isolated from the others thanks to its shape. Because of this, the edges are always in contact with the walls of the housing, leading to a sensible wear of the piston gaskets. Furthermore, since also lubrication is critical for these machines, gaskets materials have to be chosen as a compromise between their duration and their capability of seal the gaps, influencing the number of maintenance actions and the volumetric efficiency of the machine.

The gerotor expander (Figure 18, bottom-left) is a positive displacement machine consisting in two rotors, one inside the other, in which the inner rotor has a number n of teeth and the outer one $n+1$, where n is greater than two. The axis of the inner rotor is offset of a certain quantity from the one of the outer rotor so, when both components start rotating in the same direction, n expansion chambers with volumes variable with time are created, with each one

of them decreasing at first and then increasing. These expanders are characterized by the fact that, as opposed to the reciprocating pistons, they do not require lubrication.

Rolling piston expanders (Figure 18, bottom-right) are other machines characterized by a rather simple design. A piston is placed inside an housing and it can rotate around the internal walls of the latter, so the working fluid is injected in the domain and moves the shaft thanks to its expansion in the free volume. A single vane is placed between the inlet and outlet ports, with the aim of avoiding the leak of fluid from the expansion chamber; this vane works in the same way as for the vane expander, so a spring pushes it against the moving piston. This fact leads to the same issues listed some paragraph above, which can be synthetized in friction losses and wear of the vane. The main advantage of rolling piston expanders is given by their low cost of production, making their choice possible if both efficiency and low-pressure ratio are not of primary concern for the system conductor.

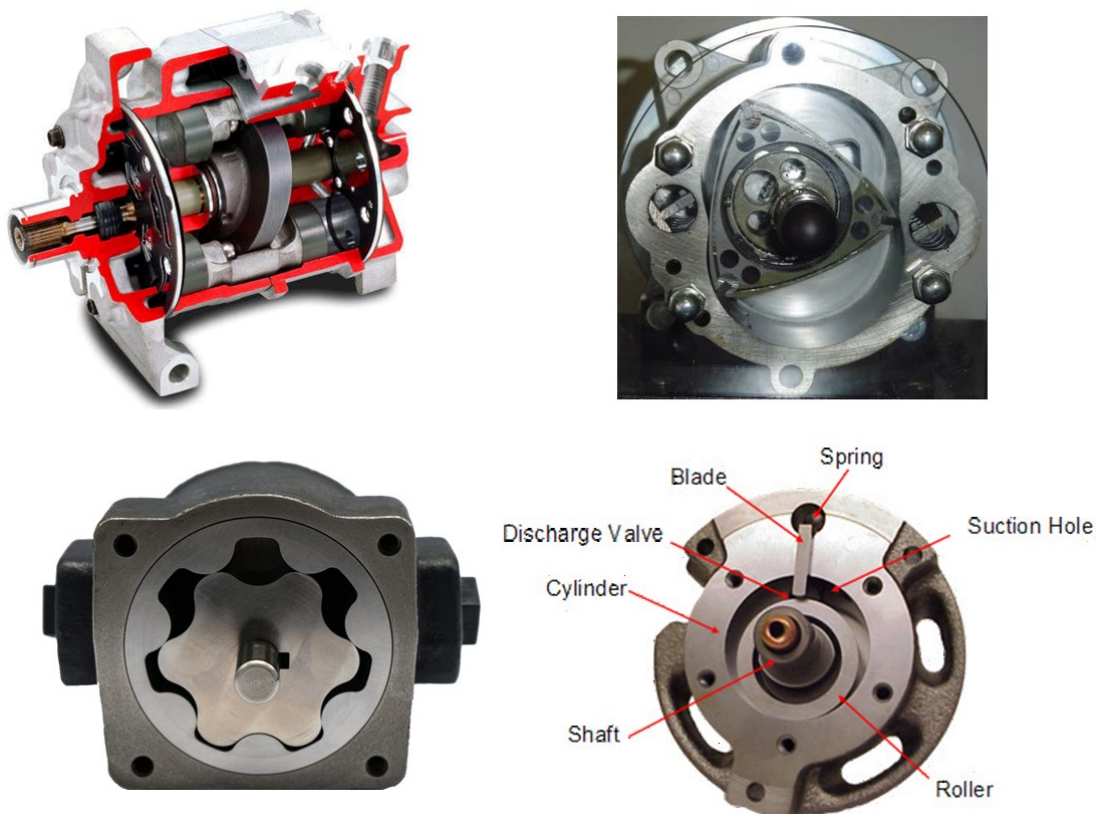


Figure 18: different piston expanders. Swashplate (top left), rotary (top right), gerotor (bottom left), rolling piston (bottom right)

1.4.3 Pumps

While in medium and large scale ORC, as well as in water Rankine cycles, pump efficiency and thus its energy consumption is of relative importance, because of the great expander output, in micro-scale ORCs the back-work ratio can reach values greater than 10 %, as

reported in [40]. The fact is that few studies regarding pump for micro systems are present in literature, as showed also by Bracco et al. [41], but among these some general guidelines can be found. First of all, as for expanders, positive displacement machines are preferred to centrifugal ones, since within micro-ORCs we find high pressure ratios and low flow rates, requirements which can be fulfilled only with multistage architectures, which are excessively bulk and expensive for this type of applications [42]. From some of the studies published in years (such as [43], [16]), it seems difficult to find a pump-motor system able to reach a global efficiency greater than 20 %. In fact, not only the pump itself shows low efficiency, mainly due to the low viscosity of the organic fluid which leaks from the gaps of the machine, but also the electric motor results in being a critical component, because for the typical rotational speeds of the pumping element, well below 3000 rpm, which lead to low efficiency. Clemente et al. [44] tested a lubricated external gear pump elaborating R245fa as working fluid: they found that pump efficiency increased with pressure, reaching a peak of almost 65 % (at least for the highest values of its rotational speed), but they also found that the mechanical work required to its shaft reached the 10 % of the power produced by the expander, not considering the electrical motor connected to the pumping unit. If greater efficiency and pressure ratio are required, Aoun [45] presented a piston pump capable of up to 78 % of efficiency when delivering fluid at a pressure of 60 bar and with a rotational speed greater than 800 rpm, with the main issue of a maximum allowable temperature for the working fluid equals to 50 °C.

1.5 Working fluids

Some aspects that must be considered when choosing the working fluid for a given application were listed in paragraph 1.1, but their most important categorization is based on the slope of the saturated vapor curve. In fact, this characteristic influences both system layout and its components, together with its global efficiency. As reported in Figure 19, three types of saturation curves exist: wet fluids, like water, show a negative slope for the saturated vapor curve, while for dry fluids the slope is positive. Among these two categories, lie isentropic substances for which, during expansion, vapor remains saturated from the inlet to the outlet of the device, without condensation [26]. Dry and isentropic fluids are then more suitable than wet ones for being employed in ORCs, since they do not need to be superheated in order to avoid liquid at the end of the expansion phase.

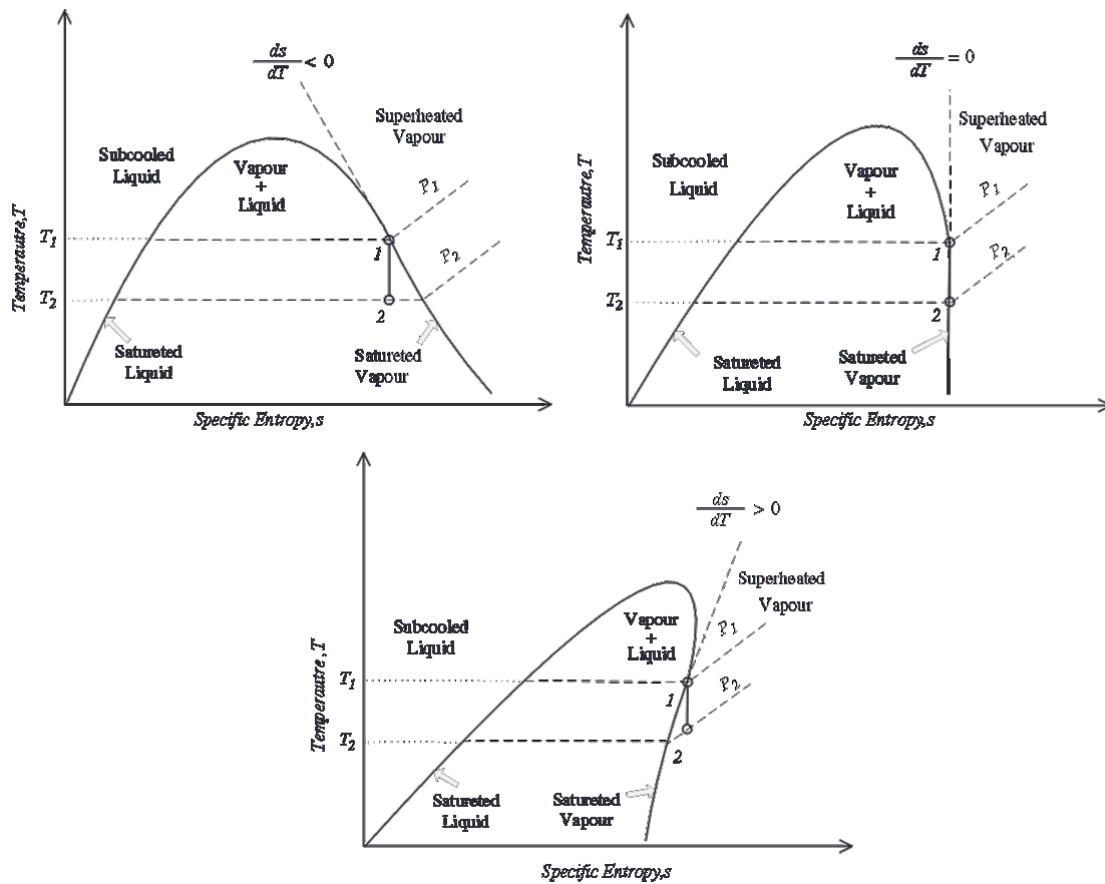


Figure 19: wet (top-left), isentropic (top-right) and dry (bottom) saturated vapor curves on a T-s diagram, from [46]

Given this first, broad categorization, a number of properties must be considered when choosing the fluid for a given system:

- heat of vaporization: generally speaking, fluids with high values for the vaporization latent heat are desirable to have the most of the energy from the heat source exchanged with them during phase change [47], but an exception occurs when considering waste heat recovery applications since, as noted by [48], having a low value for latent heat of vaporization leads to have variable temperature heat transfer in the evaporator, in order to follow the temperature profile in the heat exchanger, reducing the irreversibility of this process;
- price: organic fluid are expensive, for example R245fa price is around 15 \$/kg, while R450a costs 28 \$/kg;
- molecular weight: the highest this parameter, the lowest the rotational speed of the dynamic expander, due to a low enthalpy drop through the turbine;

- condensation pressure: if too high, it reduces expander work production and requires more resistant and thus more expensive materials. If too low, size of the condenser has to be increased;
- decomposition temperature: each fluid has a temperature above which its molecules break into several fragments, thus the system has to operate well below this value;
- freezing point: relevant if the system is shut down in certain geographical locations;
- density: the highest the density, the lowest are the dimensions of components, since they are directly linked to the volumetric flow rate;
- heat transfer related properties: a great heat transfer leads to the reduction of heat exchangers dimensions;
- environmental and safety requisites prescribed by the authorities of the country in which the system has to be sold.

Taking into considerations all these requirements, during years tens of fluids have been developed and adopted in both commercial and research systems, but the ones which are used the most belongs to the family of hydrofluorocarbons (HFCs), such as R134a, R245fa, R-152a and the siloxanes, even if D4 and D5 are deemed as “substances of very high concerns” by the European Chemicals Agency [49] and so their use should be limited. A characteristic of all pure substances is given by the fact that boiling and condensing temperatures are at a fixed temperature, for a given pressure. This represents an issue for those cases in which the ORC system heat source temperature is not constant with time, for example in waste heat recovery applications. In these cases, it is desirable a working fluid showing boiling and condensation temperatures are variable inside a certain range: this is the case of zeotropic mixtures. Zeotropic blends have been extensively studied since 1990 [17], starting from the experience gained in cryogenic refrigeration [50]. By using these mixtures, since the temperature profile at the heat exchangers is better followed, it is possible to increase the power production by reducing the irreversibilities in the heat transfer process. In spite of this, the use of these blends is limited because of the issues in refilling a system subjected to fluid leakage, since the more volatile component is more prone to escape to the environment than the other one, thus it is difficult to refill the system up to the original composition.

An actual micro-ORC system

2.1 Introduction

In this paragraph, a micro-ORC test stand installed at the Herrick Labs of Purdue University will be described. That system (Figure 20) is a recuperated cycle with a target electrical power output of 1 kW. The heat source is hot air, while the heat sink is air at environmental temperature. Measurements of temperatures, pressures, mass flow and mechanical input and output power to the pump and from the expander were taken during the stay as a visiting scholar in that university.

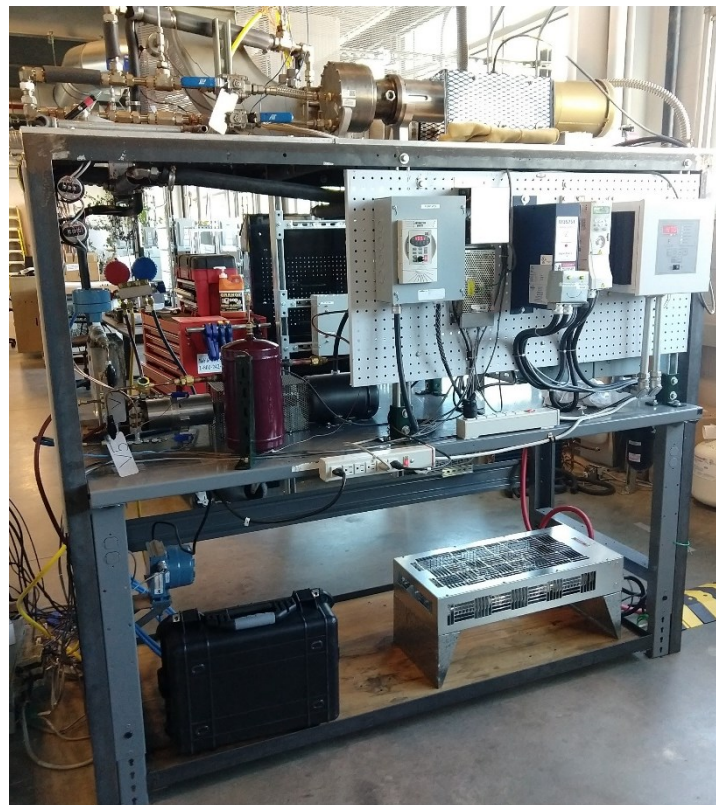


Figure 20: Herrick Labs micro-ORC system

2.2 Test stand characteristics

The global characteristics of the system depicted in the previous pictures are included in the master thesis of its designer (Lavernia, [51]), but are here reported for clarity. Looking at

Figure 20, we see that the expander was located on the top surface of the test stand, to have gravity removing potential liquid phase at the outlet of the evaporator; this was also promoted by the layout of the piping between the outlet of the evaporator and the inlet of the expander, whose first segment was vertical. For the same reason, pump was placed in the lowest surface of the metallic frame, with a buffer tank placed upstream its inlet, in order to let the eventual vapor exiting the condenser to sediment in the top part of this reservoir: in this way, pump was less prone of cavitating. A by-pass valve has been placed in order to avoid the liquid to enter the expander during the start-up phase of the system, due to low heat source temperature. To speed-up this phase, the air flow at the condenser was reduced with respect to its nominal value, setting the rotational speed of the pump accordingly. Regarding the heat source, compressed air was used to simulate the exhaust gases of an internal combustion engine, so it was heated up to a temperature of 650 °C and then it flowed across the evaporator: excess heat was rejected in the laboratory environment, as well as the one exiting the condenser.

2.3 Instrumentation

To collect data from the system, several instruments were fitted in different locations on the test stand. Temperature measurements were made by means of eleven type-J (Fe/Cu-Ni) and ten type-K (Ni-Cr/Ni-Al) thermocouples, of which two were pre-installed in the air heater by its manufacturer, for both safety reasons (shut-off of the heating element in case of a too high temperature for a given airflow) and control of the heater itself.

Working fluid pressure was measured thanks to four variable capacitance, absolute pressure transducers placed upstream and downstream of the pump and the expander, connected to pipes by means of pig-tail tubing, in order to dampen the vibrations caused by the pulsating flow in the ducts.

A Coriolis sensor was used to measure the mass flow of refrigerant circulating in the system. It was placed downstream the pump, not to create head losses capable of inducing cavitation to the supply unit. A second flow meter, hot wire sensor type, was installed to measure the volumetric flow of compressed air at the inlet of the evaporator: the measure was then combined with the ones of environmental temperature, pressure and humidity to calculate the mass air flow.

Two rotating strain sensors were fitted to measure torque requested by the pump and generated by the expander. These two devices were placed between the volumetric machines

and their motor or generator covered by a metallic shielding, not to enter into contact with the rotating shaft extensions of the machines.

Data from all these sensors were collected thanks to an Agilent AG 344980 data acquisition device, by converting the incoming voltage and current inputs in digital signal read by a dedicated computer. Three acquisition cards were installed on the DAQ, sampling incoming signal at a rate of 1 Hz: one card for J-type thermocouples, one for K-type thermocouples and the last one for all the other signals, which stayed in $-5+5$ V range. On the computer connected to the DAQ, LabVIEW was used as the acquisition software and user control panel; to calculate real-time fluid properties such as enthalpy and entropy, CoolProp library [52] was employed: in this way it was possible to plot on the T-s diagram the instantaneous thermodynamic states in selected points, such as inlet and outlet of the expander or evaporator.

Table 1: sensors main data

	Thermocouples		Pressure transducers	Coriolis mass flow meter
	J-type	K-type		
Model	Omega ICSS-18U	Omega KQXL-18U	Setra 280G-040B	Micro motion DS025S119SU
Output signal	-8-70 mV	-7-55 mV	0-5 V	0-10 V
Measurement range	0-750 °C	0-1250 °C	0-40 bar	0-180 g/s
Accuracy	± 2.2 °C	± 2.2 °C	± 0.044 bar	± 0.18 g/s

Table 2: sensors main data, continued

	Hot-wire volume flow meter	Torque meters	
		Pump	Expander
Model	ifm SD8001	Omega TQ514-012	Omega TQ514-200
Output signal	4-20 mA	-5-5 V	-5-5 V
Measurement range	1.7-225 m ³ h	0.00-1.41 Nm	0.00-23.0 Nm
Accuracy	± 3.0 % R + 0.3 % F.S.	± 0.142 Nm	± 0.232 Nm

2.4 Main components

2.4.1 Expander

The expansion machine adopted for this system was a prototype, Oldham-ring type scroll machine (Figure 21). It was a semi-hermetic, lubricated machine, in which the coupling between the expander shaft and the electric motor one was accomplished by means of a magnetic device. 5 % by mass of Polyolester oil had to be mixed together with the refrigerant, which is R245fa, an hydrofluorocarbon with formula $C_3H_3F_5$, widely used for ORC applications: the mixture entered the machine through the port located in the middle of

the housing and it was discharged through the exhaust port in the periphery of the frontal surface. The internal volume ratio of the machine was 4.318, while its suction volume was $4.56 \times 10^{-6} \text{ m}^3$. Since the machine had to be adopted to supply power to the American electrical grid, its design speed was 3600 rpm.

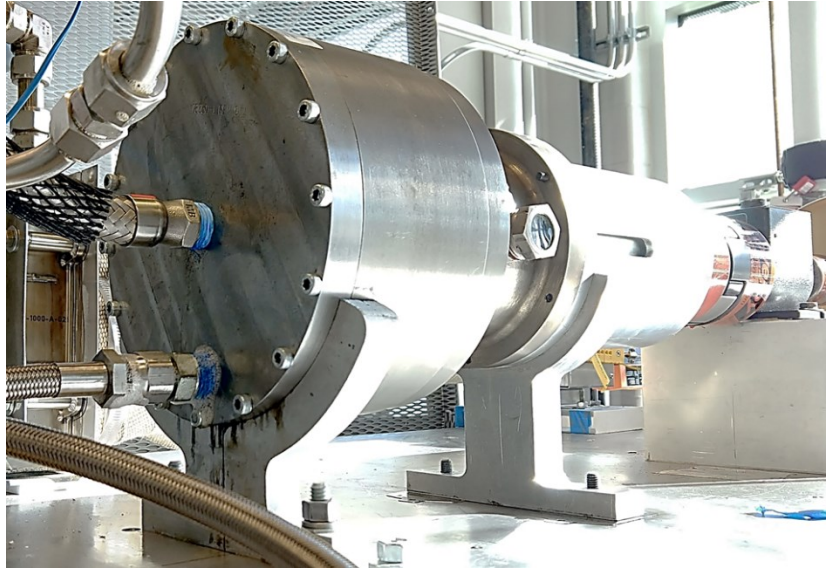
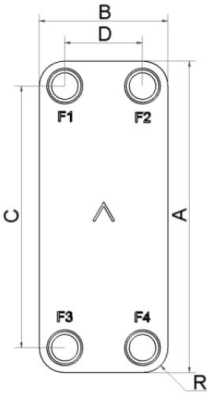


Figure 21: Scroll expander

2.4.2 Recuperator

The recuperator was a brazed plate heat exchanger built by SWEP, whose characteristics are reported in Table 3. It has been necessary to install this device in order to cool down the gases at the outlet of the expander prior of their inlet into the condenser, since this exchanger was made of aluminum, which experiences softening for temperatures above $150 \text{ }^\circ\text{C}$. The recuperator plates were made of stainless steel 316L and were brazed together with copper. Considering the layout of the recuperator, port F1 was connected to the outlet of the expander, F2 to the inlet of the evaporator, F3 to the inlet of condenser and F4 to the exhaust port of the pump.

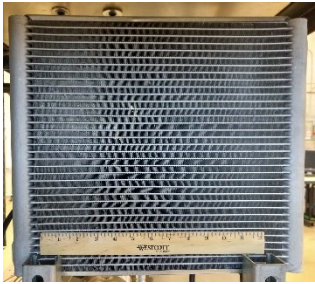
Table 3: Swep brazed-plate heat exchanger main specifications

	Number of plates [-]	10	Height [mm]	317
	Maximum flow rate [m ³ /h]	4	Width [mm]	76
	Volume per channel [dm ³]	0.039	Depth [mm]	33
	Maximum pressure [bar]	45	Weight [kg]	1.6

2.4.3 Condenser and liquid receiver

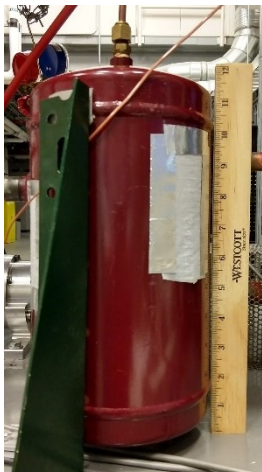
The microchannel air-condenser used in the test rig was a custom prototype, in order to reach a good compromise between device footprint and the required heat transfer rates. It was a three-pass heat exchanger, where both the liquid channels and the fins, welded between the extruded channels, were made of aluminum. Vapor from the recuperator entered the condenser on the top, while subcooled liquid was exhausted on the bottom of the device. In Table 4, the main characteristics of this heat exchanger are shown.

Table 4: Climetal condenser main specifications

	Number of passes [-]	3	Height [mm]	354
	Number of microtubes [-]	10	Width [mm]	415
	Internal volume [dm ³]	0.7	Depth [mm]	25
	Burst pressure [bar]	140	Weight [kg]	2.1

Downstream of the condenser, a tank was installed in order to guarantee an adequate head for the pump, not to incur in cavitation and a sight glass was placed in the liquid line before the pump inlet to check if two-phase refrigerant was entering the machine.

Table 5: Temprite liquid receiver main specifications

	Max. temperature [°C]	160	Height [mm]	313
	Min. temperature [°C]	0	Diameter [mm]	152
	Internal volume [dm ³]	4.16	Inlet loc. [mm]	244
	Maximum pressure [bar]	45	Outlet loc. [mm]	219

2.4.4 Pump

As the expander, also the pump adopted an Oldham-ring, scroll layout which is quite unusual, since this type of machine are usually employed to work with gases, not liquids. For this reason, the pump used in the system was a prototype; another peculiarity was given by the fact that its nominal rotational speed was half the expander one, namely 1800 rpm. Other specifications regard the suction volume, equals to $1e-6 \text{ m}^3$ and the unitary value for the internal volume ratio. Because of its operation, the fluid entered from the port in the periphery of the front plate and it is was exhausted from the one located in the middle of the plate.

2.4.5 Evaporator

The evaporator was a prototype micro tube heat exchanger, manufactured to meet the heat transfer requirements of the ORC system reducing the overall dimensions with respect to commercial exchangers. It was designed with both the inlet and outlet ports on its top surface: after entering the evaporator, the fluid was distributed in the several microtubes by means of a collector. Then, the fluid arrived to the bottom collector and was redirected to the upper one, passing through another passage of microtubes and, finally, exiting the exchanger. Thanks to both this port and dual passage layout, the heat transfer was optimized and, furthermore, gravity helped in increasing liquid residence time in the device, reducing the probability of having liquid droplets at the outlet of the exchanger and, thus, at the inlet of the expander. In the following table, the main characteristics of the evaporator are reported, while a couple of photos are showed in Figure 22; unfortunately, it has not been possible to take a picture of that component alone. Given this, the photo on the left emphasizes the limited axial extension of the device, while on the right it is visible the duct

which connects the heat torch to the evaporator. This steel duct is wrapped in fiberglass tape to reduce heat losses.

Table 6: evaporator main specifications

Number of microtubes [-]	843	Height [mm]	212
Number of passages [-]	2	Width [mm]	161
Tube diameter [mm]	0.45	Depth [mm]	50
		Weight [kg]	5.64

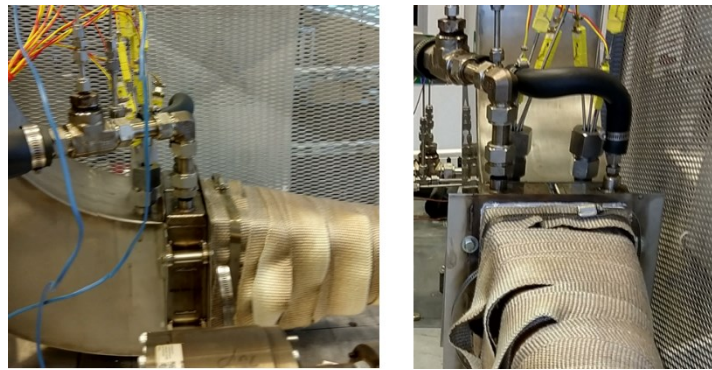


Figure 22: microchannel evaporator

2.5 Ancillary systems

2.5.1 Air stream (heat source)

As repeated in the last paragraph, the heat source for the ORC system was hot air. To generate the air flow required to evaporate the refrigerant, a stream of compressed air generated by compressors installed in the laboratories was used. The main issue of this approach was that the maximum value of this stream available at the system location was equals to $47.52 \text{ m}^3/\text{h}$, not even half of the required volume flow ($98.54 \text{ m}^3/\text{h}$). To overcome this fact, an air flow amplifier was installed: as reported in [53], this device works by injecting through an annular nozzle (number 2 in Figure 23) a thin film of primary air (the compressed air flow). This air is then deflected by a ring towards a frusto-conical surface and continues to flow as an high-velocity thin-film on the conical surface mixing with secondary air which is, in our case, the environmental air inside the laboratory. In this way, a peak value for the output air volume flow of more than $163 \text{ m}^3/\text{h}$ was reached, and the resulting air flow was canalized to the evaporator passing through the airflow meter.

2.5.2 Air stream (heat sink)

As anticipated in the paragraph about the condenser, the cooling medium was air, which flow was induced by an axial fan capable of delivering a flow rate up to 1900 m³/h: its flow rate was controlled by means of a potentiometer, which output was adjusted based on the fan curve, to let the system operator to vary the flow rate as a function of the cooling air required by the condenser during warm-up phase and regular operation. As for the evaporator case, air was then rejected into the laboratory environment.

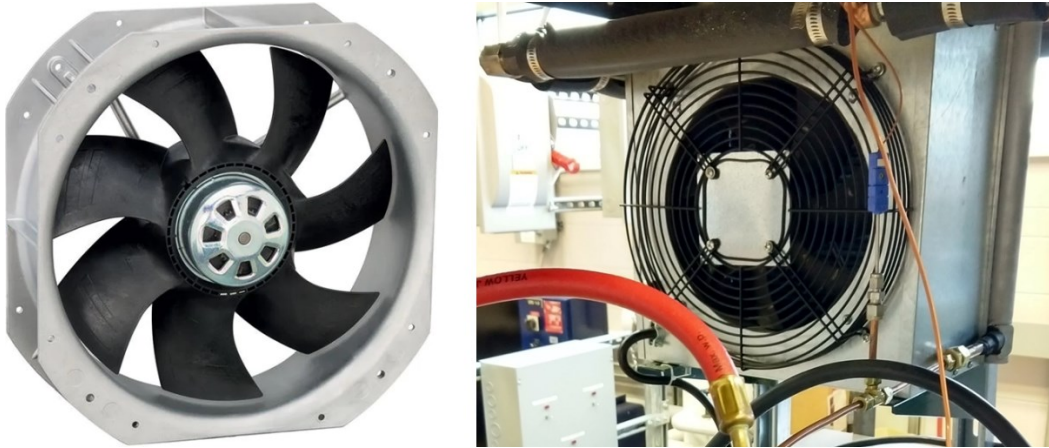


Figure 25: condenser axial fan. Left: from manufacturer catalogue, right: as installed on the condenser

2.5.3 Pump electrical system

The scroll pump was connected to a 120 V AC, single-phase electrical motor, which delivered a maximum of 0.75HP. Its synchronous speed was 3600 rpm, which was the nominal speed of the pump. The motor was controlled by means of an inverter, whose installation adopted a couple of peculiarities in order to reduce electrical interference with other sensors: first, it was powered through an isolated power line and second, cables to the electrical motor were shielded. A picture of the assembly of motor, torque sensor, couplings and pump is showed in Figure 26.



Figure 26: motor-pump assembly

2.5.4 Expander electrical system

Differently to what happened with the pump, the expander management system not only had to start the rotation of this volumetric machine but, once fluid began the expansion through it, it had to deal with the mechanical torque produced by the scroll machine. Given this, the expander was connected to a tri-phase electric motor, delivering 1.5 HP with the synchronous speed equals to the nominal speed of the expander, which was 3600 rpm (60 Hz). As for the pump, also this motor was driven by an inverter, supplying the 480 V current for the user-defined work frequencies. The inverter featured a built-in braking resistor, which was needed to deal with the scroll engine delivering positive torque to the electric motor: the inverter had then to brake the motor to maintain the set rotational speed. The current generated by the motor operating in this mode was sent to the resistor, being then dissipated as heat. The fact is that the internal resistor of the inverter was not designed for continuous duty, as happens during normal system operation: therefore, the system was equipped with an auxiliary braking transistor with a duty cycle equals to 20 %: this meant that, even if its peak breaking current was 7.75 A, well above the peak expected value of 3.25 A, it could not withstand continuous operation. For this reason, another product was used, a resistor bank capable of dissipating a constant power of 3.7 kW. In Figure 27, the pump and expander motors inverters, together with the braking transistor are shown.



Figure 27: from the left: pump motor inverter, 24 V DC power supply, braking transistor, expander motor inverter, heat torch controller

Before showing the results, the thermodynamic relations which permitted the evaluation of system performance are presented.

2.6 Results

A quantity which has been defined to evaluate the performance of the scroll expander was the isentropic efficiency, as defined in [55]:

$$\eta_{is,exp} = \frac{W_{el,exp}}{\dot{m}_{R245fa} \cdot (h_{exp,bef} - h_{exp,aft,is})} \quad (1)$$

where $W_{el,exp}$ is the electrical power, \dot{m}_{R245fa} is the mass flow rate of refrigerant at the inlet of the machine, $h_{exp,bef}$ is the specific enthalpy of the refrigerant at the inlet port of the expander and $h_{exp,aft,is}$ is the specific enthalpy of the working fluid after the isentropic expansion from the state at the inlet to the pressure at the exhaust. Since no instrument was installed on the test stand to measure the electrical power generated by the alternator, it has been necessary to calculate it by multiplying the measured mechanical power at the shaft of the expander by the electrical motor efficiency, as reported on the supporting documents. In Figure 28, the performance curves reported on the datasheet of the motor are shown.

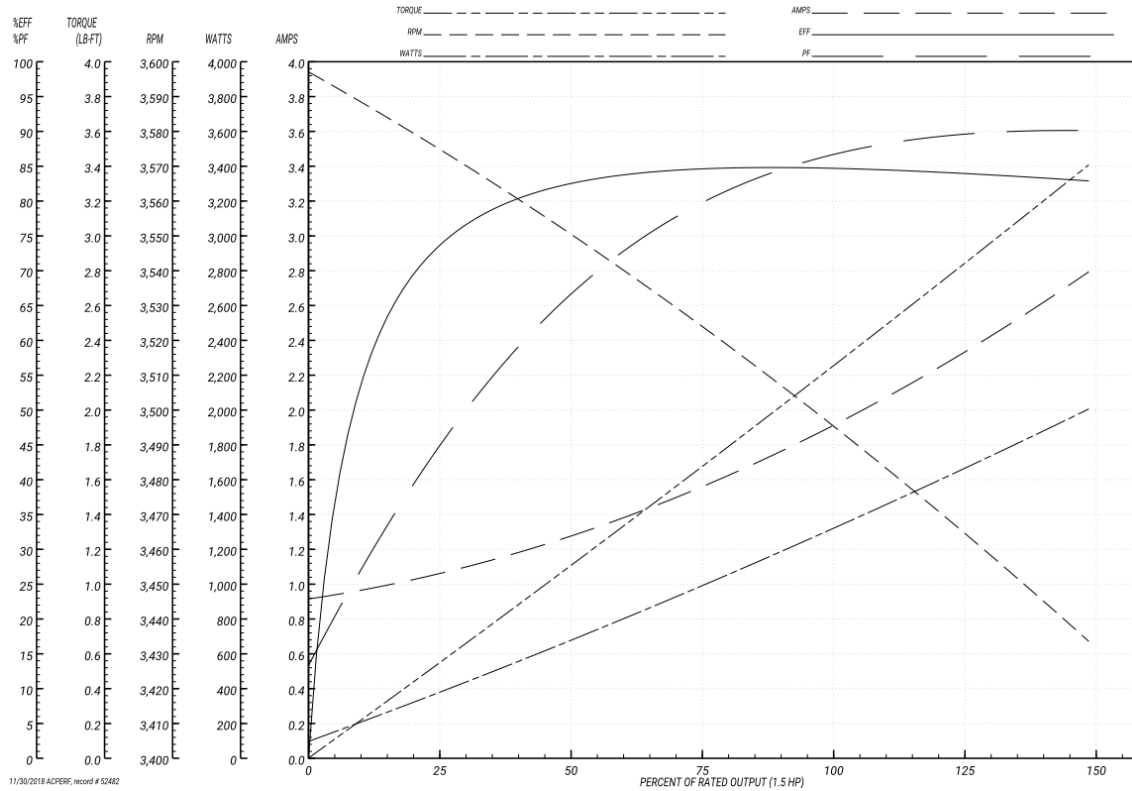


Figure 28: performance curves of the expander electrical motor – generator, from its datasheet [56]

As it is possible to see from equation (1), that is not the usual definition for the isentropic efficiency used when assessing the performance of turbomachines since, at the numerator, no enthalpy drop of the real expansion through the expander is reported: this happens because, while in a dynamic machine the enthalpy drop corresponds to the specific work given that the expansion can be considered almost adiabatic, in a positive displacement expander this simplification cannot be made (see reference [57]).

Another quantity which is useful to show in assessing the performance of a volumetric expander is the Filling Factor (FF), which has been defined for the first time by Zanelli and Favrat [58]:

$$FF = \frac{\dot{m}_{suc}}{N \cdot V_{suc} \cdot \rho_{suc}} \quad (2)$$

where N is the rotational speed, V_{suc} is the suction volume and ρ_{suc} the density of fluid at the inlet. By looking at its definition, a value for the FF equal to one means that the actual flow rate flowing through the machine is equal to the theoretical flow rate, making its definition similar to the one of the volumetric efficiency.

Given this couple of relations, the aim of the test campaign ran during the stay at the Herrick Labs was to investigate the performances of a new generation of scroll expander and scroll pump, if compared to the ones studied by Lavernia [51]. These performances were evaluated by operating the system in steady state conditions, which were met after ten minutes with fixed values of pump and expander speed, together with fixed temperature and volumetric flow rate of the hot air entering the evaporator. Tests were conducted following well defined safety and operational procedures; in particular:

- Expander bypass valve was opened, to exclude the machine during warm-up phase;
- Pump was started at a speed of 720 rpm;
- The condenser fan speed was set-up at 50 % of its nominal value;
- Air flow to the air heater (and thus to the evaporator) was initialized at 96.8 m³/h;
- Heat torch was turned on with a conservative starting temperature of 250 °C.

Once vapor was obtained at the outlet of the evaporator, the bypass valve was closed, the expander started at 1200 rpm, the heat torch temperature was increased of 50 °C and the condenser fan was run at full power. With these conditions it was possible to set the ORC system in a stand-by status from which the various working points could be reached, with the only requirements of maintaining refrigerant temperature and pressure at the outlet of the evaporator below 275 °C and 35 bar respectively.

Before showing the results obtained in the test campaign, some introductory remarks on how changes in components operating conditions can influence system output are given. Enthalpy drop through the expander, and thus work at its shaft, can be adjusted by modifying heat source temperature and volume flow, together with condenser fan speed: while the former affects the superheating degree, the latter influences subcooling degree, thus condensation pressure. Work at the shaft is also influenced by pump rotational speed: the higher the speed, the higher the flow rate and pressure in the cycle, giving an higher power output for fixed expander inlet temperature. On the other hand, also the expander rotational speed influences pressure and temperature at its input and outlet ports, and thus the work harvested at the shaft. It is then clear how every single working condition of every single system device has an effect on the other components. For this reason, some concerns were raised by the high unsteadiness of the hot air source.

In paragraph 2.5.1, it has been written that the primary air which simulated the flue gases was supplied through laboratory compressed air line. The behavior of control system of the

compressors probably led to the flow pulsations showed in Figure 29 and, in greater detail, in Figure 30.

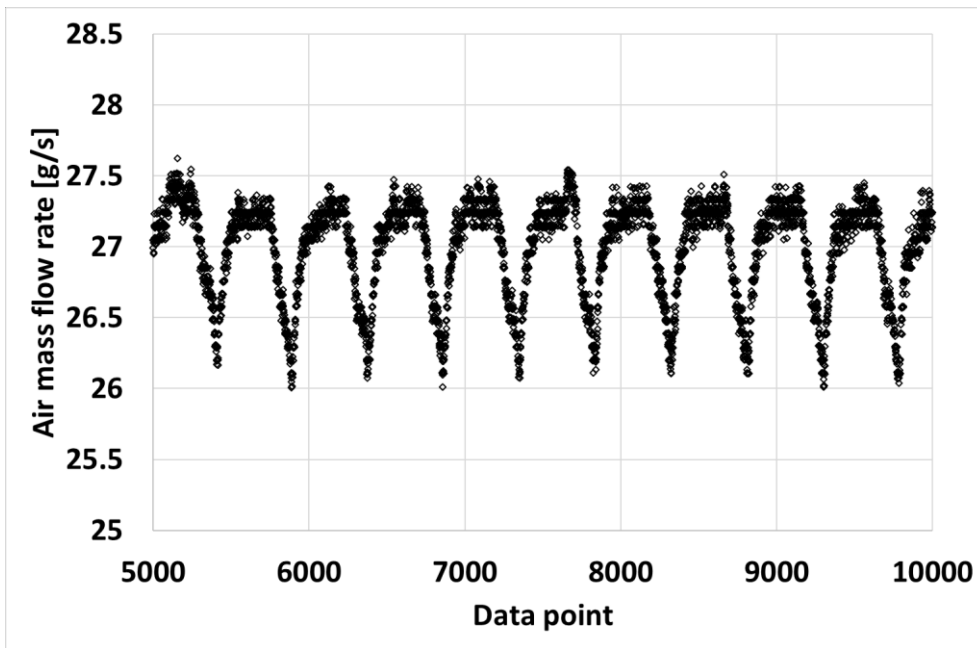


Figure 29: air mass flow rate for about 80 minutes of data acquisition

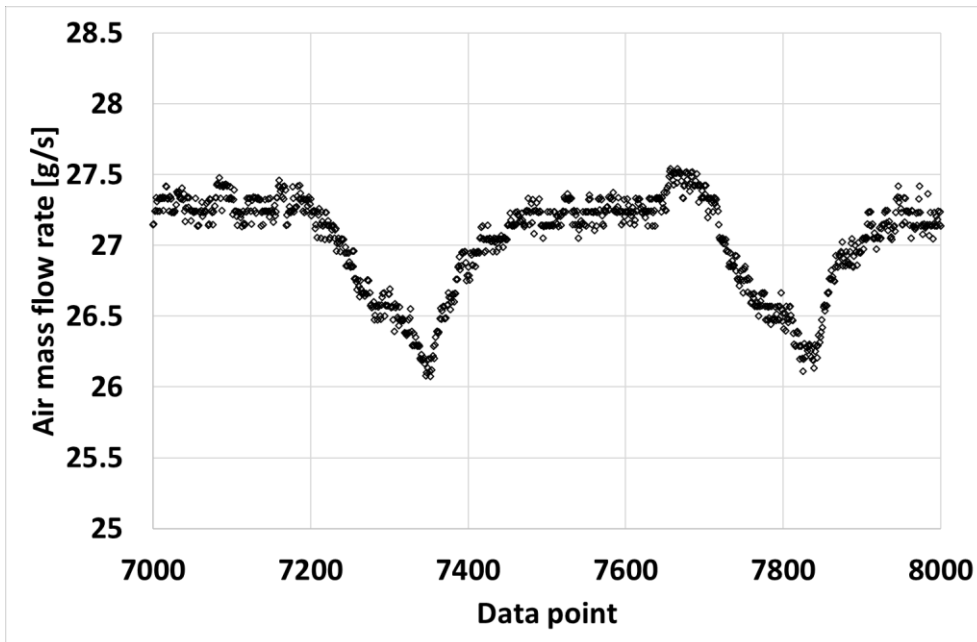


Figure 30: air mass flow rate for about 17 minutes of data acquisition

This fact affected, obviously with a greater inertia, the maximum air temperature achievable before the evaporator since, up to a certain limit, temperature increased for a lowering in the air flow rate and vice versa. This made the temperature control when running the heat torch at its maximum power quite difficult, risking a safety shutdown of the heat torch or a decrease in the performance of the expander, for a decrease or increase in the air flow

respectively. This was one of the reasons which led to consider an interval of ten minutes as the time window in which consider a steady state behavior for the cycle; the other was the thermal inertia of the refrigerant, given the size of evaporator and condenser.

Another observation that has to be made regards the prototypal nature of both the scroll expander and the pump: result which will be shown a few lines below regard preliminary run of the system adopting these two components. Probably because of this, when operating the expander at rotational speeds equal to 3000 rpm and 3600 rpm which correspond to the frequencies of 50 Hz and 60 Hz (which are the European and American electrical grid frequencies, respectively), high level of vibrations occurred, leading to the breakage of thermocouple wires after a few minutes of testing and impacting the pressure and refrigerant mass flow measurements (especially the latter, taken with the Coriolis mass flow meter). Several attempts were made to limit the influence of these vibrations on the instruments, but none were successful. It was then decided not to test the expander for these two values of rotational speed.

Given these introductory remarks, the ORC system was tested for the working conditions reported in Table 7. Four steps for pump rotational speed and five for the expander were set; the heat source temperature was set-up at its maximum value for the given conditions of environmental air at the inlet of the heat torch, which were variable between 20 °C and 22 °C as visible in the line of the condenser air temperature. The air flow rate reaching the evaporator and the condenser were fixed to 96.8 m³/h and 1869 m³/h respectively, where the latter value corresponds to the condenser fan rotating at its maximum speed.

Table 7: ORC system testing conditions

Property	Values
Pump frequency [Hz]	25, 27.5, 30, 32.5
Expander frequency [Hz]	25, 30, 35, 40, 45
Evaporator air flow rate [m ³ /h]	96.8
Evaporator air temperature [°C]	550
Condenser air flow rate [m ³ /h]	1869
Condenser air temperature [°C]	20-22

The first result shown here is the mechanical power at the shaft of the expander as a function of the pressure drop through the machine. Points reported on the graph are the representative value for each of the expander rotational speeds: for each expander rotational speed, there were values of the pressure drop or the pressure ratio through that machine which cannot be reached by the expander (the highest ones for the highest rotational speed and vice versa),

so are not reported in the next figures. We can see that a maximum of 600 W is almost reached for both the highest rotational speed between the one tested, which was 2700 rpm, and 2400 rpm, but this value is well below the target of 1 kWe. To quantify this fact with greater correctness, it is necessary to convert the mechanical power in electrical one thanks to the electric motor data, as showed a few lines above: doing so, an electrical output of 501 W results, which is almost half the target value. One explanation can be the presence of fluid leakages through the gaps of the machine: to test the correctness of this hypothesis, filling factor values were calculated for the different speeds. As can be seen from Figure 32, for increasing rotational speeds, FF decreases: this happens because when the expander is turning faster, the mass flowing through it matches the one delivered by the pump: however, the FF at the highest tested speed was slightly less than 2.3, meaning that a great amount of refrigerant was leaking through the clearances between the moving and fixed components.

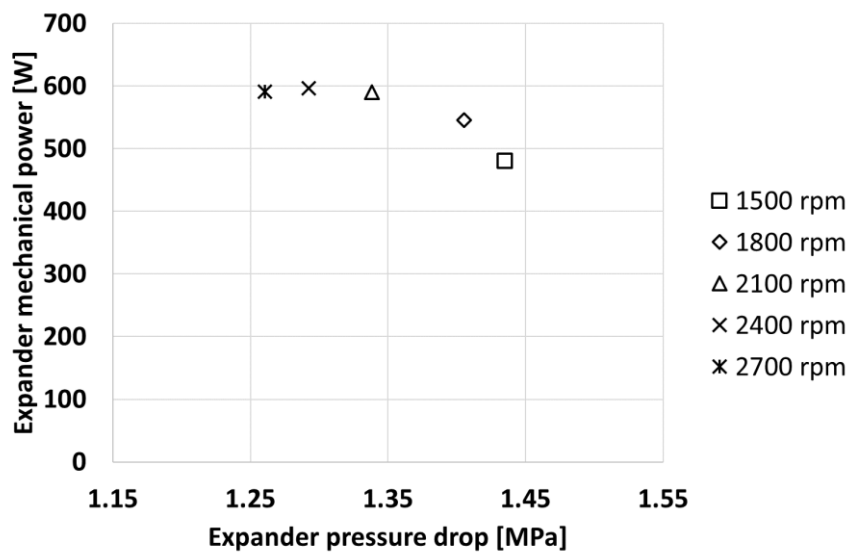


Figure 31: expander mechanical power as a function of expander

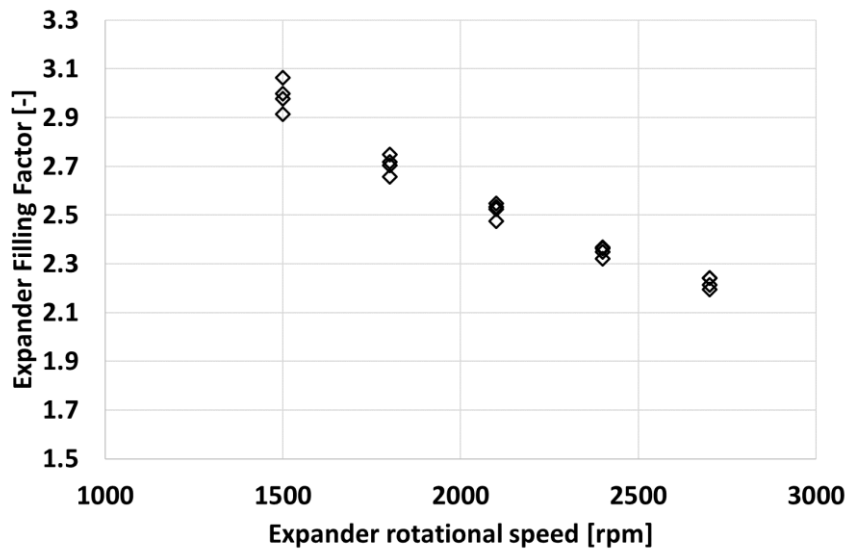


Figure 32: expander filling factor as a function of the expander rotational speed

By passing at the result of the isentropic efficiency of the expander, which showed a trend similar to the one of the mechanical power, it can be seen how the peak value of efficiency is quite limited, and this can be explained by the fact that the data reported in the graph below have been determined in range of expansion ratios between 2.5 and 3.3, while the internal volume ratio of the machine was 4.318.

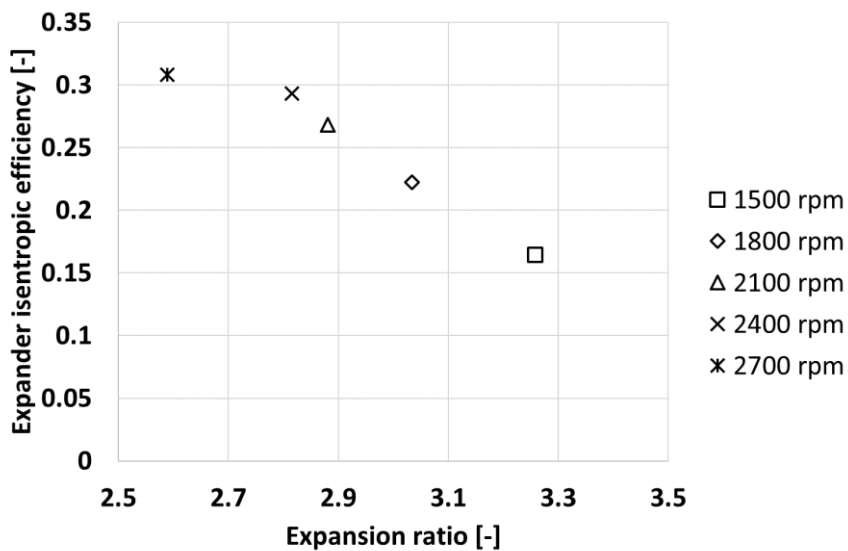


Figure 33: expander isentropic efficiency as a function of the expansion ratio

Because of the discrepancies between the expected performances and the actual ones, it has not been possible to validate the results obtained with numerical simulations with the data showed in the previous pages. For this reason, results regarding the analysis of the scroll expander have been compared with the ones provided by its manufacturer. These data, as

well as the ones relative to other devices which are typically employed in an ORC system, will be reported in the second part of the thesis (chapters 3 to 5), dedicated to the computational study of such apparatus.

First of all, in chapter 3 the focus will be put on the simulation of more than just a single system component, introducing the Whole ORC Model (WOM): in paragraph 3.2 a preliminary simulation showing the capabilities of the concept is showed, while in the following paragraph the results of a more in-depth analysis in which the effects of a variation in the working conditions of a system device are reflected on the upstream and downstream ones are shown.

The fact that it has not been possible to simulate a complete system by means of 3D CFD simulations because of the prohibitive computational effort required pushed towards the implementation of an approach able to link the models of the single system components into a whole, to save computational resources. The suggested approach is based on the use of a Python script which is able to transport the boundary conditions of a given system device (heat exchangers, expander and pump) to the one located downstream to it. In this way, it is possible to simulate each of these components with the most appropriate CFD tool, in terms of computational efficiency, reducing the physical time required to run the entire cycle simulation. The followed approach will be depicted in chapter 5, while the simulations of the individual components are reported in chapter 4: studies of scroll and single screw expanders have been carried out, as well as the one focusing on the heat transfer inside an heat exchanger.

WOM approach

3.1 Introduction

Although ORC systems are easy to manage, particular care must be taken in controlling and monitoring the system in order to avoid unwanted conditions. This is particularly true during transient conditions, in particular when the load request or the heat flow suddenly change. In particular, given the generally low value of the performance of these systems, the flexibility in following load variations can be an essential element to make the ORC cycle competitive with other solutions, or simply to make it adequate to the task assigned to it (such as, in fact, to be considered as a "peak-shaving" technology).

These problems should be addressed and possibly avoided in the design phase by using model-based techniques to simulate the transient behavior of the ORC system and thus be able to predict those operating conditions in which critical situations can occur. These methodologies have to be based on the availability of adequate models of each component that are able to correctly interpret the behavior of the system in both stationary and transient conditions. In the latter case, it is for example important that the proportion of the liquid and vapor phases in the condenser and the evaporator is maintained within acceptable ranges to avoid critical operation (stall, thermal shocks, uncertainty of the operating point, and so on).

In recent years, several dynamic models with concentrated or one-dimensional parameters have appeared and applied in the literature, even successfully. These models, however, require the mapping of the components into which the estimated parameters are entered starting from correlations or empirical information, often ad-hoc calibrated on the single component, or through 3D,CFD simulation.

Currently, however, there are still no CFD simulation attempts that integrate all the components in a single process to obtain a complete virtual model of the entire machine, which also includes information exchange between the components directly within the same three-dimensional model. The virtualization of the entire ORC system is to be considered

beneficial from the point of view of both the designer and the user under different perspectives:

- The simulation of each component in different operating points can be exploited to obtain the performance maps of the machines rather than the design parameters of interest such as the heat exchange efficiency of the heat exchangers;
- The virtualization of an entire ORC system could be used to build a virtual test stand: such a virtual device can be useful for testing off-design conditions rather than mapping the performance of each component and the mutual interaction during transient operations. A very important information that can be extracted from this approach is for example the position in which the liquid charge stops or, again, the change in the performance of the ORC system due to the amount of refrigerant charge. This is possible only if the transient behavior of each component and their mutual interaction can be simulated. The virtual test stand could also be very useful for predicting performance differences when a system component needs to be modified: for example, the use of a scroll expander rather than a piston expander can be simulated while simultaneously evaluating the interaction with all the other components. At the same time, different fluids could be virtually tested avoiding numerous problems related to the compatibility between the organic fluid and sealing systems or with the lubricating oil;
- The change in the performance of the ORC cycle over time can be studied by introducing the effect of aging of the components and the degradation of the performances connected to it. By way of example, a change in the geometry of the pump due to prolonged operation in cavitation conditions could be evaluated, rather than the combined effect of variation of geometry and increase in thermal resistance due to fouling of heat exchangers.

Given this, it is clear that just a few approaches are feasible when trying to simulate an entire ORC system without using 0D modeling for the components, at least for the main ones. These approaches regard on one hand the simulation of an entire cycle with 3D, CFD tools, on the other the simulation with these tools of only some of the system devices and the use of a 0D tool to model the others. Another one consists in neglecting pressure losses along the pipes and through the valves connecting the various elements and simply importing thermodynamic conditions from the exhaust of a given components to the inlet of the following one. Each of these approaches have its own pros and cons, which will be discussed now.

A full-3D simulation of an entire ORC system is the way in which the most of information can be harvested with a numerical tool: citing the examples reported above, it is the way in which the level of refrigerant in the various components can be seen, or how the geometry of the pump varies under cavitation conditions. By setting the most appropriate boundary conditions for each simulated component, it is possible to observe how heat transfer take place all along the system, or it is possible to check if hot or cold spots are present in the heat exchangers. Depending on the complexity of the simulation, also the heat transfer across the material of which the various system components are made can be modeled, by running Conjugate Heat Transfer analyses. The major drawback of such an approach consists in its computational cost: the simulation of an entire system requires the generation of numerical grids with several thousands or millions of elements, depending on the desired accuracy degree. Furthermore, most of the fundamental components of the system are untrivial to simulate themselves: for example, since we are dealing with micro systems, as reported before the expansion devices which are usually employed are the positive displacement ones. The problem in modeling such machines stays in the discretization of the expansion chambers, whose volume is obviously not constant with time. It is then required to generate a numerical mesh able to deal with this aspect, which can lead to a decrease in robustness of the simulation. Another problem is to find a simulation tool able to model, in the same simulation, phenomena such as evaporation and condensation, together with the motion of the moving boundaries in the expander and the pump. Furthermore, since the various components once virtually “assembled” will define a closed system, it is necessary to find a sufficiently robust CFD tool able to dampen phenomena such as pressure pulsations in the pipes connecting these components, which are detrimental in terms of numerical stability of the simulation, both if these are “real” pulsations or just numerical, induced by the startup of the model. This latter aspect introduces another fundamental characteristic of CFD simulations, which are the initial and the boundary conditions. The software user has to decide the value of several parameters, such as the initial fluid temperature, pressure and its level inside the various components, thermal specification of the boundaries (e.g. adiabatic, fixed temperature, fixed heat flux, ...), an average turbulence value in the cycle and so on. It is then apparent that this type of system modeling requires, apart from a great computational power, also a great knowledge of the system behavior, which can be difficult to know when running simulations of prototype solutions. Thus, sometimes is better not to focus on information like level of fluid in the piping across the system, but just on the behavior of the different machines existing in the system. For this reason, a simulation in

which information about thermodynamic state of the fluid at the outlet of each component is simply “copied” at the inlet of the successive device can be of great use.

Within this type of simulations, pressure losses in the piping can be neglected or modeled with simple mathematical relations, reducing the complexity of the simulation. Furthermore, in the previous lines it has been written that one of the issues of a full-3D approach is to find a CFD tool able to model both working fluid change of state and motion of the moving parts in pump and expander. By running a simulation for the pump, the evaporator, the expander and the condenser it is possible to overcome this fact by running each simulation with the most appropriate tool and then “connect” the exhaust port of each device with the intake port of the other by means of a script, which can be written in any third-party language. It is then clear that such an approach is far more flexible than a full-3D one, with the drawback of a loss of information between the various components.

Before showing the results of these two types of approach to the problem of modeling an entire cycle, a few words will be spent on the 0D model, which is frequently employed to study ORC systems.

A 0D model is an approach in which system components are replaced with an algebraic or differential relation, without its geometrical discretization: for example, a pump is modeled by using its characteristic curve, a pipe with his distributed losses formula, a valve with concentrated losses and so on. Once the entire system is modeled, one of the input quantities is perturbed and this causes the operating points of all the components to vary accordingly. In this way, it is possible to rapidly observe how the system behaves when one of its working parameters is varied: in fact, just one equation is solved for each device. While a fast solution is the strength of this method, it is also its weak point: modeling a component by means of a single equation introduces a great uncertainty, which can lead to results which are acceptable only when considering them under a qualitative point of view. Furthermore, if one wants to increase method accuracy to obtain performance maps of the components or thermal properties of the pipes, it is necessary to run at least one experimental campaign in which all these data are collected. A way to partially overcome these accuracy issues is to model a single device with more than one equation, where each relation is relative to a single part of the component. For example, considering a volumetric pump in which several compression chambers are present, it can be possible to implement an equation for each of these chambers, getting a better model of pump behavior as a function of rotational angle. Another example can be the modeling of the gaps between moving boundaries, such as the rotor and stator of pump or expander, which can be modeled as a source, or sink, of mass

and momentum. Again, the problem with this other approach stays in collecting the information for such a more comprehensive modeling: where the flow coefficient for the gaps can be obtained? Unfortunately, unless using approximate relations, this data comes from experimental analysis or CFD simulations. Despite these limits, several researchers have adopted this approach: Donghong et al. [59] used Dymola® to study the behavior of an ORC system in transient conditions, while Dickes et al. [60] ran different lumped parameter simulations in order to find the one with the best compromise between accuracy, complexity and robustness. Miao et al. [61] and Quoilin et al. [62] modeled the various system components with a semi-empirical approach and then the former author linked them together within Matlab® environment, while the latter used and EES®. Xu et al. [63] used Simulink® to create a dynamic model of an ORC system which recovered energy wasted by an heavy duty engine: Finite Volume Method (FVM) has been employed to model the evaporator, but the other cycle components were represented without any sort of discretization. A similar approach has been adopted by Huster et al. [64], in which for a same ORC application they ran a dynamic model where, this time, the heat exchangers were modeled with a moving boundary approach. In the analyzed literature, just a few researchers discretized one or more cycle components, mainly with the FVM and a few elements so, as suggested before, a quite novel approach to the whole system modeling should be of running 3D, CFD simulations of the main components such as the pump, the expander and the heat exchangers and then using a 0D model to “connect” them. In this way, a 0D-3D simulation is set-up.

A 0D-3D approach, also named co-simulation, can be of aid in several different occasions; such the ones here reported:

1. If a component performance map is not available, it could be too expensive to extensively delineate its behavior for all the possible working points of the system, because some zones in this map could never be explored during standard working conditions. It would be wiser, then, to calculate only those points of the map which are effectively reached during system operation, thus a CFD simulation could be of aid in determining them;
2. A similar case is when the system user or the designer wants to check what happens in the system when off-design conditions are reached, such as a temperature spike in the hot source or a sudden variation in the load connected to the expander. In these cases, the “standard” performance maps are of no aid, since the working point will likely stand outside the covered range;

3. Variations in the system layout or in the type of working fluid lead to a change in working conditions, thus it is necessary to evaluate how the different components of the system behave.

Given all these aspects, in order to switch from a full-0D simulation to a 0D-3D one, it is necessary to employ three different computational tools: the two 0D and 3D software together with the interface language, as already said several lines above. It has to be noticed that for each of these different tools several commercial and open-source instruments are available, with different levels of complexity. For example in several languages, such as Modelica®, libraries in which the modeling equations for pump, heat exchangers, expanders, valves and so on are available, and the user has just to modify the parameters on the base of the actual system configuration but there are other languages, such as Python, in which the user has to create from scratch the various models. A similar thing happens for 3D software, in which complexity and adaptability to the actual problem change between commercial and open-source ones and also among products having the same licensing type. Furthermore, one has also to choose between a general-purpose code or a tool created for just a class of devices, such as software oriented to positive displacement machines simulations.

It is then clear that different methods exist for the simulation of an ORC system, each one with its pros and cons, but with the fundamental premise that each device performance is affected by the operations of the other components which are present in the system; in this chapter, the focus will be put on the simulation of an entire, actual ORC system by means of a full-3D (yet simplified) CFD simulation in order to show the first steps made in WOM, which is the Whole ORC system Modeling. Then, an example on how this approach can also be applied to just a section of the same ORC system will be given.

3.2 WOM concept

3.2.1 Introduction to system modeling

A simplified model of an actual ORC system will be shown in the following lines. The system under analysis is a test cycle located in University of Bologna laboratories, whose experimental characterization has already been done by Ancona et al. [65] and Bianchi et al. [66] [67] and thus data regarding working fluid mass flow rate and temperature and pressure at the intake and exhaust ports of the various system devices are available. Thanks to the presence of these studies, it has been possible to choose a single working point of the system from which derive the boundary conditions for the numerical model. Transient simulations using STAR-CCM+® CFD tool have been run, in order to have an insight on the distribution

of the refrigerant inside the circuit, starting from an initial condition in which both the condenser and expander were filled with both liquid and vapor R134a. Other useful pieces of information which have been possible to obtain were the ones regarding heat exchange and liquid-to-gas fraction. Given this, the actual ORC system and its P&I diagram are showed in Figure 34.

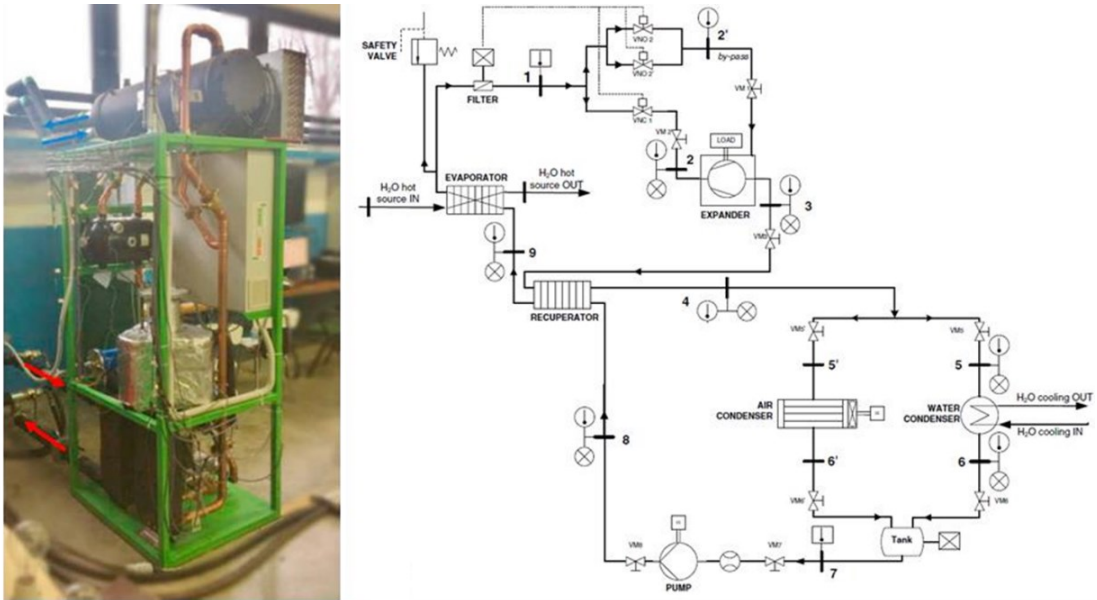


Figure 34: left: ORC system [66], right: P&I diagram

As visible from the scheme in the previous picture, the ORC system features a regenerator placed at the outlet of the radial, three-piston expander, with a nominal power output of 3 kWe. The working fluid mass flow is controlled by means of an inverter operated external gear pump, while fluid condensation is made with a shell and tube heat exchanger whose cold medium was cold water. On the other hand, refrigerant is evaporated thanks to a brazed plate heat exchanger, with hot water as heat source. To monitor the operating conditions of the system, T-type thermocouples and ceramic pressure transducers are fitted upstream and downstream of each cycle main component and mass flow rate is measured thanks to a Coriolis flow meter.

3.2.2 Simulation set-up

Given the novelty of the approach introduced in these lines, one of the objectives of the WOM concept was to obtain fast and reliable multiphase simulations. Because of this, several simplifications have been adopted for both the heat exchangers, the pump and the expander. As visible in Figure 35, where the numbers present in the right hand side of the picture are the same as the one reported in Figure 34, the CFD model was made up of the evaporator, a pressure-reducing valve which acted as the expander, the condenser and a tank.

The overall dimensions for this model reflected the ones of the actual system, since the numerical domain was 2.7 m high and 1.7 m wide.

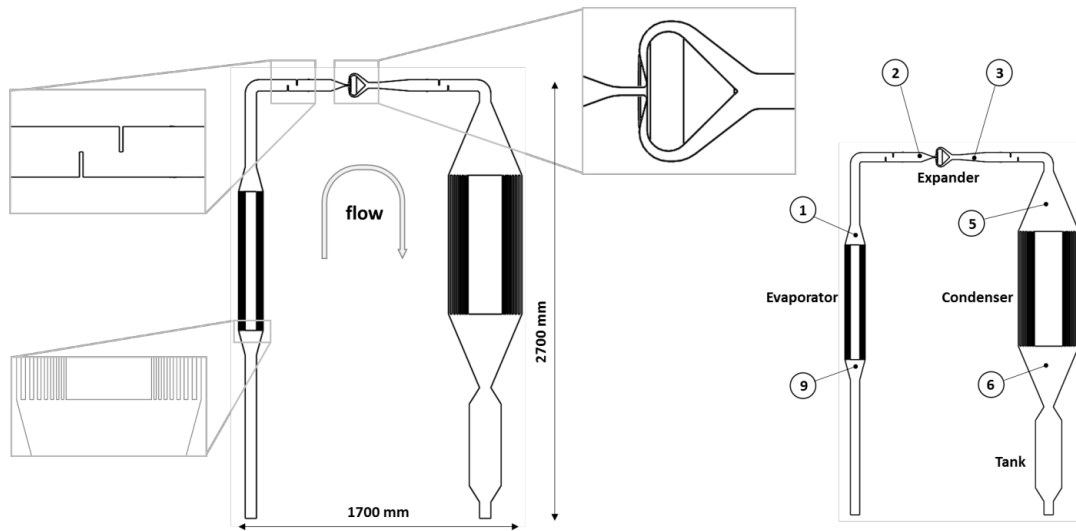


Figure 35: CFD model of the system presented in Figure 34

Describing the previous figure from the left branch, we have that the liquid enters the system from the bottom of the evaporator, it becomes vapor and then it reaches the pressure-reducing valve through a duct in which a couple of fins have been inserted to dampen pressure pulsations, which can negatively affect simulation stability if they take place, given that the valve has been designed for a well-defined mass flow rate and fluid density. After the expander, the vapor reaches the condenser in which is cooled down up to the liquid phase and then is admitted in the tank.

Considering the single devices, the computational models for the evaporator and the condenser have been designed to have the same volume as the real components, even if their geometry is totally different. In fact, heat exchangers models are made of a series of coaxial tubes with rectangular section, totaling a number of sixteen surfaces which exchange heat with the surrounding fluid, as it is possible to see from the evaporator cut section on the left-hand side of Figure 35. This section is also valid for the condenser, with the only difference that it is scaled up to accommodate an internal volume which is almost nine times the one of the evaporator, because the latter is a compact plate heat exchanger, while the condenser is a shell and tube one. From the same figure it is noticeable how the two exchangers have been placed in the numerical model with their main axis aligned in such a way the fluid phase change was facilitated, considering the direction in which gravity force. Another peculiarity of these two devices is given by the fact that their inlet and outlet sections have been modeled

in order to reduce fluid recirculation: this has been accomplished by means of divergent and convergent layout, respectively.

Other two simplifications were introduced to model the expander and the pump whose simulations, even if feasible with the CFD tool employed in this analysis, for the study which is to be presented would have been too time consuming. So, the former machine has been modeled with a valve with fixed lift, calculated in order to obtain the experimental pressure ratio across the expander. On the other hand, the pump has not been modeled at all and its presence has been simulated by imposing at the inlet and outlet section of the system the discharge and suction pressure of the pump, respectively. System main characteristics are reported in Table 8.

Table 8: main properties of system components

Component	Properties	Value
Evaporator	Number of heat-exchanging surfaces	16
	Heat exchange area [m ²]	5.710
	Volume [l]	8.10
Expander	Expansion ratio	2
	Valve lift [mm]	0.3
Condenser	Number of heat-exchanging surfaces	16
	Heat exchange area [m ²]	17.13
	Volume [l]	72.9
Piping	Hydraulic diameter [m]	0.0694

3.2.3 Mesh and numerical model

The numerical domain has been discretized with a computational grid consisting in 21.5 million of polyhedral elements. As visible in Figure 36 and Figure 37, mesh was refined in locations such as the volume between the heat exchanging surfaces of the heat exchanger and in proximity of the throat section of the expansion valve. From these two pictures are also visible the prism layers generated on those surfaces, to increase the stability of the numerical simulations and to increase the modeling accuracy of the heat transfer process: for the heat exchangers, a total height of 1mm was modeled with five layers of prismatic cells, with the first centroid placed at 36 μm from the wall. In the case of the expander, just four layers have been modeled, because of the limited distance between opposite surfaces. In the rest of the domain, polyhedral elements with dimensions up to 5 mm were generated, with such a size decided in order not to greatly increase the total number of elements while maintaining y^+ values in a range which fits the all- y^+ approach adopted in this study.

To model mass transfer, in the current study the Volume of Fluid (VOF) method has been used together with fluid film evaporation and condensation model for the refrigerant

considered as an ideal gas, both to reduce computational effort and because of the presence in the heat exchangers of both stratified and mixed flows. The VOF method, which utilizes an Eulerian representation of the flow field, was described for the first time by Hirt and Nichols [68] as a tool to model multiphase flows with the hypothesis of same pressure, temperature and velocity fields for all the phases defined in the domain.

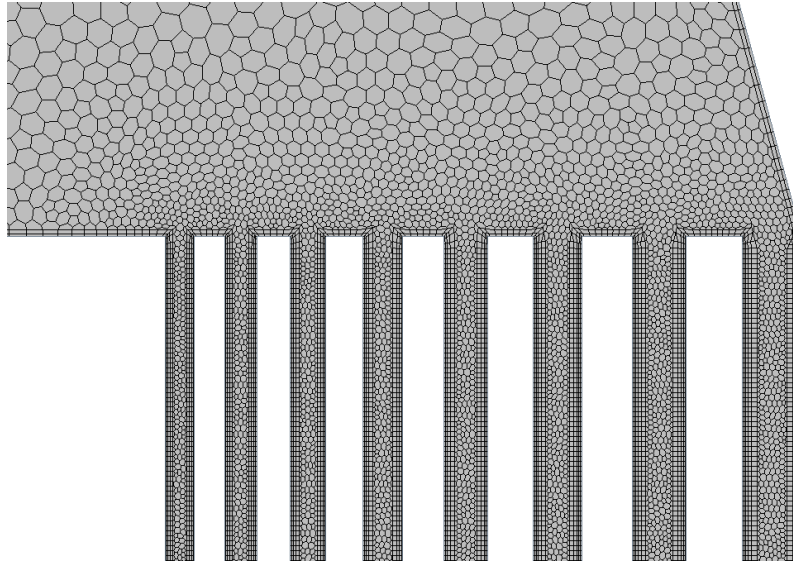


Figure 36: detail of mesh in one heat exchanger

To locate the interface between the two phases for each grid element, this method is based on the local average value of a function. So, for a given cell, this function assumes a value between one (liquid only) and zero (vapor only). In addition to the position of the interface, another required information is the direction in which it moves: this datum is provided by the direction in which the gradient of the function is greater.

Another issue given by the simultaneous presence of both stratified and mixed flow is the need of small overall mesh size to obtain a robust simulation. To overcome this fact, it has been necessary to couple the VOF method with the fluid film model through the resolved fluid film model: in this way, it has been possible to generate relatively coarse mesh in the background, thanks to the transition between the VOF method and the fluid film model made using a user-defined transition volume fraction value. Given a computational cell, when the volume fraction of the liquid in the neighboring cell is greater than a user-defined value, the software manages the transition of the fluid film into one of the VOF phases and vice versa. Since the fluid film model is based on the creation of the so-called shell regions, which enclose the boundaries in which a fluid film is supposed to exist, these regions have been generated only on those surfaces in which the refrigerant phase change is likely to occur, namely the internal surfaces of the two heat exchangers. Within these regions, the fluid film

model solves the transport equations for energy, mass, momentum and volume fraction to determine several properties like fluid film temperature, pressure, thickness, distribution and volume fraction in the neighboring cells. This model also required the definition of a couple of parameters: the first, was the surface tension between the phases, to account for the immiscibility of liquid and vapor while the second was the contact angle between the liquid and the wall (wet or dry contact).

Once the models have been set up, the global simulation parameters were defined. The time step value for the transient simulation was set up to $1e-6$ s and a compressible solver was chosen to deal with the multiphase flow and interface tracking, while the turbulence has been modeled with the one-equation model of Splart and Allmaras [69]. The R134a working fluid properties and boundary conditions for the CFD model are reported in Table 9.

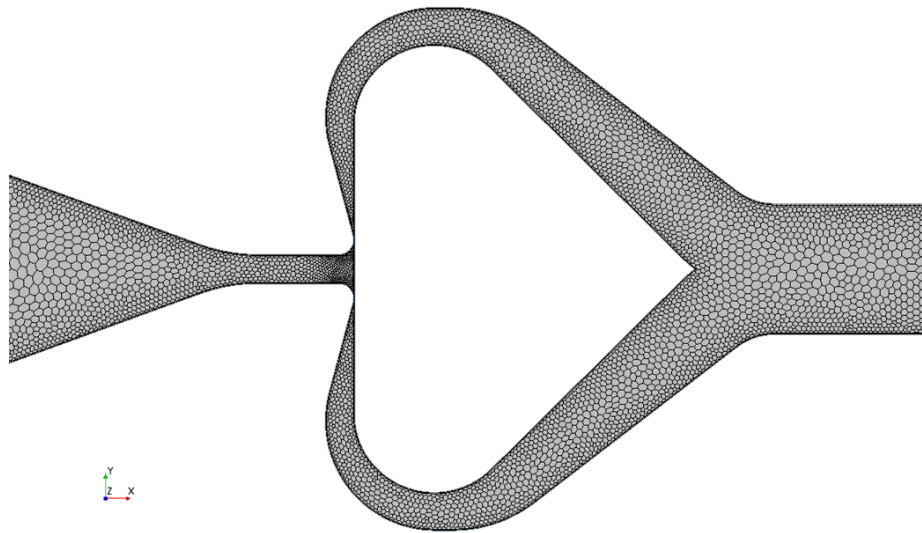


Figure 37: detail of the expander mesh

Table 9: model boundary conditions and refrigerant properties

Property	Value	Property	Value
Evaporator wall temperature [K]	351.0	Liquid viscosity [Pa s]	1.744e-4
Condenser wall temperature [K]	283.2	Liquid thermal conductivity [W/m K]	0.07749
Liquid mass flow rate [kg/s]	0.1	Liquid-vapor surface tension [N/m]	4.610e-3
Liquid inlet temperature [K]	308.6	Vapor specific heat [J/kg K]	1235.0
Liquid inlet pressure [MPa]	1.8	Vapor Density [kg/m ³]	82.85
Liquid specific heat [J/kg K]	1458.5	Vapor viscosity [Pa s]	1.437e-5
Liquid density [kg/m ³]	1172.3	Vapor thermal conductivity [W/m K]	0.01919

3.2.4 Results

Steady state conditions of both the expander and the heat exchangers were reached after a physical time of 90 seconds, after which pressure and temperature field of the working fluid inside the numerical domain looked like the ones reported in Figure 38.

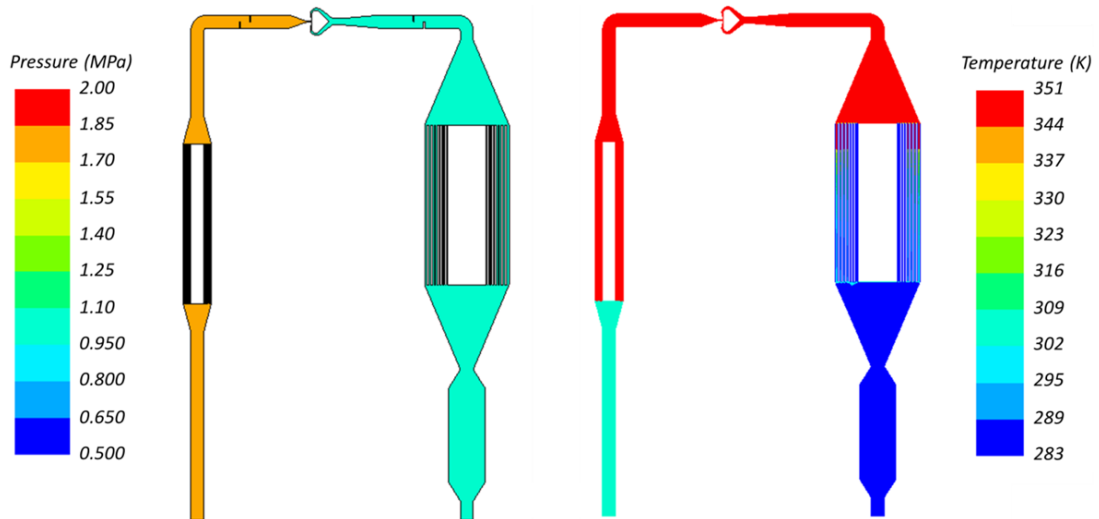


Figure 38: pressure (left) and temperature (right) fields inside the circuit

From the image on the left-hand side, we can see that the two branches of the system, before and after the expander, are at constant pressure. In fact, pressure losses along the pipes and the exchangers are, even if existing, limited and the pressure reducing valve is responsible for a pressure drop equal to 1.7, from 1.77 MPa to 1.02 MPa.

On the right-hand side, it is visible how extreme superheating and subcooling values are present in the evaporator and in the condenser, respectively. The high temperature in the evaporator leads to refrigerant vaporization as soon as it enters the device, while in the condenser it is possible to see how temperature drop, and thus phase change, is more gradual. Even if this happens, we can see that at the outlet of the condenser and inside the receiving tank the fluid is completely at its liquid state, as it is also showed in Figure 39.

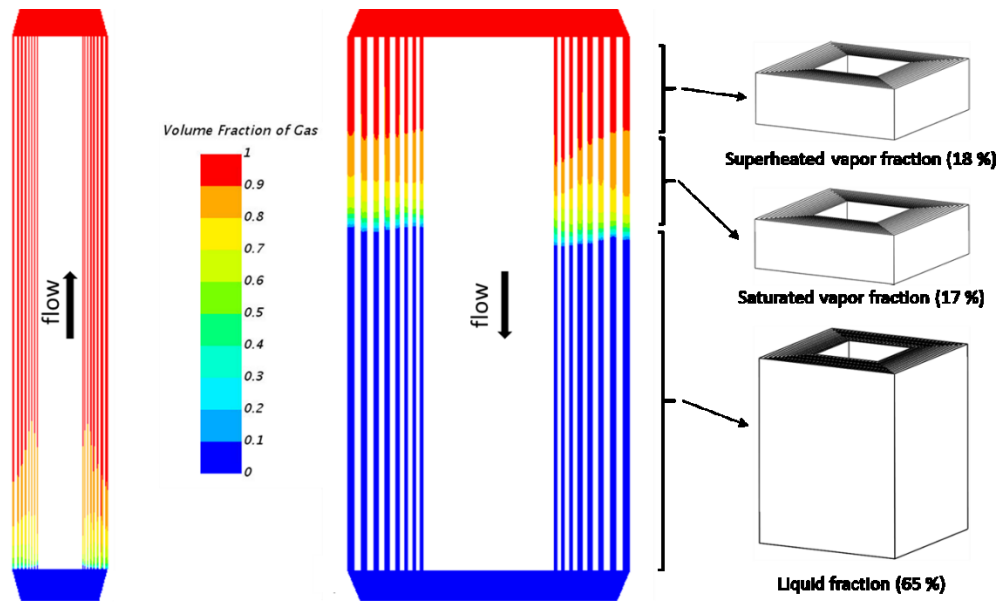


Figure 39: change in fluid state in the evaporator (left) and condenser (right)

The previous picture shows one of the peculiarities of the WOM approach, which is the ability of showing the level of liquid inside the exchangers; on the right-hand side, also the different fluid states are reported and show how, in this case where the total volume of the condenser is around 73 liters, the 65 % of it is occupied by liquid refrigerant, while the remaining volume is half superheated vapor and half saturated gas. This latter information can be inferred by querying a thermodynamic library, such as Coolprop [52] or REFPROP [70], to retrieve entropy and enthalpy values as a function of temperature and pressure. In this study, this was done thanks to REFPROP v7.0 library and fluid states at the inlet and at the exhaust of the various devices have been calculated, see Table 10. From the data presented in this table, it has been possible to plot the p-h diagram (Figure 40) showing the transformations which occur in the circuit.

Table 10: thermodynamic properties of refrigerant in relevant sections of the circuit

Point	p [bar]	T [K]	h [kJ/kg]	s [kJ/kg K]
9 - Evaporator inlet	17.73	308.6	249.59	1.1664
1 - Evaporator outlet	17.71	350.3	446.73	1.7582
2 - Expander inlet	17.69	349.5	445.78	1.7555
3 - Expander outlet	10.15	349.1	457.97	1.8278
5 - Condenser inlet	10.12	349.0	457.91	1.8278
6 - Condenser outlet	10.08	283.2	213.75	1.0474

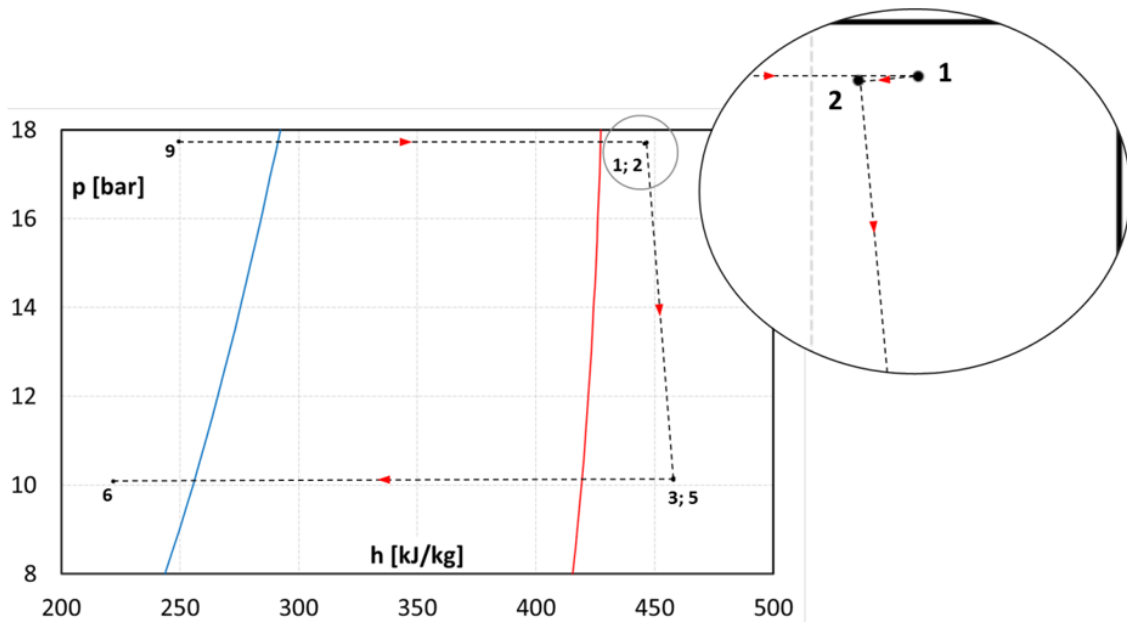


Figure 40: p-h diagram of the simulated ORC system, transformation in the duct upstream the evaporator magnified

In Figure 40 it is possible to see some of the system peculiarities already depicted, such as the high degree of subcooling (point 6 is far from the saturated liquid curve, the blue line), but it is also visible an unexpected transformation which occurs in the pipe between the outlet of the evaporator and the inlet of the expander. From the magnified area on the right-hand side of the picture, it is visible how pressure slightly decreases, while enthalpy does it in a steeper way. This is probably given by the presence of the fins, modeled to prevent pressure waves to travel across the pipe: these fins introduce an additional pressure drop, beyond the head loss of the duct. This causes the enthalpy drop and, also, the temperature reduction, as visible from Table 10 (walls of the numerical domain have been modeled as adiabatic); this effect is also given by the fact that the temperature value reported so far it is the static one. Since the cross section of the duct varies from rectangular to circular, the fluid accelerates and a conversion of static temperature in dynamic contribution takes place.

Another parameter which is useful to predict how the heat exchangers behave under actual working conditions is the temperature evolution inside the exchangers. In Figure 41, from the picture on the left, it is visible that the phase change takes place in a small region of the heat exchanger, because of the effects of both the high temperature of the walls and an extended heat-exchange surface. The same happens for the condenser, picture on the right, but with an even higher rate, since the surface is greater, when compared to the one of the evaporator.

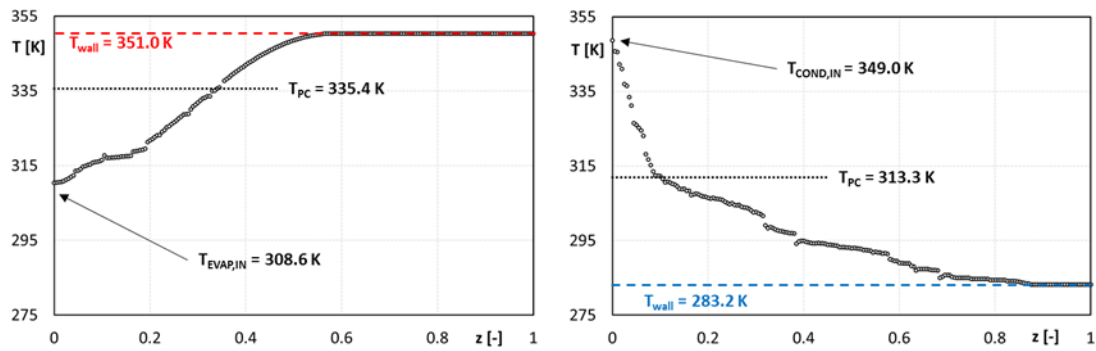


Figure 41: temperature profile inside the evaporator (left) and condenser (right) as a function of the normalized height of the heat exchangers

Even if the results shown up to this point are relative to an idealized ORC system with fictitious (yet simulated with actual boundary conditions) components, it is clear that such an approach can truly provide useful information to both the user of such a system and its manufacturer, since data such as the level of liquid inside the exchangers rather than the temperature profile inside of them can be obtained. From this idealized work is then natural to study the same ORC system again, but with the actual geometry of its constituting components.

3.3 WOM development

3.3.1 From the concept to an actual application

One thing which is possible to notice from the system depicted in the previous paragraph is the absence of the pumping system, which has been justified with the need of implementing a simple concept to conduct a feasibility study for the approach. Given the encouraging results, a further step has been made towards a more representative simulation of the real system. This time, the complete pumping system portion of the cycle studied in [65] has been modeled. This was done in order to analyze a couple of phenomena which can often happen in ORC systems, namely the fluid cavitation in the pump and pressure pulsations induced by its operation: results shown in this paragraph are taken from the work published on Energies [71]. Generally speaking, for micro-ORC applications, positive displacement pumps are used and, among these, external gear pumps are quite common: in fact, that is the type of pump used in the considered cycle. One of the peculiarities of these pumps is given by their high sensitivity to cavitation phenomena, especially for increasing values of rotational speed. High values for this parameter are adopted, apart for increasing the mass flow rate, to reach high values of volumetric efficiency; the fact is that at the highest speed the combined action of both pressure losses and narrow gaps can lead to localized pressure drops and thus cavitation [72] [73]. In ORC systems this problem is much felt, since the

thermodynamic state of the liquid at the inlet of the pump is not that far from the saturated liquid curve as showed in Figure 40, but is very close to saturation: this leads to a phase change for even pressure fluctuations. In the long run, cavitation leads to erosion of the teeth profiles and thus a reduction in the delivered mass flow rate and, at the end, to a premature substitution of the component. While cavitation affects just the pump, pressure pulsation are detrimental for the entire system, since vibrations are easily propagated through the entire system, since pipes are usually not able to dampen them. Unfortunately, this frequently affects the different measures taken in the system (such as temperature and pressure ones) because of disturbed signals and also physical damage of the sensor itself. Without incurring in the latter, severe issue, disturbed signals can lead to an increase of the uncertainty in the measured variables. This is particularly true [74] [75], because of its measuring principle [76], for the Coriolis mass flow meter, which is one of the most used refrigerant flow meters in the micro-ORC field.

To analyze the impact of these two issues on the pump performance, the section of the system including the buffer tank, the Coriolis meter, the pump and the regenerator has been studied with a 3D-CFD analysis. As it is possible to see from Figure 42, which depicts the simulated section, also the piping bends and the internal layout of the flow meter were modeled, trying to determine in the most accurate way the thermodynamic state of the fluid entering the pump. But looking at the picture, is visible that also a component downstream the pump has been modeled, namely the recuperator. This was done to investigate the effects of the pumping process also in the first component placed downstream the pump, besides the ones placed on the upstream branch. In fact, in the current work the influence of the pump operation was assessed also with respect to the pressure pulsation of fluid inside the Coriolis meter, whose internal geometry has been modeled too.

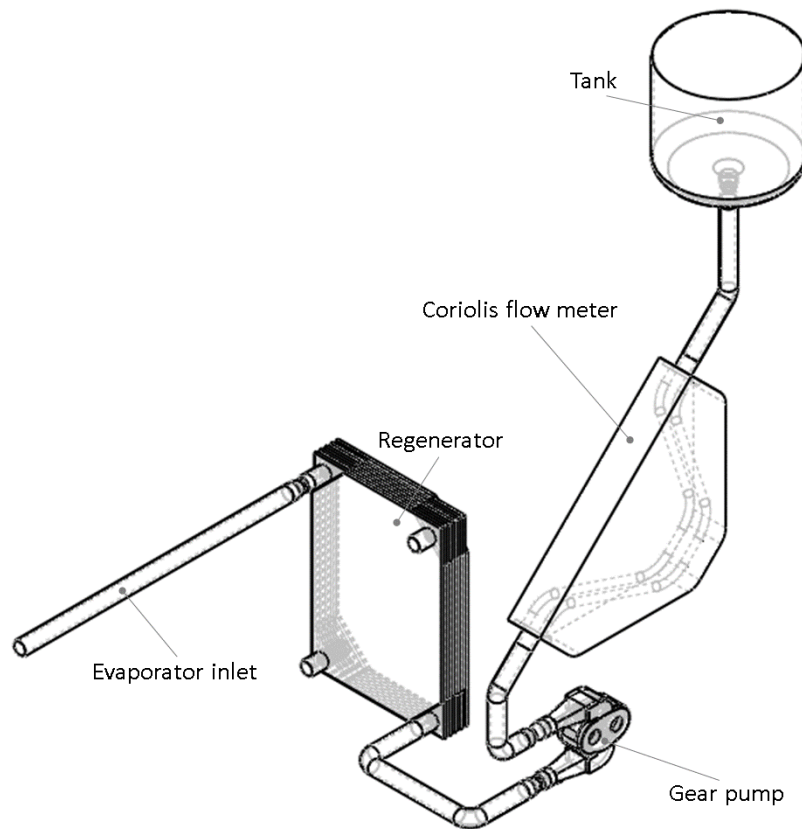


Figure 42: simulated system section, with details of the internal geometry

3.3.2 Numerical model

3.3.2.1. General approach

Both the generation of the computational grid and the numerical simulation of the system portion reported in the previous picture were done using Simerics Pumplinx[®] 4.6.4. Stationary domains (e.g. the Coriolis meter, the regenerator, etc.) were meshed by means of cartesian elements (Figure 43), while a body-fitted curvilinear mesh was generated for the pump (Figure 44, which shows how the rotating and fixed domains of the pump are modeled). Since heat transfer was neglected, it has been possible to generate meshes with a low overall number of elements if compared to the WOM concept case, around three million versus more than twenty-one. On the other hand, also in this case finer mesh elements were generated where variation of the flow passage area occurred, such as restrictions or bends of the pipes: for this reason, a number of elements varying between 20 and 30 was generated along pipe diameter. For the moving parts, the dynamic mesh approach was adopted in order to analyze with greater accuracy fluid flow transient properties during pump operation: more than $3e5$ structured, hexahedral elements have been associated with a deformation algorithm to simulate the rotation of the pump wheels and the engagement of their teeth, with this peculiarities causing the modification, for every single time step, of the shape of the

numerical domain. This is visible from Figure 45, which shows three consecutive instants in which the two wheels rotate and the teeth engage: the mesh elements in the vane of a wheel are able to change their shape, adapting for the presence of the tooth belonging to the other wheel. As inferable from Figure 44, the suction and discharge ports of the pump are connected to the rotating mesh through a sliding interface.

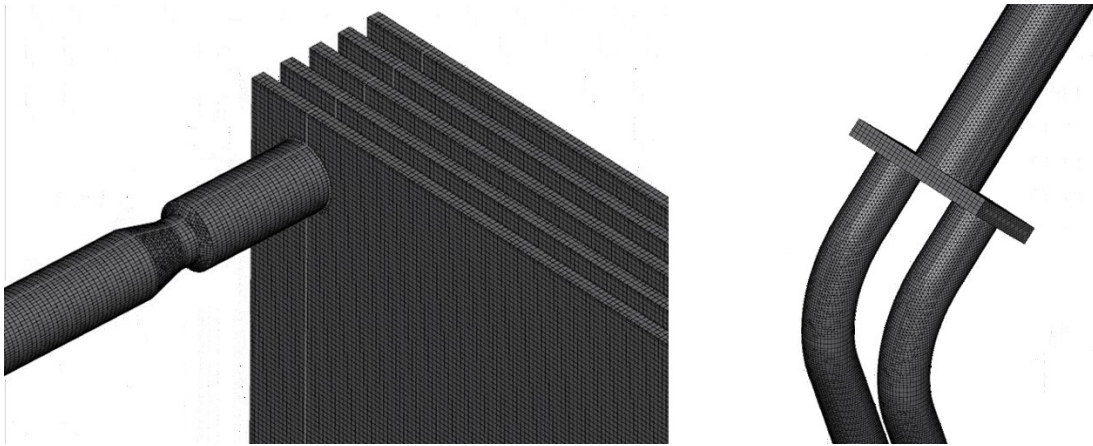


Figure 43: detail of the mesh on the regenerator (left) and Coriolis flow meter inlet (right)

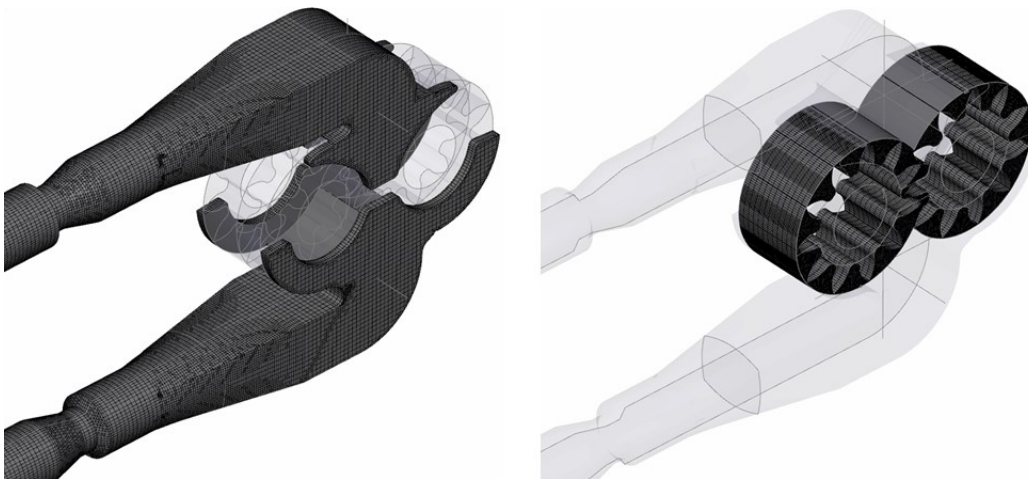


Figure 44: detail of the mesh for the stationary parts of the pump (left) and for the rotating domain (right)

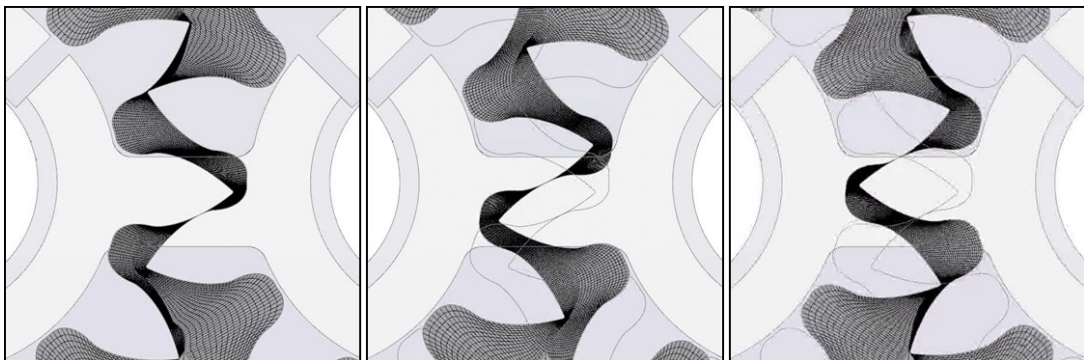


Figure 45: engagement process

3.3.2.2. Gear pump characteristics

The nominal displacement of the external gear pump ($7.5e-6 \text{ m}^3$) is always affected by the leakages that characterize positive displacement machines, in the engagement region and between the rotors and the housing, which are the tooth flank – pump housing and tooth head – pump housing periphery ones). The fluid flows through these gaps from the outlet port to the inlet port, because of the pressure gradient, leading to a volumetric efficiency well lower than one.

An axial clearance does exist between the wheels and the pump housing and is characterized by a width of $20 \mu\text{m}$; in the numerical model, it has been discretized with five layers of hexahedral elements coupled with the rotating wheels by means of a sliding interface (Figure 46). Another clearance is present between the tooth head and the housing, but this time it is not constant but it depends on the angular position of the wheel, varying between $50 \mu\text{m}$ and $100 \mu\text{m}$. This variability is given by the fact that the wheels are subjected to unbalanced forces given by different pressures: there is a wheel region which faces the delivery port, thus it is exposed to high pressure, while the teeth facing the suction port are facing a low pressure: this cause the wheels to operate in an eccentric position with respect to the pump housing, leading to lower values for the tooth – head gap in the adjacency of the suction port. To better visualize this phenomenon, a polar diagram is reported on the left-hand side of Figure 47, together with a detail of the generated computational mesh between the tooth head and the housing. In the polar diagram, the suction region is represented in the upper part, while the delivery section in the lower part. It is possible to notice that the gaps increase during rotation, starting from $70 \mu\text{m}$ up to $100 \mu\text{m}$. These clearances have been discretized with the same number of elements used to discretize the vane volume, which is equals to sixteen. This is visible in Figure 47, where the computational mesh in correspondence of the tooth head – pump housing gap is showed: this particular mesh topology is given by the deformation strategy adopted to generate the computational grid.

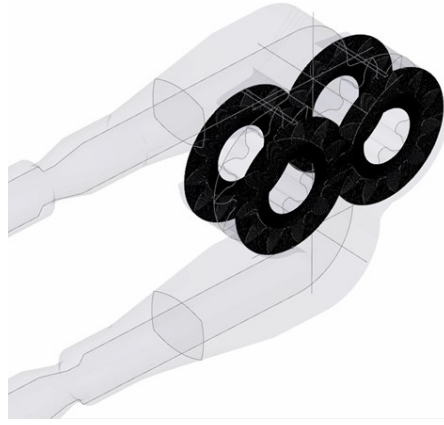


Figure 46: gaps between tooth flank and pump housing

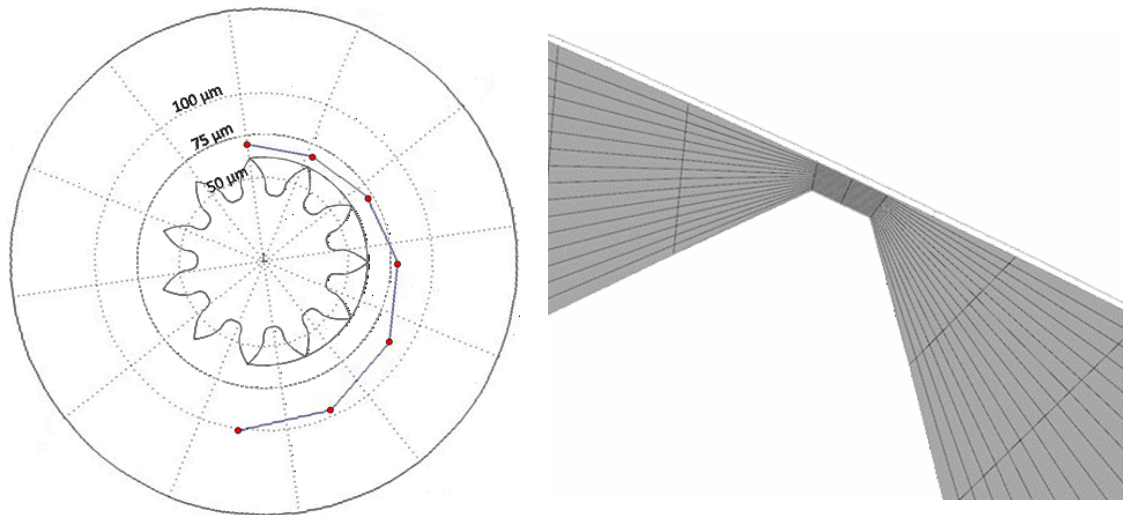


Figure 47: polar diagram of tooth head – pump casing gap width (left) and detail of the numerical grid for the same gap type (right)

The last type of leakages which are encountered in external gear pumps is given by the flow escaping the region in which the two wheels engage. When two pairs of teeth engage, a trapped volume arises which could lead to a sudden change in pressure if the trapped volume decreases, because of a wrong design of the pump [77]. Not to incur in this issue, the trapped volume is always connected to the high- or low-pressure domains by means of pockets, named relief grooves, which are engraved in the lateral side pump housing and whose dimensions need to be carefully designed because they influence the device dynamic behavior. The radial extension of the relief groove has to be chosen in order to both prevent pressure peaks given by the trapped volume and limit the flow leaking from the delivery port to the suction one, because of the pressure difference. In Figure 48, the position and shape of the relief groove are depicted: taking a look at the two consecutive instants, on the left-hand side of the picture this groove is initially connected to the upper and lower ports (which are the suction and discharge one, respectively) and then, right-hand side, it is sealed thanks

to the contact between the two tooth pairs, avoiding fluid to flow from the discharge to the suction port.

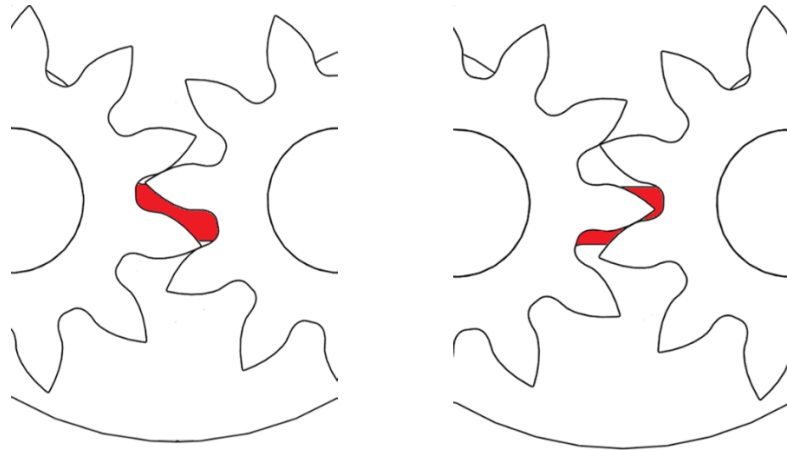


Figure 48: relief groove. Upper and lower ports communicating (left), suction and discharge ports isolated (right)

The backflow from the high-pressure port to the low-pressure one through the relief groove not only is detrimental from the point of view of a decrease in volumetric efficiency, but it also leads to pressure pulsations which travel up to the suction port of the gear pump, affecting the flow field. This happens because in this zone a high-pressure stream of fluid coming from the relief groove experiences an abrupt pressure drop, facilitating cavitation phenomenon.

3.3.2.3. Operating conditions

As introduced in paragraph 3.3.2.1, no heat exchange in the regenerator and heat dissipated through the walls of the numerical domain to the surrounding environment were considered, since the main aim of the study was to analyze the dynamic behavior of the considered system section. Given this, the value of the time step adopted to do this analysis was sufficient to solve a rotation of 0.5° of the toothed wheels.

A pressure of 0.601325 MPa has been imposed to the liquid in the buffer tank installed upstream to the pump, while at the regenerator outlet a pressure of 1.601325 MPa can be found. These two pressure boundary conditions are in agreement with the working point reported in [78] and are restricted by the system heat source and sink, with temperatures between 60°C and 90°C for the former and between 18°C and 25°C for the latter.

To obtain the target value of 0.1 kg/s for the R134a refrigerant mass flow rate, according to the pressure boundary conditions depicted above, the gear pump rotational speed has been varied between 450 rpm and 475 rpm. Since, as stated in the previous lines, the pump

operation is disturbed by the presence of both leakages and liquid cavitation, the target mass flow rate was reached by varying pump rotational speed as a function of the liquid subcooling occurring at the condenser. A given degree of subcooling determines the liquid saturation pressure, which is the most important parameter to consider in avoiding cavitation phenomenon. Starting from a reference condition of 450 rpm for pump velocity, 293 K for liquid temperature and 0.569060 MPa for saturation pressure, another couple of working conditions have been simulated

3.3.2.4. Model validation

The two values of pressures reported in the previous paragraph for the fluid in the tank and the liquid at the inlet of the evaporator were the ones applied to the inlet and outlet sections of the numerical domain (thus, 0.601325 MPa and 1.601325 MPa respectively). Density and viscosity for the refrigerant adopted as working fluid (R134a) were taken as constants, with values of 1226 kg/m³ and 2.02e-4 Pa s respectively. The phenomenon of cavitating gas has been modeled thanks to the “equilibrium dissolve gas” model implemented in Pumplinx tool [79]. Given these last simulations details, the numerical model was then validated against the data reported in [78]. A sensitivity analysis has been run to find the numerical mesh which could offer a compromise between computational time and accuracy in reproducing the experimental results. In Figure 49, a comparison of the mass flow rate obtained with the numerical tool and the one measured on the test stand is reported as a function of pump rotational speed. The mass flow rate values herein reported were taken as an averaged value of the instantaneous ones provided by the pump. When considering the value of the error bars, which are set to 10 %, it can be said that data are in reasonable agreement, especially for the highest rotational speeds. In fact, for the lower ones, the presence of lubricant in the real system (between 3 % and 6 %) leads to a better sealing of the axial and radial gaps, thus the measured values for the flow rate are greater than the ones calculated by means of the CFD simulation.

3.3.3 Results: Pump behavior

The results of the transient analysis conducted by means of the dynamic mesh approach are now reported. The various graph depicted in this paragraph refer to a 32.7 degrees rotation window, because each wheel is composed of 11 teeth.

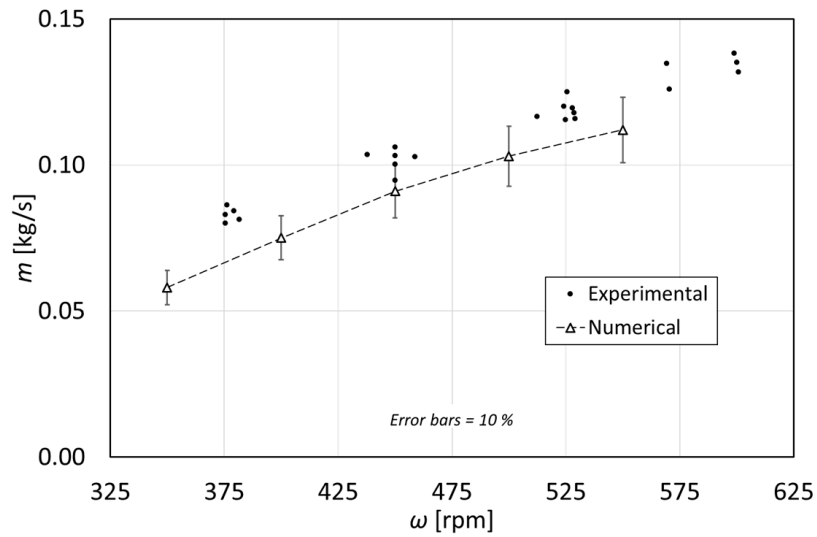


Figure 49: comparison between simulation results and experimental data

The first result to be showed is the mass flow rate at the outlet section of the regenerator as a function of the rotational speed of the pump, depicted in Figure 50. It is possible to see that the reported trend is not constant, but it follows the operations of the pump, which provides a certain amount of refrigerant as a function of the angular position of its wheels: taking α as the reference angular position, the peak of flow rate is given by the fluid vane discharged at the pump outlet section. Given the time resolution of the simulation, it has been possible to calculate with acceptable accuracy the average mass flow rate handled by the wheels during their rotation: for the nominal rotational speed, which is 450 rpm, the value for the average mass flow rate is 0.091 kg/s. This value is given by the concurrent presence of both the fluid released at the discharge port and the leakages given by the pressure difference between the inlet and outlet ports.

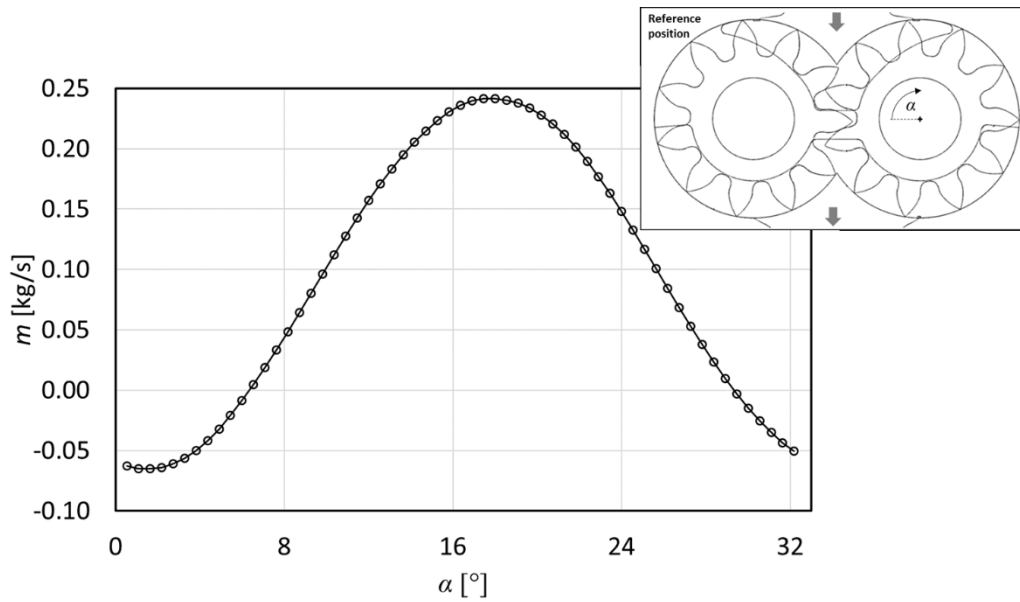


Figure 50: mass flow rate as a function of wheel angular position; on top, the reference angular position is showed

The representation of these leakages is shown in the following Figure 51. On the left-hand side of the picture, it is visible how fluid escapes through the axial gaps, while on the right-hand side the leakages through the tooth-gap are showed. It can be seen that there are two different types of vectors: the ones with the same direction of wheel rotation and the ones directed in the opposite way. The former represents the liquid moving from the suction to the delivery, given by the sealing effect provided by the teeth and, in the numerical simulation, by the no-slip condition imposed for all the wheels surfaces. On the other hand, the vectors directed in the opposite way with respect to wheel rotation depict the fluid escaping the compression chambers and flowing from the high-pressure volumes to the low-pressure ones through the tooth-head gaps.

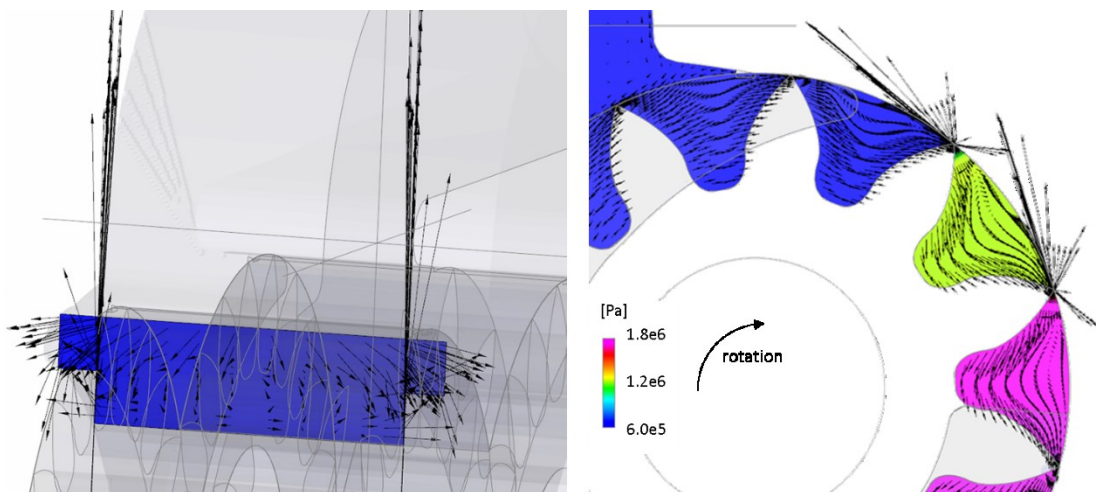


Figure 51: leakages through axial (left) and tooth (right) gaps, represented by means of velocity vectors

Changing the focus from fluid leakages to its pressure pulsations, we have that this phenomenon has been sensed by means of a couple of virtual probes placed in both the suction and discharge ducts of the pump, whose position is depicted in Figure 52. In correspondence of the pump inlet and outlet sections, the rotation of both the gearwheels led to both high turbulence and mixing. At the inlet port, the fluid trapped in the region when engagement occurs determined a certain backflow of liquid towards the inlet. In relation to the angular position of the wheel, the pressure reduction sensed by the probe at the inlet was given by fluid filling the vane which ended the meshing process, leading to an abrupt increment of the available volume for the liquid at the intake of the pump. A similar reasoning can be applied to explain the pressure pulsations at the outlet section; pressure trends at the probe points are depicted in Figure 52, which also shows a pressure plot on a plane perpendicular to gearwheels axes. It is visible how the pressure increment was mainly located on two consecutive vanes in the upper part of the pump, near the intake sections.

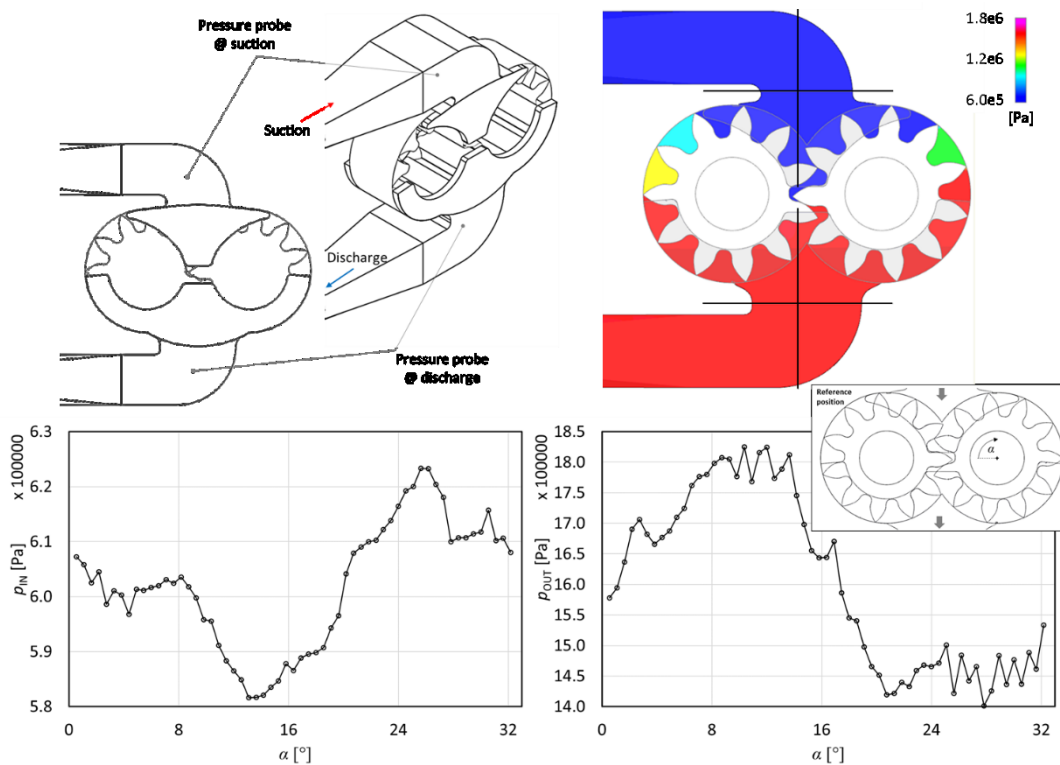


Figure 52: from top-left, clockwise: position of the pressure probes at the inlet and outlet sections; pressure plot on a plane perpendicular to wheels axes, with two black crosses indicating the position of the pressure probes; pressure measured with the exhaust probe as a function of wheel angular position; pressure measured with the intake probe as a function of wheel angular position

From the mass flow rate data depicted in Figure 50 it is visible that, for almost 10 degrees of the considered wheel angular position, a condition of reverse flow affects the simulated system. From this situation, a plot of the pressure on a plane parallel to regenerator outlet axis has been extracted, and it is shown in Figure 53. The upper plot depicts the pressure for

$\alpha=0^\circ$, while the lower one is for $\alpha=16.5^\circ$ which are the angles at which the flow is reversed or it is maximum, respectively. From the $\alpha=0^\circ$ case, it is visible how the pressure generated by the pump is lower than the discharge one, leading to reverse flow in the duct, while in the case of $\alpha=16.5^\circ$ the opposite reasoning can be done, and the refrigerant is successfully supplied to the evaporator.

Another aspect that can be inferred from Figure 53 are the pressure losses given by the presence of fitting and valves, which have been simulated as well. These losses reached a value of almost 2000 Pa, given by the localized pressure drop in correspondence of the valve that separates the duct section belonging to the recuperator and the one belonging to the evaporator.

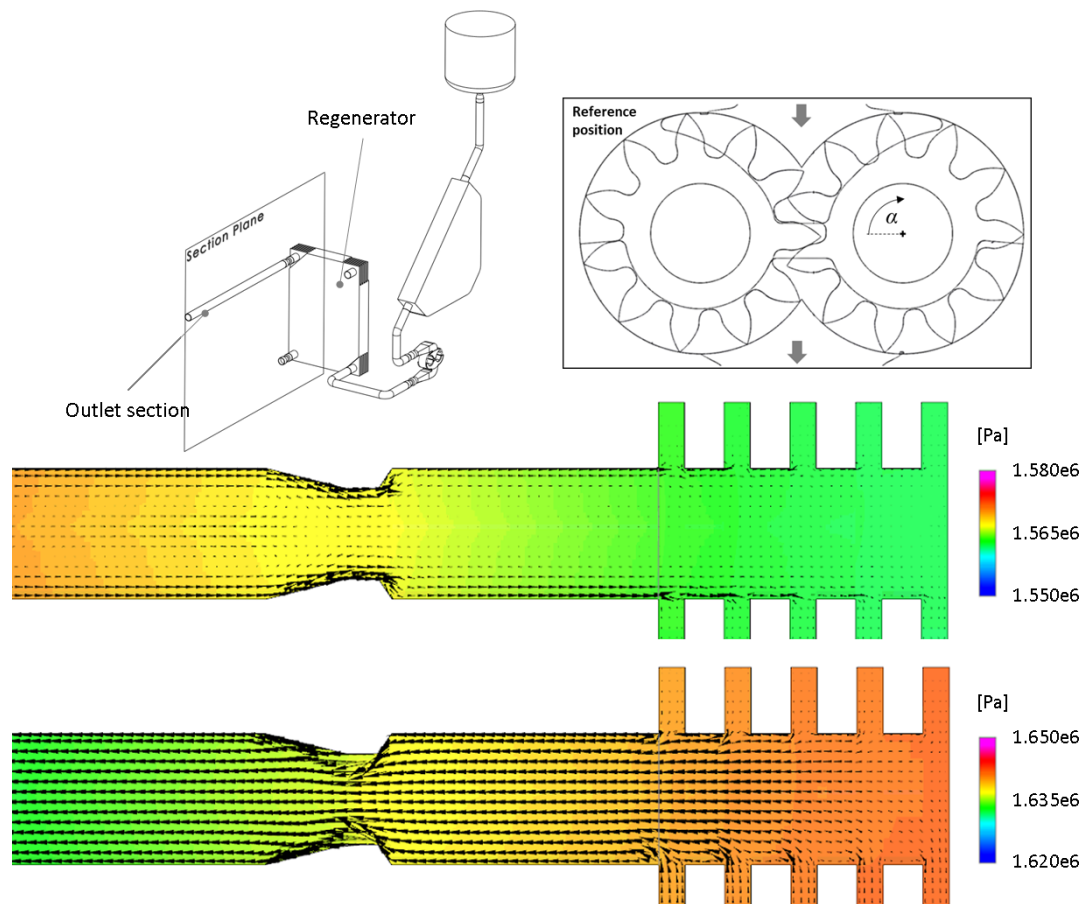


Figure 53: plots of the pressure field and velocity vectors on an axial section of the regenerator outlet duct for the case of $\alpha=0^\circ$ (top) and $\alpha=16.5^\circ$ (bottom) wheel angular positions

3.3.4 Results: System behavior

The pressure pulsation of which the picture above refers influenced also the components placed upstream the pump: this means that also the Coriolis flow meter (CFM) is affected from this phenomenon.

The CFM bases its operations on, as is inferable from the name, the Coriolis force. Each one of these meters includes one or two measuring tubes, which are excited in order to oscillate by means of a dedicated circuit. When the measured fluid begins to enter the measuring tube (or tubes), fluid inertia imposes another oscillatory movement, which superimposes with the one generated by the exciter. A couple of sensors detect the change in oscillation frequency, amplitude and the shift in phase: the latter is directly linked to the fluid mass flow rate. Given the working principle of the CFM, it is clear how fluid pressure pulsations can lead to decreased instrument accuracy, because of inducted oscillations and vibrations not linked to the mass flow itself flowing inside the CFM. Because of this, in the following lines the results of flow pulsations which affected the numerical model of the flow meter will be shown.

One thing that has to be said at this point is that to avoid the detrimental effect of these pulsations on the instrument accuracy, the sensor manufacturer generally indicates, on the operation manual, the proper distance from the other cycle components, especially the pump, usually prescribing to install the CFM upstream this device. Obviously other components such as valves, fittings and curves can reduce the accuracy of the measurement, but the unsteady flow provided by the pump usually has the greatest effect on the accuracy of the measured data.

In the analysis which will be showed below, pressure pulsations deriving from pump operation have been considered as-is, meaning that both the damping effect provided by the system frame and its vibrational response, which is obviously present in the actual test stand, have been neglected. For this reason, the results which will be shown are related to the greatest amplitude of the pulsations in terms of force, calculated thanks to the pressure pulsations signals measured by means of the two numerical probes placed in the positions showed in Figure 54, upstream and downstream the mass flow meter. These probes returned the two pressure traces depicted in Figure 55, where on the left-hand side the pressure at the inlet of the CFM is reported, while on the right-hand side the one at the outlet of this device is showed. As visible from this figure, the Coriolis flow meter is disturbed by pump operation even if it is installed upstream to that volumetric device. By definition, if unbalanced pressures are presents, a net force will exist too: as visible on the left-hand side of Figure 56, a 3 N-magnitude force acting on the housing of the CFM exists, and it is variable with the angle of the toothed wheels, disturbing device measurements.

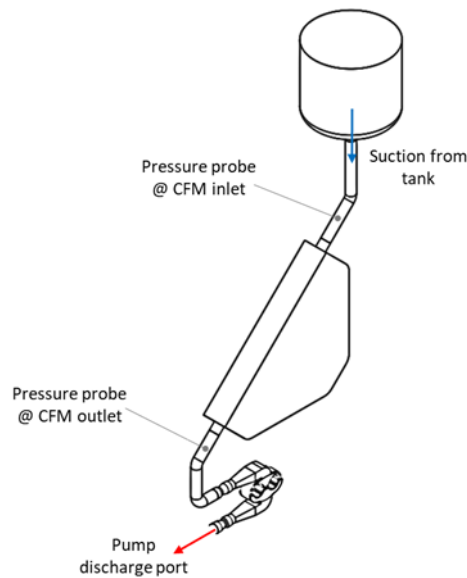


Figure 54: layout of the simulated domain with the positions of the two pressure probes

Moreover, not only the force magnitude can affect the CFM readings, but also the frequency of the pressure pulsations can cause such an issue. For this reason, the Fast Fourier Transformation (FFT) of the force signal already cited has been calculated, and it is shown on the right-hand side of Figure 56. The frequency of each harmonic corresponds to a multiple of the first harmonic, calculated by taking into account the number of teeth of the gearwheel (11) and the rotational velocity for which the analysis was conducted (450 rpm): the interaction between the wheels, the relief groove and the cavitation phenomenon influences the magnitude of each harmonic. Thanks to the FFT, interactions between the pump and the CFM that can be detrimental for the operations of the latter can be detected and, possibly, limited. For example, taking a look at Figure 56, it can be seen that the third harmonic (with a frequency of 247.5 Hz) was greater than the second one (165.0 Hz). This implies that the frequency of the flow disturbance is likely to affect the CFM operation in terms of stability and accuracy for particular operating conditions (depending, for example, on the saturation pressure of the fluid and rotational speed of the pump) [75] [74]. This result confirmed that by running a transient simulation including not only the pumping element but also other components of the circuit, as the CFM, it is possible to find out what kind of interaction takes place, allowing the system user or designer to put in place adequate countermeasures:

- Guarantee a stable operation of the pump, for example by using check valves to reduce backflow;
- Check the resonance frequency of the Coriolis flow meter with respect to the pump operating range, including off-design conditions;

- Try to choose pumps with high capacity, which are able to operate with lower rotational speeds than pumps with limited displacement, in order to limit cavitation phenomenon and the linked high-frequency flow pulsations. Obviously also the design of the pump itself is of great importance to reduce cavitation.

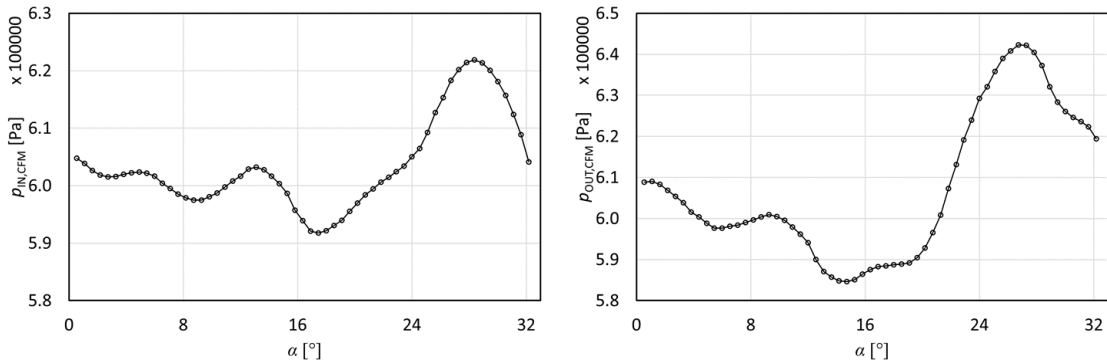


Figure 55: pressure traces at the inlet (left) and at the outlet (right) of the Coriolis flow meter as a function of the wheel angular position

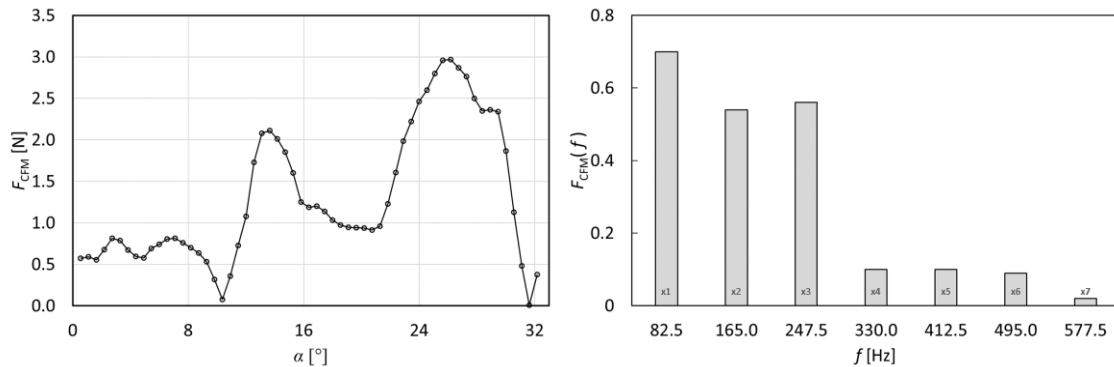


Figure 56: force acting on the CFM as a function of the wheel angular position (left) and its Fast Fourier Transformation (right)

Having introduced cavitation phenomenon, one can think of implementing a control logic which detects this issue and restore the design refrigerant mass flow rate. Any control system has a certain characteristic time, which is given by the sum of the greatest characteristic time between the various measuring devices plus the calculation and data processing time. The actions which are then taken by the control system have to be bounded, not to operate the system in points which are not allowed and have to operate the various components with a certain logic. For example, especially for waste heat recovery applications, a sudden variation of the evaporation temperature could happen: in these cases, a control logic as the one depicted in Figure 57 can be adopted. Referring to this picture, let's suppose that the system is operating in steady-state conditions, with a certain and fixed refrigerant temperature

at the condenser inlet. Suddenly, a steep increase in the heat source temperature takes place: gradually, refrigerant temperature will increase in every section of the system. This will lead to an higher temperature and thus an higher saturation pressure for the fluid at the suction port of the pump, pushing the refrigerant towards cavitation. Clearly, cavitation is not only given by fluid saturation properties but also from the system geometry and pump rotational speed: the latter is the only parameter the system control can manipulate to find a compromise between cavitation issues and the updated thermal conditions. When the vapor bubbles start to collapse, the cycle management system has to increase the pump rotational speed, since cavitation decreases the available mass flow at the outlet of the machine; on the other hand, in this way a greater cooling capacity at the condenser will be required.

In the actual system installed at University of Bologna laboratories [65], the control system generated two different working conditions, a part from the nominal one: these are reported in Table 11; all the other boundary conditions were the same reported in paragraph 3.3.2.4.

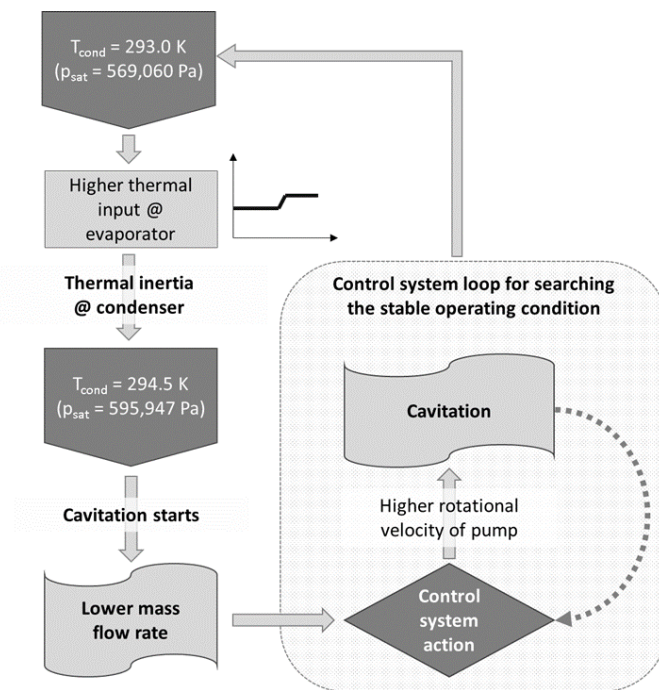


Figure 57: logic diagram for controlling an increase in the temperature of the hot source

In Figure 58, three plots of the gas mass fraction on a section plane transversal to wheels axes are shown: the section on the left-hand side of the figure depicts the situation for the nominal operating conditions, the ones relative to operating point A which have been adopted to obtain the results showed up to this point. The plot reported in the middle of the figure is relative to the operating point B, in which the temperature at the outlet of the condenser has increased but the pump is still operating with the old value of rotational speed.

The last picture, on the right-hand side of Figure 58, shows the gas fraction for the point C in which the system management has increased pump speed reacting to the temperature increment. These plots regarding the released gas mass fraction allow for the simultaneous evaluation of the effects on this parameter given by the presence of both the wheels motion and thermodynamic conditions. From the control system perspective, varying the pump velocity is easier than varying temperatures or pressures of the entire cycle, so the analysis carried out in these paragraph sees the cavitation phenomenon mainly driven by the rotational speed of the two gearwheels. In fact, from the plots representing operating points B and C, it is visible that the gas fraction values for both the rotational speeds are very similar, with the ones relative to point C higher than the ones relative to the unmodified pump speed. This phenomenon is expected to decrease the actual displacement of the pump, leading to a reduction in the delivered mass flow of refrigerant to the recuperator. For this reason, Figure 59 has been here reported.

Table 11: ORC system operating conditions after hot source temperature increase

Operating Point	Liquid Temperature [K]	Saturation Pressure [MPa]	Pump Rotational Speed [rpm]
A	293.0	0.569060	450
B	294.5	0.595947	450
C	294.5	0.595947	475

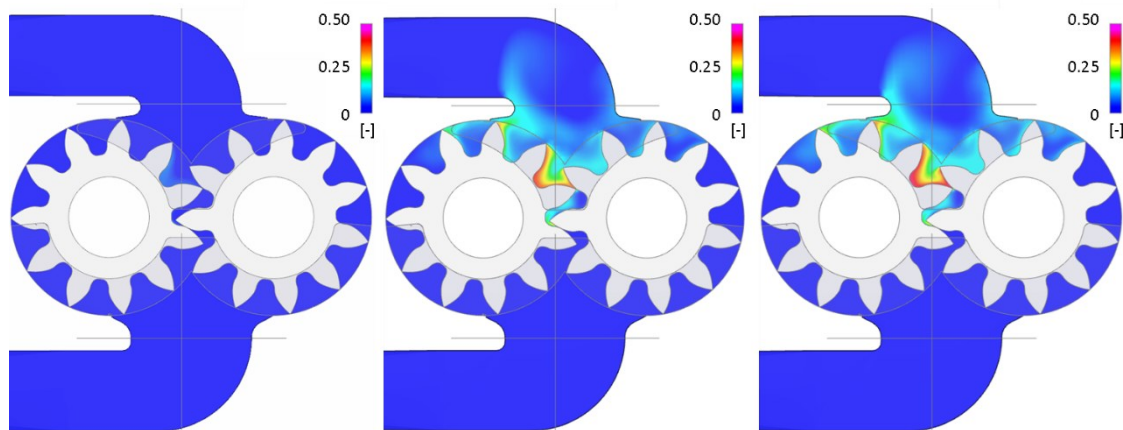


Figure 58: gas mass fraction for working conditions A (left), B (middle) and C (right) as reported in Table 11

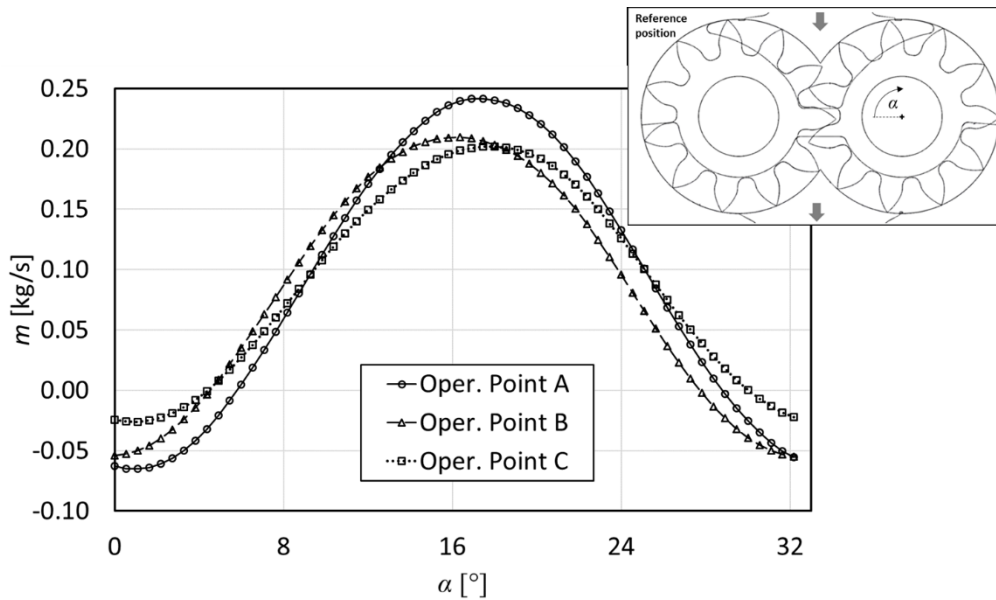


Figure 59: mass flow rate of refrigerant delivered from the pump for the three cases reported in Table 11, as a function of the angular position of the wheels

From Figure 59, it can be seen that both the trend and average value of the mass flow rate varied as the working conditions changed. For the operating point A, the pump delivered 0.091 kg/s of refrigerant. When temperature and thus saturation pressure increased (point B), this value decreased to 0.082 kg/s, which is a value 10 % lower than the nominal one. From this condition, the control system increases the pump speed of 25 rpm (operating point C), restoring the original value for the mass flow rate. On the other hand, even if the value was the same, it was not the case for the trend; furthermore, the greater presence of gas in the mixture reduced flow pulsations thanks to the greater compressibility of the fluid processed by the pump. In spite of these smoother operating conditions, this high gas fraction could generate severe erosion in some parts of the machine, especially near the axial gaps close to the intake port, where the bubbles implode due to the localized increase in pressure.

From the results shown in the pages above it is then clear that numerical simulations of the actual system layout can be of aid to observe how the operating conditions can affect the operations and, on the long run, the operating life of the various components. By using the same simulation method, it is possible to analyze with a similar level of detail how the single devices behave when subjected to a given set of working conditions. This is what will be shown in the next chapter, where results regarding the CFD simulations of an heat exchanger, two different scroll expanders and a single screw machine will be reported.

Analyses of the single components

4.1 Introduction

The study of the single components has been done with a double objective: analyzing their behavior by focusing all the computational resources on a given machine made it possible to create fine computational meshes, being able to quantify phenomena such as leakage mass flow across the gaps of a scroll expander or visualize the amount of lubricant on the surfaces of a single screw expander. On the other hand, by simulating different types of components and machines (namely an evaporator, two scroll expanders and a single screw machine running with or without lubricant) with different computational tools, it has been possible to assess the strengths of each of these software for different applications, aspect which has been taken into account in chapter 5 when choosing the software to be coupled for the Whole ORC Modeling approach.

As it will be shown in the next paragraphs, starting from 4.3, where the results of a simulation of a scroll machine will be presented, lubricant plays a non-negligible role in limiting the volumetric losses of positive displacement machines but is difficult, with standard computational resources, to study also its behavior during the transient simulation of the whole machine. It is then required to make some compromises between the required computational time and the accuracy of the solution, which have to be carefully evaluated on a case-by-case basis.

4.2 Study of the heat exchange inside a simplified evaporator

The first fundamental component being described is the evaporator. From the point of view of a CFD analysis, the greatest difficulty in studying this device is the correct modeling of the phase change which takes place through it, where the liquid refrigerant is heated over its boiling point to obtain saturated or superheated vapor, according to how the expander and the system are designed. In order to understand what are the most suitable models which have to be used when dealing with phase change and with the aim of setting up a simulation which, based on the WOM approach, can be robustly linked to the ones of the neighboring

devices to create an entire virtual cycle, a simple geometry for the heat exchanger has been considered and its simulation has been focused on the distribution of the two phases (liquid and vapor) inside the tube. The generality of the proposed approach makes it possible to extend the results obtained for the evaporation of the working fluid also to its condensation by simply changing the boundary conditions from a value of temperature above the evaporation one to a value below that limit.

4.2.1 Numerical model

The geometry for which the heat transfer has been evaluated is a tube from a fin-and-tube heat exchanger and it is shown in Figure 60. The behavior of the evaporator has been studied thanks to a transient simulations (with a fixed time step of $1e-6$ s) run with Siemens STAR-CCM+[®] CFD tool for a given working point, characterized by an inlet pressure of 1.6 MPa, an inlet temperature of 310 K and a temperature of the heat source of 400 K. To increase the accuracy of the solution while, at the same time, maintaining an acceptable computational time, the so-called “directed mesh” with additional layers of prismatic cells at the boundaries was generated. As reported in the software user’s manual [80], this method generates the computational grid by sweeping a given surface mesh from a source surface to a target surface through the fluid domain; for the exchanger here reported, the source and target surfaces were the inlet and outlet ports of the tube, respectively: the inlet opening has been placed at the bottom of the model, while the outlet one at the top, taking Figure 60 as a reference.



Figure 60: geometry of the heat exchanger. A transversal section is showed on the right

The advantage of this method when compared to the usual ones is that it provides a structured mesh in the axial direction of the component which is, in this case, the direction in which the refrigerant flows, making it a promising way in obtaining an accurate solution throughout the domain (even if it is an hybrid mesh, given the contemporary presence of both polyhedral and prismatic elements). Another advantage of using such a type of mesh is that the total number of elements remain quite low, if compared to the other, unstructured computational

grids which can be generated with the used CFD tool; for the geometry considered here, less than $9e5$ grid elements were generated, comprising both the polyhedral cells at the domain core and eight layers of prismatic cells near the walls at which the heat is exchanged. A couple of sections of the generated mesh are visible in Figure 61.

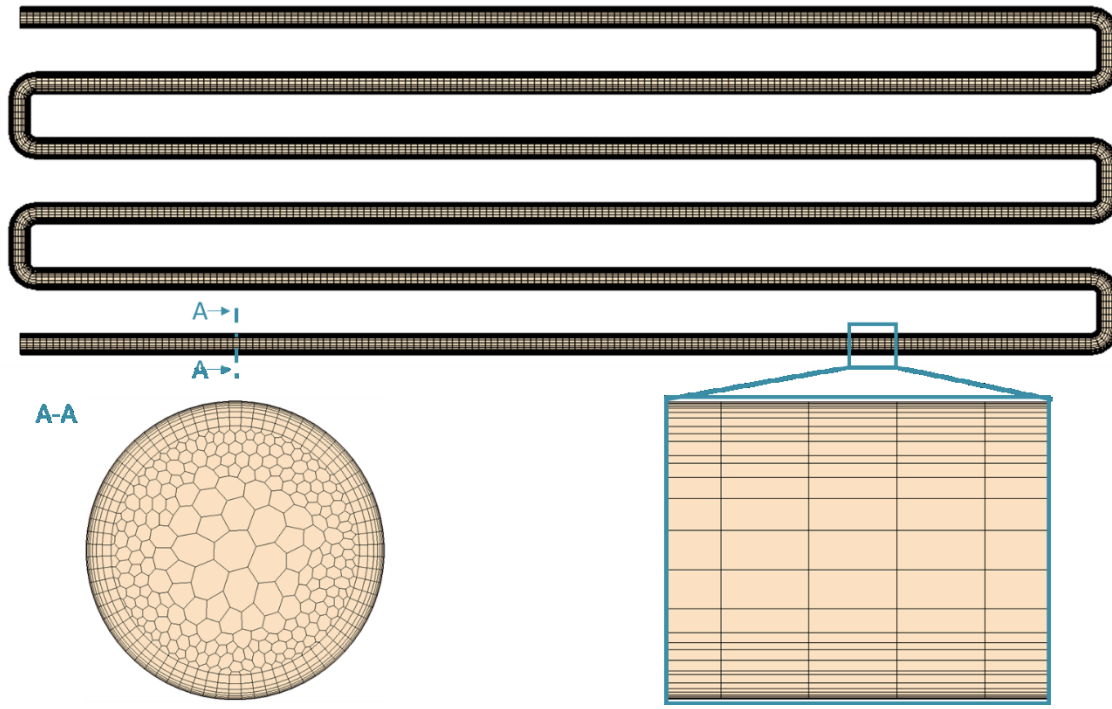


Figure 61: computational grid of the modeled heat exchanger. Global mesh (top), transversal section showing the polyhedral cells at the core and prismatic layers near the walls (bottom – left), magnification of the mesh in the axial direction (bottom – right)

After the mesh was generated, an SST $\kappa\text{-}\omega$ turbulence model with an all- y^+ wall treatment approach was chosen to take into account the behavior of the fluid inside the numerical domain, given the computational grid with fine elements near the walls which allowed to the solution of the viscous sublayer. The phase change of the working fluid, namely R134a, was taken into account with the Eulerian, VOF method, whose characteristics have already been explained in paragraph 3.2.3 when showing the numerical model of the WOM concept. Refrigerant was modeled thanks to the properties reported in Table 12, which are relative to the conditions at the inlet of the evaporator.

Table 12: 1,1,1,2-Tetrafluoroethane (R134a) fluid properties

Property	Liquid	Vapor
Saturation temperature [K]		331
Surface tension [N/m]		0.004
Kinematic viscosity [m ² /s]	1.440e-7	1.629e-7
Density [kg/m ³]	1064	82.50
C _p [J/kg K]	1637	1353
C _v [J/kg K]	963	949
Thermal conductivity [W/m K]	0.067	0.018
Latent heat of vaporization [kJ/kg]		141.929

4.2.2 Results: Liquid mass fraction

The results showed in this paragraph, starting from the one of Figure 62, were obtained after the entire evaporator domain was initialized with a unitary volume fraction of liquid; this means that the various pictures show the real operation of the evaporator when the cycle is started, having run transient simulations. Taking a look at Figure 62, it is possible to make a couple of remarks: the first is that, after one second of physical time, the average volume fraction of gas at the outlet of the evaporator is nearly 60 %; the second is that, on the rest of the domain walls, this fraction is much more variable, with liquid spots surrounded by vapor.

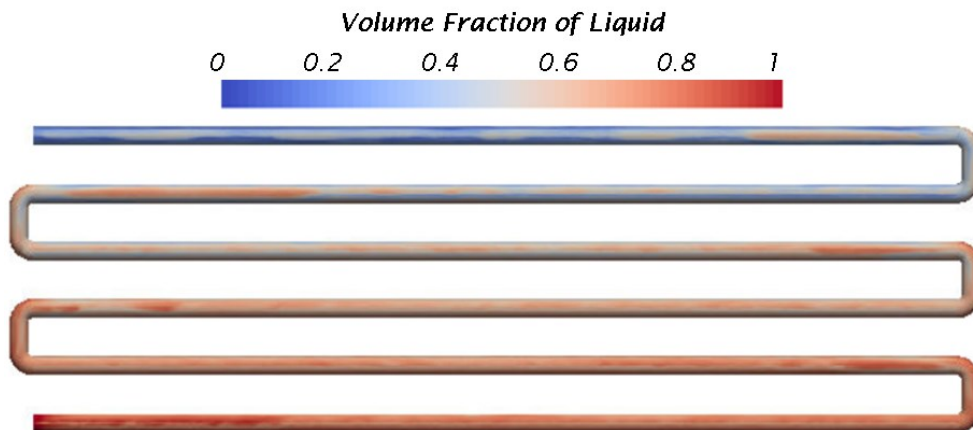


Figure 62: liquid volume fraction on the walls of the exchanger after 1.0 second

When running the simulation to calculate other 0.5 seconds of evaporator operation, it is possible to see from Figure 63 how the volume fraction of liquid on the walls near the outlet opening is almost zero; this means that the startup of this device under actual operating conditions is extremely rapid, reducing the expander by-pass time at the startup of the cycle: the by-pass is required to avoid liquid entering the expansion machine during this phase, by

recirculating the fluid between the pump, the recuperator (if installed), the evaporator and the condenser.

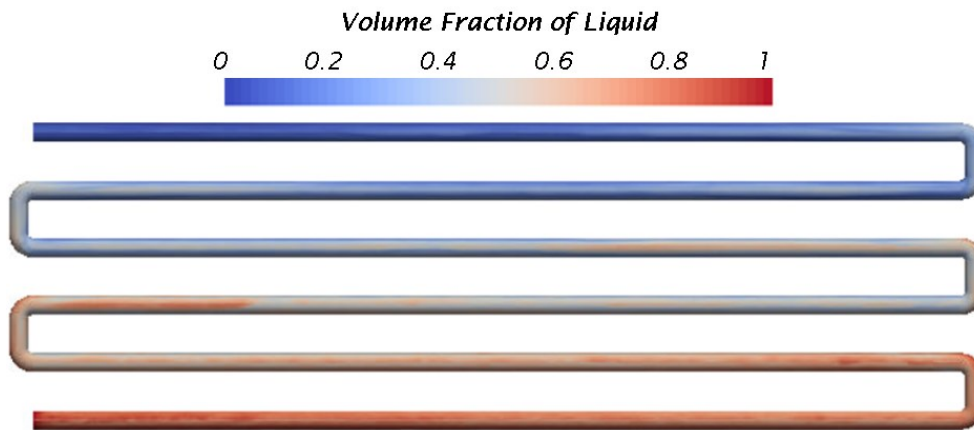


Figure 63: liquid volume fraction on the walls of the exchanger after 1.5 seconds

When moving the focus from the distribution of liquid on the walls to the one in the internal volume of the pipe, another interesting aspect can be found, which was hidden by the presence of the domain boundaries. From Figure 64, it is noticeable how the distribution of the two phases is less scattered, if compared to Figure 63 and how liquid stratification takes place on the lower part of each tube; this fact is also confirmed by observing Figure 65, where a transversal section of a tube is reported: on the walls and on the bottom of the pipe, the volume fraction of liquid is greater than in the middle of the duct, showing how the correct modeling of all the phenomena involved in this transformation led to plausible and useful information for the fluid properties at the outlet of the device. It is then clear how, from this type of simulation, both the response time of the heat exchanger when the system is turned on or boundary conditions (such as refrigerant flow, wall temperature or heat flux) vary and its behavior in terms of phases distribution inside the exchanger can be investigated. Thinking at the impact on the WOM approach, this means that all the fundamental information about fluid state at the outlet of the heat exchangers can be exported to the next component of the cycle (pump or evaporator, downstream the condenser or evaporator respectively), as already suggested in paragraph 3.1. Obviously, it is then necessary to enable the phase-change models also on these downstream devices, with effects which can be detrimental on the robustness and rapidity of the solution. So, sometimes it is necessary to adopt some simplification, such as neglecting the two-phase flow being admitted in the machine. Given this, while reading the next two paragraphs it has to be taken into account that, while the study reported in paragraph 4.3 refers to an oil-free device, the one in 4.4 is

relative to a lubricated machine whose oil presence has not been modeled for those two reasons.

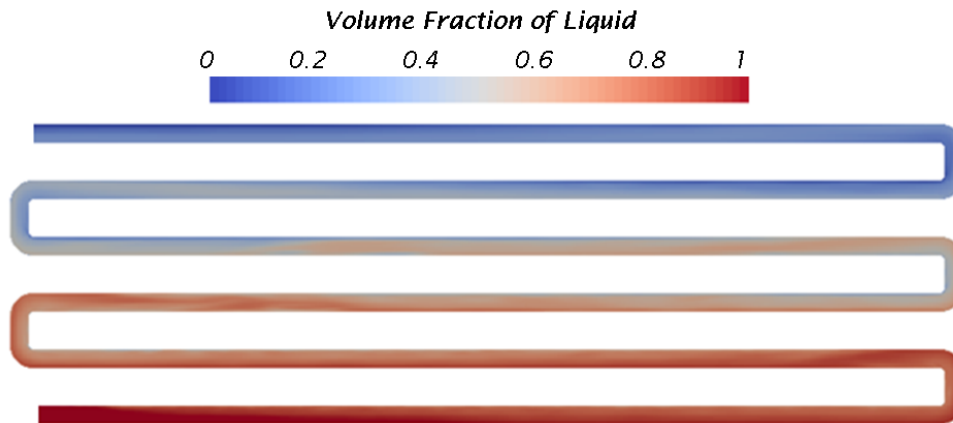


Figure 64: liquid volume fraction inside the exchanger after 1.5 seconds

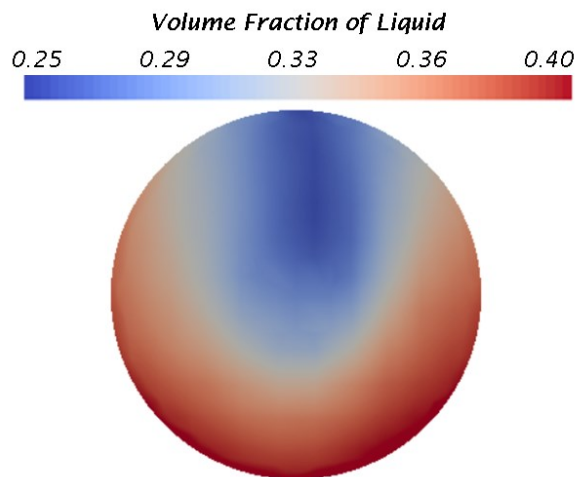


Figure 65: liquid volume fraction on the outlet section of the exchanger after 1.5 seconds

4.3 Analysis of an oil-free scroll expander

In the following lines, the procedure shown at the 4th International Seminar on ORC Power Systems [81] aimed at the characterization of an oil-free scroll machine will be presented. The important aspect of this study is given by the fact that the expansion machine was derived from a compressor, thus no information about its behavior when operating in compression mode was known; first of all, the machine was tested under the new operating conditions on an air-running test stand; then, for being able to study the performances of the expander for different working conditions (such as refrigerant in place of air), a Reverse Engineering (RE) procedure has been adopted to obtain the CAD model necessary to run CFD simulations. The numerical model was then validated against the experimental findings.

4.3.1 Test stand

The scroll compressor (see Table 13 for its main geometric characteristics) was installed on the test stand depicted in Figure 66 and was operated as an expander, thus the inlet and outlet ports connections were inverted. The test bench was equipped with several sensors, such as temperature probes, pressure transducers, a thermal type flow meter, a load cell and a rotational speed sensor, in order to fully characterize the scroll operation. The temperature probes were A-class, Pt100 devices and were installed to measure the air temperature at both the inlet and outlet ports of the machine, alongside with the thin-film pressure transducers, with a full-scale of 16 bar and a ± 0.5 % Full Scale accuracy. Temperature and pressure sensors were placed 1.5 m before the scroll inlet port and downstream the plenum used to damp pressure fluctuations at the outlet of the machine. The flow meter was installed upstream the inlet pressure sensor and was characterized by a 180 m³/h FS with a ± 1.8 % FS accuracy. To measure the torque at the shaft of the moving scroll, a load cell with 10 kg FS and ± 0.05 % FS accuracy was installed between the expander outlet and the electrodynamic brake. The last sensor, the rotational speed one, was based on the Hall effect and showed a resolution of one sample per scroll shaft resolution. The data coming from all these sensors were acquired by means of a Data Acquisition device (DAQ) with an accuracy of ± 1 K for temperature measurements and ± 1 % of the reading for the other current signals. The A/B-type uncertainty of 2.5 % of reading was estimated to take into account all those contributions which were not known, a priori (such as flow conditions, installation, etc.).

Table 13: oil-free compressor characteristics

Property	Value
Nominal power [kW]	5
Volume ratio [-]	3.5
Displacement [cm ³ /rev]	73
Maximum rotational speed [rpm]	2600
Flank gaps width [μ m]	20-300

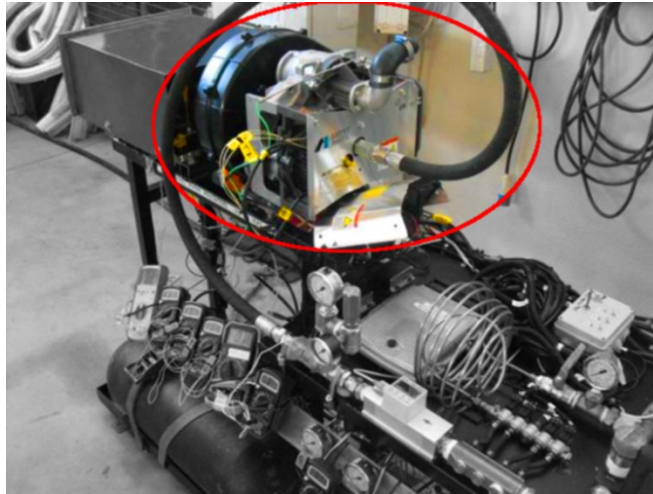


Figure 66: scroll machine (red circle) installed on the test stand

4.3.2 Numerical model

The main peculiarity of scroll machine operation is given by the orbiting motion of the moving spiral: as reported in paragraph 1.4.2.2, since each point of this component does not follow a circular path but one in which the points translates around a circular trajectory, the flank clearances width is not constant during rotation, but it varies as a function of the angular position of the shaft (see, for example, the schematic representation on the left-hand side of Figure 68). For this reason, it is not possible to model this motion through a “standard” moving-boundary CFD simulation, since we are not in front of a pure rotation. So, the CFD analysis has been conducted by using the overset mesh approach, implemented in the 11.02 release of Siemens STAR-CCM+[®] tool. The fluid model of the machine is showed in Figure 67.

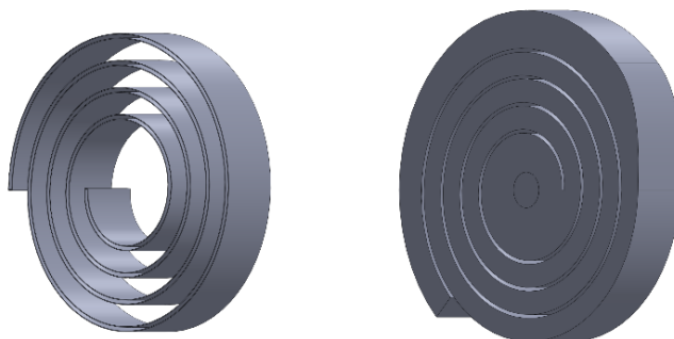


Figure 67: fluid model of the scroll expander; moving spiral (left) and stator (right)

The overset mesh criterion is based on two type of numerical grids: a background mesh and one or more overset meshes attached to the moving bodies, overlapping the overset mesh but also each other, when it is required. Both these meshes uses active and passive cells to discretize the movement of the boundaries; in active cells, the conservation equations are

solved while in passive cells, since they are temporarily or permanently deactivated no solution is searched. Since these equations are solved on all grids simultaneously, to link the results obtained in the overset regions with the one found in the background grid acceptor and donor cells are used: the former represents the first layer of passive grid elements near the active ones and exchange data with the latter, which are active cells which belong to the other mesh; every cell in the domain can be both donor or acceptor, it depends on the motion of the boundaries, thus the change of cell status is controlled by the solver via an interpolation function which can be selected by the software user. Overset mesh method differs from the ones which use cell morphing to adapt the domain to the boundary motion since the moving grids are not deformed during their movement, thus mesh quality during the simulation remains constant. On the right-hand side of Figure 68 it is visible a representation of the overlapping grids, while in Figure 69 the next a detail on how overset meshes were applied to the studied geometry is depicted. For the simulations carried out in this analysis, the overset mesh bounded the moving spiral geometry and was obtained by a 1 mm-offset from the actual spiral boundaries; this moving mesh consisted in almost seven millions of elements, while the background mesh (which included both the scroll housing and fixed spiral) was made up by about twelve million elements. Both the two meshes consisted in polyhedral elements at the core with prism layers close to the boundary walls, as visible in the right-hand side snapshot of Figure 69.

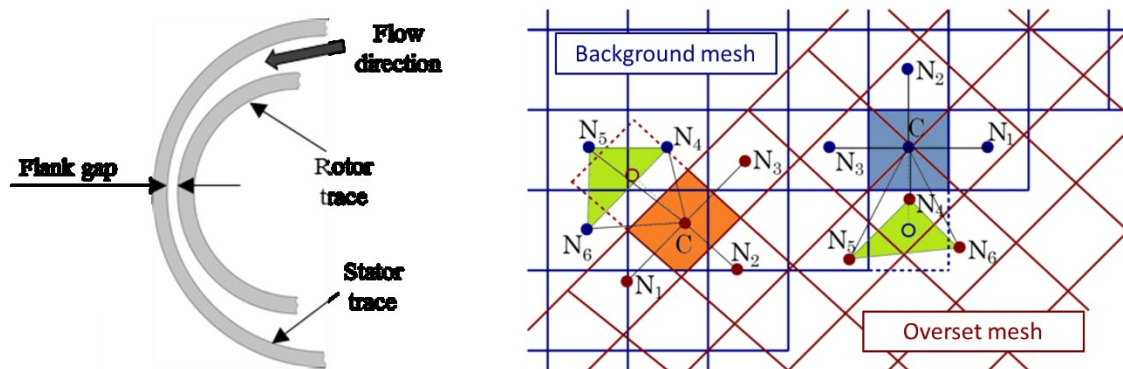


Figure 68: sketch of a flank gap (left) and representation of background and overset grids, from [80] (right)

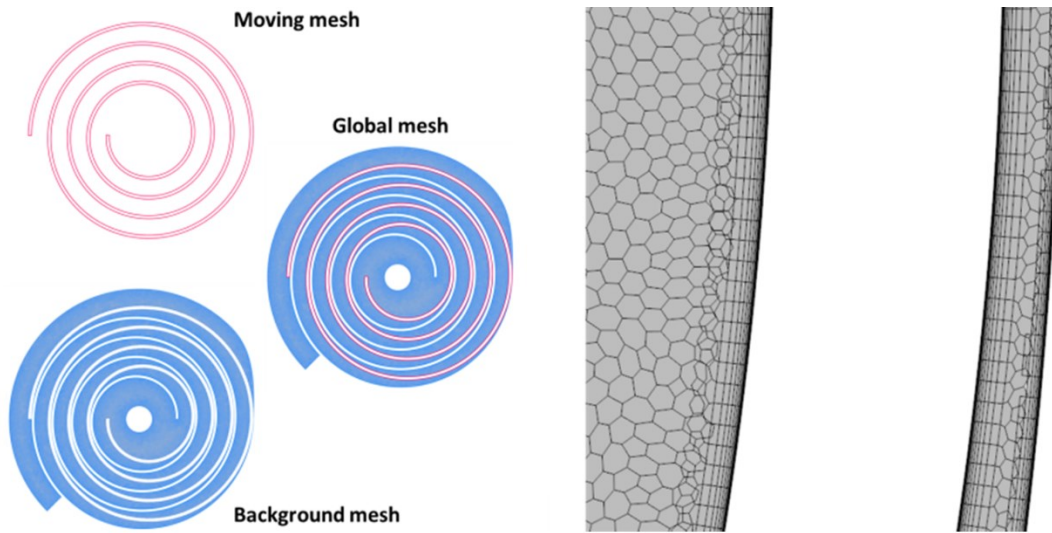


Figure 69: representation of the fluid domain by means of overset mesh method (left) and detail of the mesh in narrow gaps (right)

When simulating the scroll expander, the same inlet and outlet pressures and temperatures encountered in the experimental tests were used; a stagnation inlet boundary condition was imposed at the admission port of the machine with a static pressure of 0.75 MPa and a temperature of 292 K, while at the exhaust port of the machine a pressure of 0.101325 MPa was set. Since no temperature measurements for the housing of the expander were available, the domain walls were considered adiabatic, while the overset mesh surface enclosing the moving spiral was set as an overset mesh boundary, in order to define its interaction with the stationary parts of the domain. The validation with the experimental values was carried out for six different rotating speeds: 400 rpm, 800 rpm, 1200 rpm, 1600 rpm, 2000 rpm and 2400 rpm.

When considering turbulence modelling, the realizable $k-\varepsilon$ model was used alongside the two-layer y^+ wall treatment in order to model the air flowing through the clearances with a greater accuracy than the one provided by the standard $k-\varepsilon$ model because it is predicted to give more accurate results for flows which involve rotation and strong streamline curvature [82]. The two-layer y^+ wall treatment was adopted because of different values of the y^+ which were encountered in the first cell inside the flank gap and the ones on the other boundaries, having checked that no y^+ values were in the buffer region. The Redlich – Kwong equation of state was used to model the working fluid as a real gas.

The combined effect of both the hybrid mesh approach (polyhedral elements and prismatic cells) adopted to generate the computational grids for the simulations ran for this analysis and the presence of stretched elements could reduce the stability of the solution [83]: for these reasons, great care was taken to choose the most appropriate time step for each

simulation. Each CFD analysis was carried out with a temporal discretization spanning from 1e-5 s to 5e-6 s, depending on the scroll rotational speed and has been initialized with a solution obtained with a first order Upwind advection scheme before switching to the second order one.

4.3.3 Results: CFD-calculations of pressure and velocity fields

The behavior of the machine in terms of pressure distribution in the various expansion chambers is showed in Figure 70, where pressure values are plotted on planes perpendicular to the expander rotational axis for two different speeds, 2400 rpm and 800 rpm. While the pressure pattern is clearly similar for the two rotational speeds, for the former under-expansion is greater, because of the lower fluid residence time inside the expansion chambers, which led to a more limited pressure work at the moving boundary of the spiral.

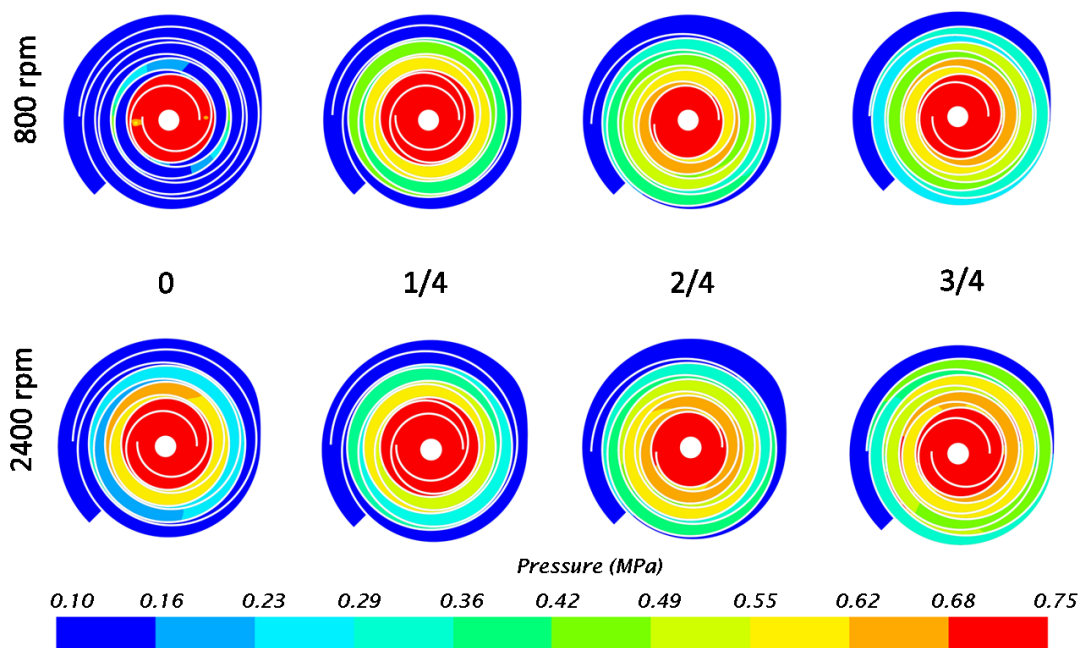


Figure 70: pressure plotted on planes perpendicular to expander rotational axis for two different values of rotational speed

In Figure 71, velocity magnitude plots on the same planes of the previous picture are reported. It can be seen how high values of velocity are always present both in the flank gaps, and this was an expected result since the simulated machine runs oil-free, and in the outlet duct: velocity, in this part of the domain, is not constant but it depends on the rotational speed of the moving spiral. Furthermore, at the duct shoulder (Figure 72) it is visible how a recirculation zone is always present during the expander operation. This is given by the steep increase in the cross-sectional area of the duct in this zone and, since from the plots of Figure 71 is visible how its extension varies during the movement of the spiral, it is supposed to

influence the flow being exhausted from the machine. To analyze this aspect, the volumetric flow at the outlet of the machine has been calculated and plotted in Figure 73: machine operation is characterized by flow pulsations which can also cause the working fluid to reverse its path and enter the machine from the exhaust. It is useful at this point of the analysis to check if this phenomenon causes a lower volume flow rate at the outlet of the machine; to do so, the numerically determined average values for this parameter have been compared against experimental data. Results are given in Figure 74: from the graph on the left hand side of the picture, it is visible how the results obtained by means of the CFD studies are always greater than the actual ones: this happened because the flank gaps of the numerical model were wider than the ones of the actual machine, because of the use of the overset mesh approach to model the movement of the spiral: smaller values for the width of the gaps would have lead the hole-cutting method to fail. On the other hand, still focusing on the left-hand side of this figure, it is recognizable how the two trends are almost parallel, apart from the 1200 rpm data. It was then thought to present this comparison in a dimensionless form, obtained by dividing each of the numerical and experimental results by their peak value: this is shown on the right-hand side of Figure 74. It is then clear how the current simulations were able to capture the general behavior of the scroll expander, even if the gaps of enlarged with played a significant role in altering the results.

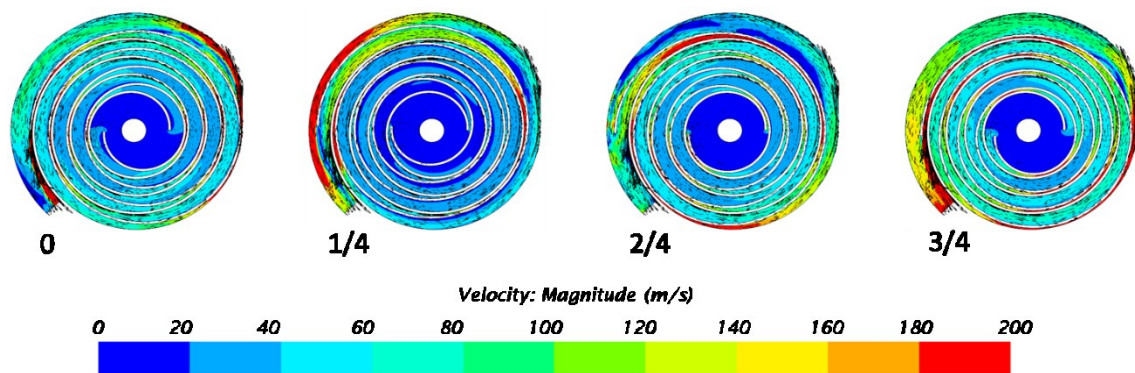


Figure 71: velocity magnitude plots on planes perpendicular to expander rotational axis

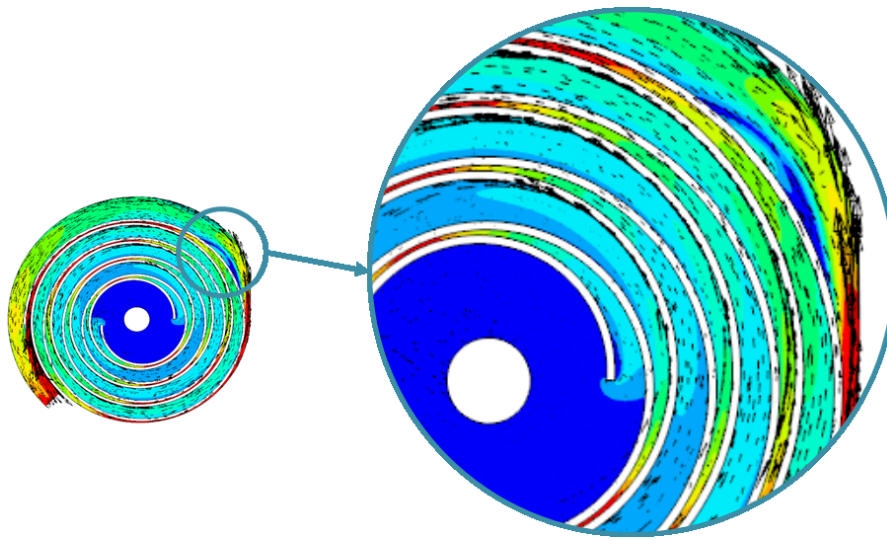


Figure 72: magnification of the recirculation zone

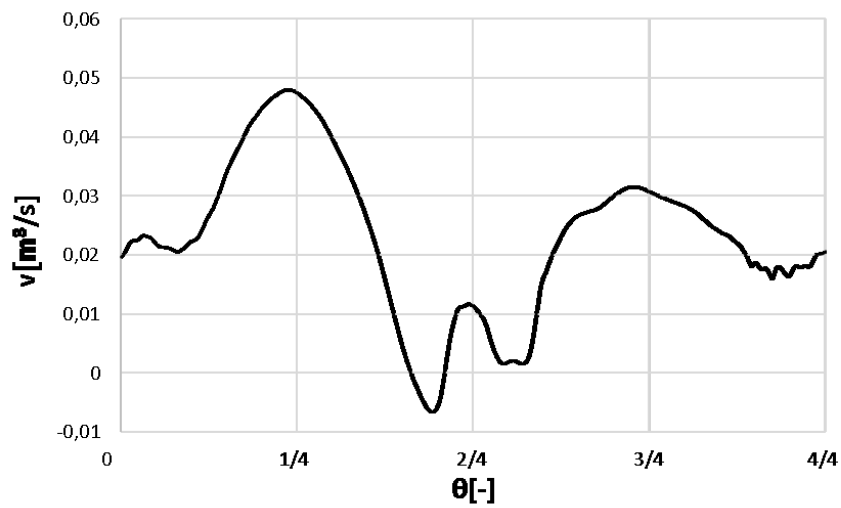


Figure 73: volumetric flow as a function of the normalized angular position

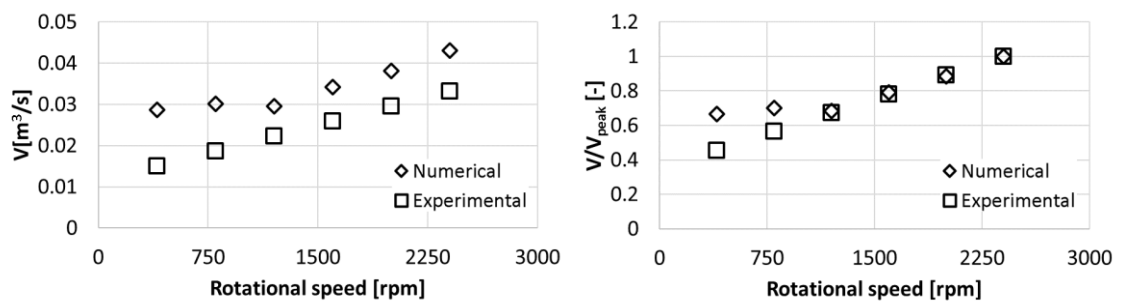


Figure 74: average values of the volumetric flow rate at the outlet of the machine. Actual values (left) and dimensionless ones (right)

4.4 Analysis of an Oldham-ring scroll expander

For the case showed in paragraph 4.3, no information about the anti-rotation mechanism of the moving spiral has been given, because the Oldham ring was placed in a position which did not influence the internal fluid-dynamics of the machine. On the other hand, there are cases in which this mechanism is placed in a location which can influence the flow, as the one which will be described here, where the outlet port is always partially occluded because of its presence and, during machine operation, the ring moves in front of the exhaust port. To study its influence on the flow field, transient simulations have been run, with an innovative approach which included the modeling of the motion of both the moving spiral and the Oldham ring. The machine which has been analyzed is a scroll expander similar to the one whose performances have been assessed in paragraph 2, being produced by the same company. The results showed below are adapted from the work presented at the 5th International Seminar on ORC Power Systems [84].

4.4.1 Numerical model

To prepare the CAD (Computer-aided design) model provided by the company for the analysis, all the couplings such as screws and bolts were removed, together with gaskets and their seats. The resulting geometry is shown in Figure 75. On the left-hand side of the figure, a section perpendicular to moving spiral rotational axis allows the reader to observe both the rotor and the Oldham ring, while on the right-hand side a global view of the machine is presented, with the inlet and outlet ports: through the latter, it is possible to see the Oldham ring, which clearly occupies a portion of the discharge area. This is visible in greater detail in Figure 76, where a section passing from the outlet port axis and rotational axis is showed. No modification has been done to the width of both radial and axial gaps, which was equals to 50 μm for both of them. After geometry simplification, the CAD model was imported into the simulation tool; at first, the same software used for the case depicted in paragraph 4.3 was intended to be used, but the number of mesh elements required to model the motion of both the translating spiral and the Oldham ring with the overset mesh approach was prohibitive, given the available computational resources. This fact meant that no simulation could have been run up to convergence in a reasonable time. To overcome this issue, the machine has been simulated with CONVERGE, from Convergent Science because of its ability in simulating moving boundaries requiring a computational effort lower than the one requested by the software used in paragraph 4.3. With this software, a cartesian grid is generated and, to model motion, the cells are gradually cut using the given geometry of the moving boundaries; to take into account the narrow gaps which exist between the flanks of

the spirals and between them and the housing, the Adaptive Mesh Refinement (AMR) algorithm has been used. This method automatically refines the computational grid only in those volumes of the domain in which the gradient of a certain flow variable, e.g. velocity magnitude, pressure or temperature is greater of a user-defined value. For a domain which varies with time as the one showed here, this means that by having imposed a certain condition on the velocity gradients, areas including the radial and axial gaps have been refined. Another aspect of the AMR method which has to be explained is the condition which controls the coarsening of the mesh when the criterion on the gradients of the variable is no more met: the software releases the refined cells when the value of the variable in them is below one fifth of the user-defined one. An additional feature of CONVERGE is that elements are coarsened or refined during runtime, reducing the set-up time of the simulation with respect to the already cited software: in that case, the user has to manually refine the computational grid during the pre-processing phase also in those zones in which the overset and background meshes overlap. For the case reported in these lines, where the overset approach should have been used also to model the Oldham ring (not present in the simulation of paragraph 4.3), this would have meant additional computational resources for the processing phase, as well as more time during the pre-processing one.

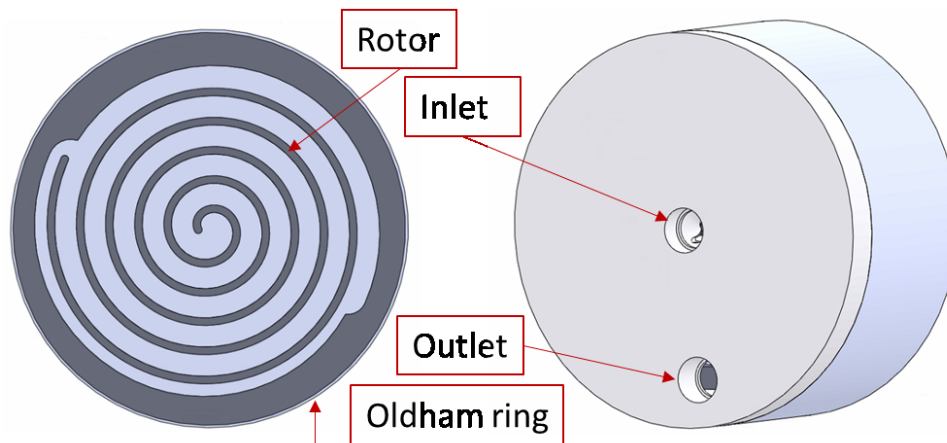


Figure 75: defeatured geometry

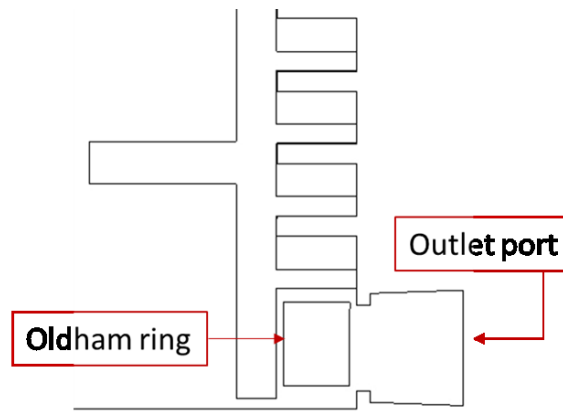


Figure 76: section showing the position of the Oldham ring

Once the scroll domain was meshed, the numerical model has been set up as follows: an INFLOW boundary conditions was placed at the inlet of the machine, while at the outlet an OUTFLOW condition has been imposed. About the thermal specification of the various surfaces composing the numerical domain, all of them were set as adiabatic. The rotational velocity of the scroll shaft derived from the frequency of the North American electrical grid (60 Hz), and the translation velocity of both the moving spiral and the Oldham ring have been set up accordingly by means of a user-defined function. Turbulence was modeled with the RNG κ - ε model; regarding the wall treatment, a y^+ approach with standard wall functions was utilized, since dimensions of the grid elements, even the ones refined thanks to the AMR method, have been chosen not to resolve the viscous sublayer. In doing so, the base size of the cartesian grid was imposed equal to 1 mm in each of the three dimensions; this led to a number of elements between one million and three millions, since the AMR algorithm was able to increase or decrease the number of mesh elements up to five millions, based on a condition on the gradient of velocity magnitude. The mesh generated in an certain instant of time and intersected by a plane perpendicular to rotational axis is visible in Figure 77, where it can also be noted where the refined areas given by the adoption of the AMR approach are located. The second order Monotonic Upstream-Centered Scheme for Conservation Laws (MUSCL) has been used for spatial discretization of the convective term of transport equations.

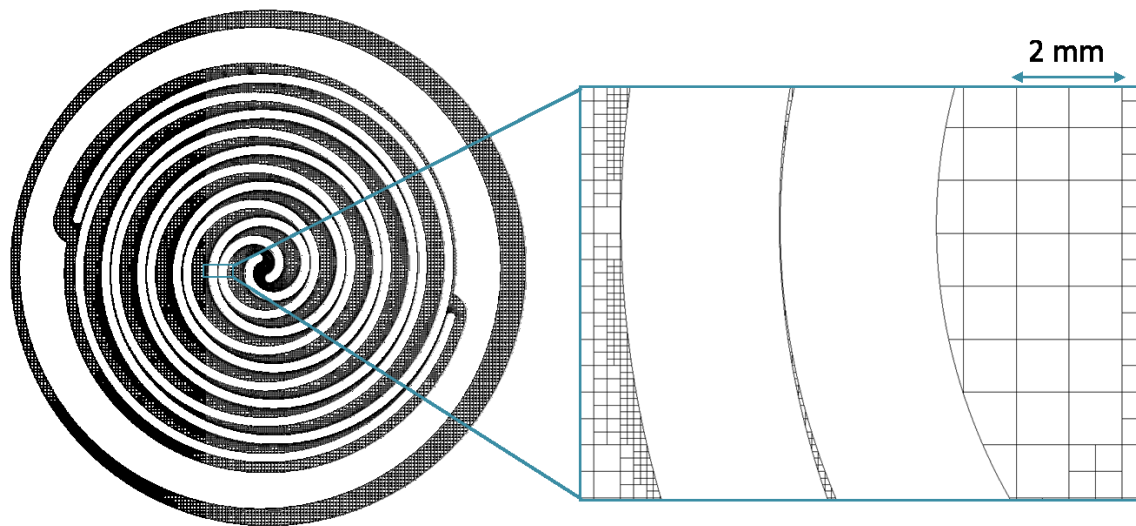


Figure 77: mesh on a section perpendicular to moving spiral orbiting axis, for a given instant

Simulations were run using air at first and then 1,1,1,3,3-Pentafluoropropane (R245fa) as working fluid: air was initially adopted just to test the simulation set-up, before passing to the real gas modeling of the refrigerant, where its properties (e.g. density, specific heat, specific enthalpy, and so on) were determined by interpolating values reported in a look-up table obtained by querying the open-source CoolProp library [52], with the simulation tool being able to read the extracted values.

Regarding the temporal discretization, the time-step has been set-up as variable as a function of both the Courant-Friederichs-Levy (CFL) number and the moving surface characteristics, but it has been bounded between 10^{-8} s and 10^{-5} s. The maximum acceptable value of the CFL number has been imposed to 2.0, which has been considered a good compromise between both simulation robustness and time. When focusing on the time-step limitation given by the moving boundaries characteristics the software takes into account, for each of them, cell size and speed, as well as the value of an user-defined multiplier which, in this analysis, has been set to 0.5.

All the properties defined in the lines above, together with a couple of geometric characteristics useful for the results which will be showed, are reported in Table 14.

Table 14: boundary conditions and geometric characteristics

Property	Value	Property	Value
Inlet pressure [MPa]	2.4	Inlet temperature [K]	523.15
Outlet pressure [MPa]	0.25	Outlet temperature [K]	440.15
Rotational speed [rpm]	3600	Gaps width [μm]	50
Suction volume [m^3]	4.56e-6	Nominal mass flow rate [kg/s]	0.0275

4.4.2 Results: Mass flow

To analyze the behavior of the expander for the given working conditions, the mass flow rate, the pressure variations within the chambers and the velocity profiles within the gaps have been studied. In Figure 78, the mass flow rate which is sucked and exhausted by the machine during fifteen revolutions of the moving spiral is shown, giving an idea of the variability of this parameter during steady machine operation. By calculating the FF with equation (2), it results a value of 2.58. This is lower than the value obtained when using air as working fluid (4.39), but it is still higher than the one obtained experimentally from the manufacturer of the expander, which is 1.22. This happens because the increase in fluid density at the inlet port is almost totally compensated by the increase in mass flow rate. This behavior can be explained as follows: in the real machine, a 5 % by mass of Polyolester (POE) oil is added to the refrigerant, sealing the gaps. Since in this analysis the oil has not been modeled, this phenomenon has not been taken into account, leading to the result shown above. Trying to quantify these leakages, one can consider the expression for the FF, equation (2): the theoretical mass flow at the inlet of the expander is the denominator of that equations, which is equal to 0.0225 kg/s. In the case here reported, the computed mass flow rate is 0.0580 kg/s thus the leakages, which are the difference between design value and actual one, are equal to 0.0355 kg/s. It is clear that such a value is not representative of the actual mass flowing into the domain, but it has something to do with the adopted modeling. To better check this result, a steady simulation with the same value for the axial gaps (50 μm) and the same minimum value for the radial gaps of the transient one has been run; also the values of the other not time-related quantities (thus thermal specification of the boundaries, conditions of the fluid at the inlet and outlet of the machine and so on) have not been varied. The mesh of the steady simulation was cartesian as well, with a total number of elements around three millions; it is straightforward that the AMR was not applied, since the mesh was stationary. To overcome this, the radial and axial gaps were discretized not only by means of the main, cartesian mesh but also with six layers of prismatic cells. It has been possible to implement this type of elements by using STAR-CCM+® as the simulation tool. A detail of the grid in radial and axial gaps is showed in Figure 79.

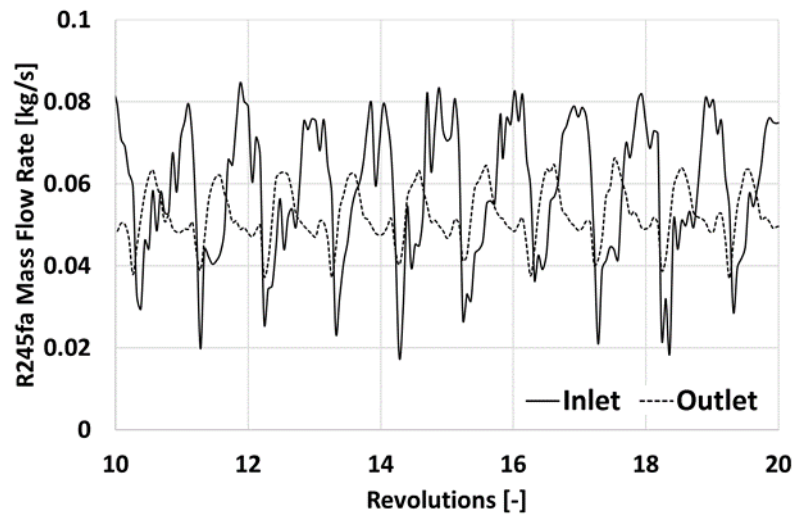


Figure 78: R245fa mass flow rate at the inlet (solid line) and outlet (dashed line) of the machine

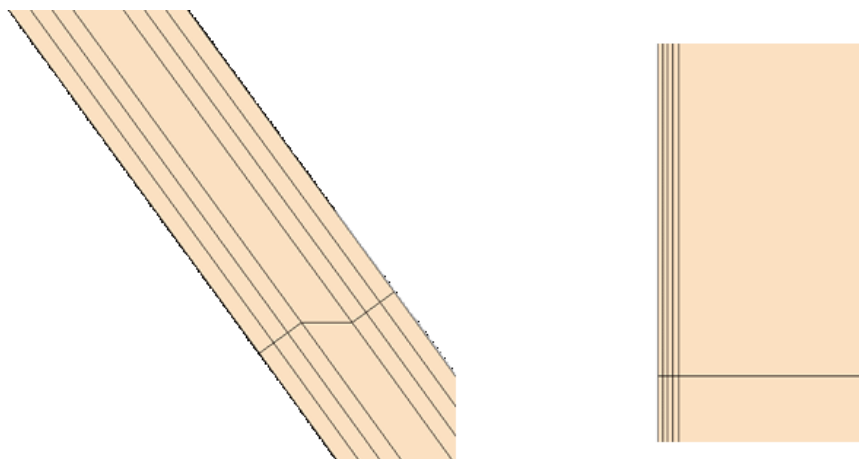


Figure 79: detail of the mesh in radial (left) and axial gaps (right). Magnification of the right-hand side picture is lower to show the relative dimensions of the prism layers with respect to the base grid

With this approach, it has been possible to calculate the leakage flow by simply subtracting the value of the mass flow rate at the outlet from the one at the inlet, obtaining a datum of 0.0338 kg/s. This value is just a couple of grams below the one obtained from the transient simulation (0.0355 kg/s), thus it can be thought that such exaggerated values for leakages mass flow rates, even higher than the nominal one through the entire machine, are not only given by discretization errors but from the absence of oil modeling. Another possible explanation for this discrepancy between mass flow rates data could be given by the fact that, in the real expander, gaskets fitted in both the moving and fixed spirals limit refrigerant flow across axial gaps, while in the simulations carried out in this study this components have been omitted, as already stated at the beginning of paragraph 4.4.1. A way to quantify both the phenomena of “oil sealing” and “gasket sealing” is to run simulations with fictitious, reduced values for the width of the gaps: for this reason a computation with radial gaps

shrunk to 30 μm , from the actual value of 50 μm , has been run, resulting in a decrease of the computed mass flow rate through the machine, which reached 0.046 kg/s. Even if this datum is 60 % higher than the nominal one, the trend indicates that this approach can be useful, beside the other possibility of modeling lubricant. The main issue in doing so is the growing computational effort, since conservation equations for oil mass, momentum and energy have to be solved, in addition to the ones linked to refrigerant. One can try to reduce this effort by adopting the Volume of Fluid (VOF) method, in which the total mass, momentum and energy equations are solved, together with the void fraction equation which represents the fraction of cell volume which does not contain liquid. Anyway, even in this case where just a set of equations has to be solved, to avoid excessive modeling error given by numerical diffusion a fine mesh is required, to track with a good accuracy the interface between the oil liquid phase and the refrigerant vapor phase, thus the resources required for the simulation remains to be higher than an approach based on the progressive reduction of the width of the gaps of the machine. Since the aim of the actual study is to quantify the leakages, and not the oil distribution in the expander, the approach of reducing the gaps by modifying the CAD model is expected to reduce the workload if compared to the lubricant modeling approach.

4.4.3 Results: Pressure and velocity fields

In this paragraph, a few comments regarding pressure of the refrigerant inside the machine and its values at the inlet and outlet ports will be made, before embarking on the explanation of how the Oldham ring influenced fluid flow at the exhaust of the expander.

In Figure 80, the pressure traces at the suction and discharge section of the machine are shown: after six revolutions of the moving spiral, pressure values stabilized around the nominal one (2.4 MPa at the inlet and 0.25 MPa at the outlet). It is possible to see that pressure pulsations at the inlet are below 1 % of the nominal value at this port, while at the outlet are below 2 %, with the global behavior affected by numerous pressure spikes. A possible explanation for these is that the ones at the inlet are related to the moment in which the suction pocket reaches its minimum value, while the ones at the outlet are probably given by the Oldham ring starting to reduce the flow passage area in front of the exhaust port.

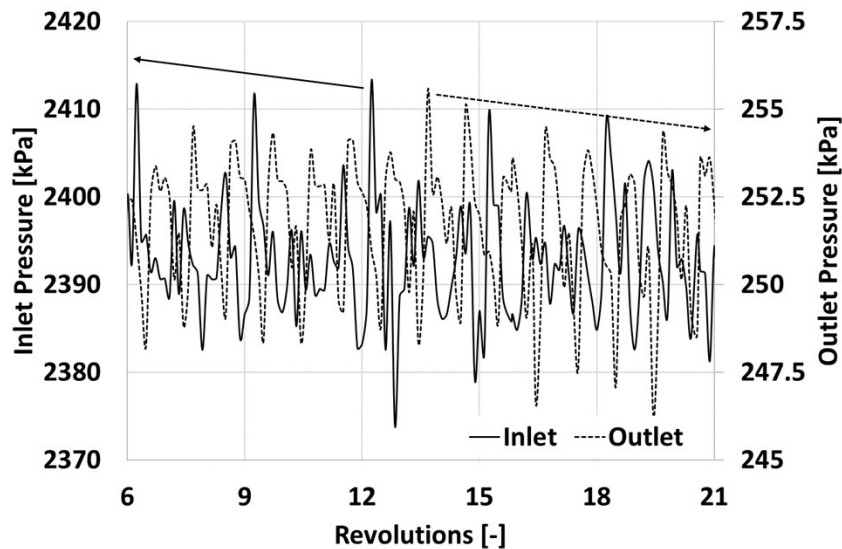


Figure 80: pressure traces at the inlet (solid line) and at the outlet (dashed line) ports

Another useful piece of information is the pressure trace during expansion, which is useful to check the pressure decrease through the expander, from the inlet to the outlet. In Figure 81, the two light blue lines represent the inlet and outlet pressures. To build this graph, data has been gathered through eleven different monitor points, whose location is depicted in green in the section overlapped on the graph. First of all, it seems that no over- or under-expansion losses were present, since the last three blue points seem perfectly overlapped to the discharge line. Under expansion losses occurred, actually, but their entity was well below 5 % of the nominal value (265 vs 250 kPa). At the suction of the machine some losses occur as well, around 20 kPa. Analyzing the rest of the graph, one can see that the greatest part of the expansion process takes place in one revolution, where pressure decreases from around 2300 kPa to 1300 kPa and then the rest is much more gradual up to the discharge value.

In Figure 82, the plot depicting the dynamic variation of pressure on a plane perpendicular to the moving spiral rotational axis during machine operation is reported. This figure is another way to represent data depicted in Figure 81, in fact it is possible to see the steep decrease in pressure for the chambers near the inlet port.

The last result shown in the next lines is related to the evolution of the velocity field during expansion. One of the objectives of this study was to investigate the effects of the Oldham ring on the refrigerant flow being exhausted from the machine. To do so, a plot showing the axial component of the velocity at the outlet section is showed in Figure 83. It is possible to see that attached to the ring and to the walls of the outlet port, zones with positive value of axial velocity exist. This means that in these zones fluid is not going out from the machine thus, since the velocity magnitude is zero, these are stagnation zones. This phenomenon can

be explained by the fact that, during Oldham ring motion, this component constantly occludes part of the outlet port thus, when the ring starts moving to the upper position, the fluid previously entrapped behind this component is able to flow towards a lower pressure region. Because of the shape of the ring and of its motion, flow is pushed upward and thus recirculates [84].

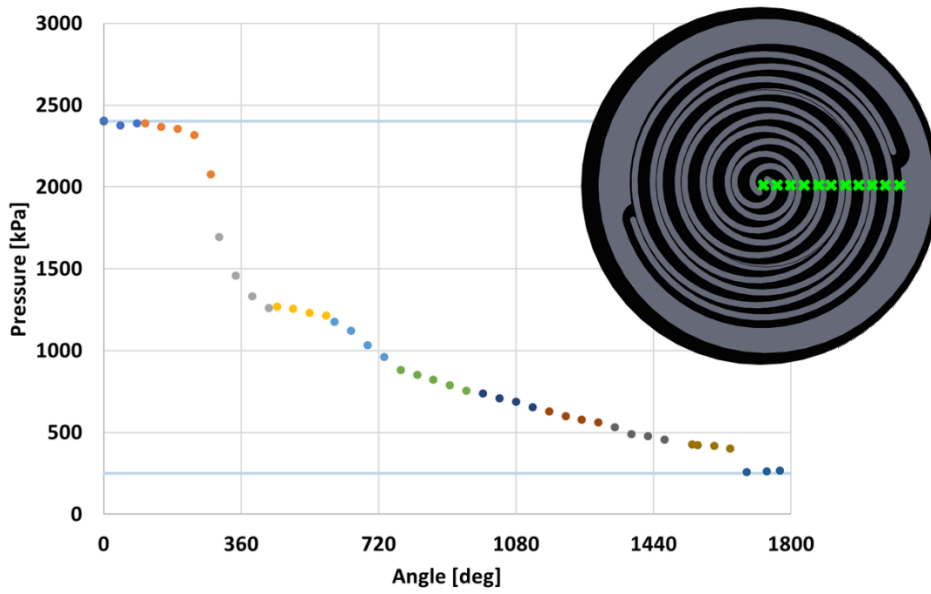


Figure 81: pressure inside the expander during its operation

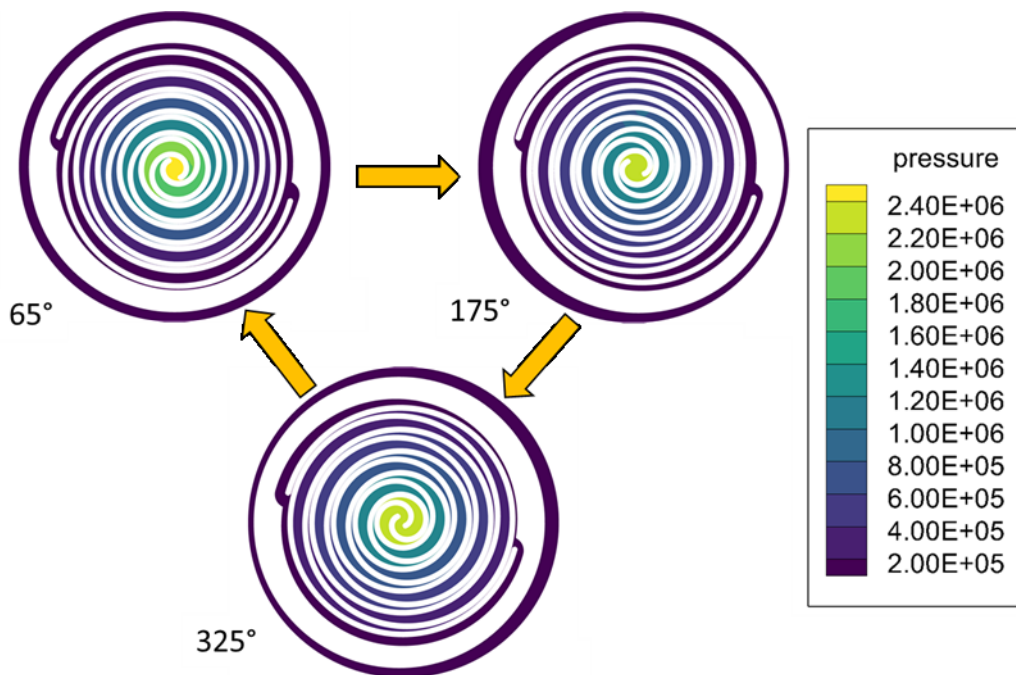


Figure 82: static pressure during one revolution of the scroll shaft, values are in [Pa]

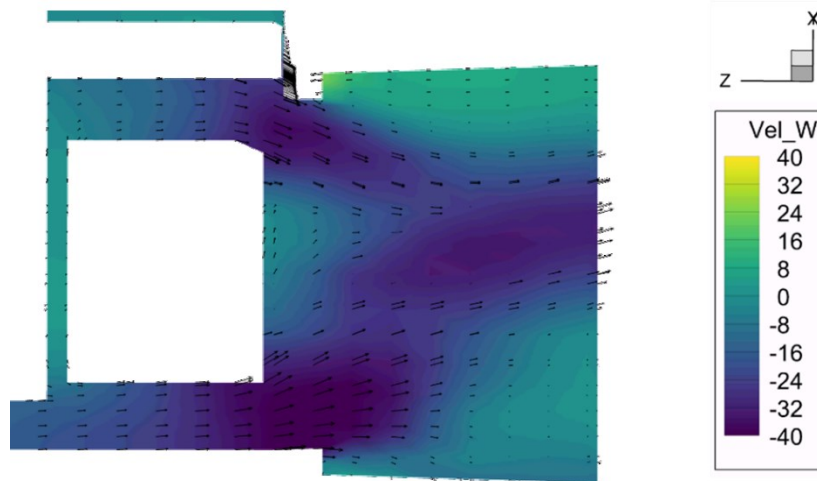


Figure 83: axial component of the velocity at the outlet of the machines, values are in [m/s]

4.5 Analysis of a lubricated single screw expander

For the two expanders analyzed in the paragraph above it has been remarked that lubricant was not modeled, in the first case because the machine was effectively an oil-free device, while for the example reported in paragraph 4.4 the presence of oil was neglected because of the additional computational resources required to run a multiphase simulation. Since it is expected that oil leads to an increase in volumetric efficiency of positive displacement machines by sealing their gaps, it would be interesting to study how the operation of such machines is affected by the presence of this liquid also by the point of view of its distribution on their surfaces, in terms of oil thickness and analysis of those locations in which it can stagnate. In the study presented at the 2018 International Conference on Screw Machines [85], from which the results shown in this paragraph are taken, it was written that many studies about screw expanders have been done with the obvious objective of increasing the thermodynamic efficiency of the whole ORC system. A couple of very interesting ones is represented by the works of De Paepe et al. [86] and Ziviani et al. [87] in which the first showed that oil atomization in screw machines permits to cool down the devices but it does not sensibly increase its global performance, while in the second isentropic efficiency values greater than 70 % are supposed of being reached by halving leakages and friction losses, thus by using lubricant. The fact is that very few works have been applied to expanders only, and even less are relative to single-screw machines: for example both the study reported in [86] and the one of the first ever made about computational analysis of oil-flooding effects on single-screw machine operation [88] considered compressors. Nevertheless, some findings can be extended to machines working as expanders: for instance, Hotta et al. [89] and Minami et al. [90] found that to guarantee reliable operation during entire machine

lifetime, a key aspect is to maintain a lubricant layer with constant height on the meshing parts, avoiding its breakage.

It is then clear that the use of oil can be of aid to extend expander lifetime, but this is true only if the correct lubricant is chosen, taking into account the type of working fluid and the working conditions for which the ORC system has to operate. When dealing with hydrochlorofluorocarbons (HFCs), which are the most employed refrigerants in micro-ORC systems, ester-based oils are normally used [91]. On the other hand, if the type of refrigerant and operating conditions influence the choice of the oil, the type of lubricant influences the properties of the working fluid to which is mixed: Zhelezny et al. [92] studied the dependency of density, vapor pressure, surface tension and capillary constant of R245fa-polyolester compressor oil mixture for various lubricant concentrations. This is a remarkable work, since oil properties are usually available for a limited range of temperatures, with mixture properties far harder to find.

With this in mind, in the next lines the results of a 3D, CFD test campaign on an oil-injected single-screw expander model will be showed. An experimental characterization of the expander has been done by Ziviani et al. in 2017 [87], thus data regarding temperature, pressure and mass flow rate of the working fluid at both inlet and outlet ports of the machine are known. As reported in [85], the first results which will be shown regard the analysis of the droplets paths and oil film evolution inside the inlet distributor, varying the droplets diameter while maintaining the same refrigerant and lubricant mass flow rate. Then, the outcome of an analysis in which a particular configuration of the screw occluded the two inlet ports of the machine will be presented; in this condition, the mass flow at the outlet of the machine is only given by the fluid leakages through the gaps between the screw, the housing and the starwheels, leading to a different behavior for the oil droplets with respect to the previous case.

4.5.1 Numerical model

The machine used as the model was an 11-kWe air compressor which Ziviani et al. [93] adapted to work as an expander for a micro-ORC system. Figure 84 reports two photos of the actual machine (on the left-hand side) and two representations of the 3D, CAD model, of the same machine (right-hand side). The main rotor (screw) has six grooves, while the starwheels have eleven teeth. To reduce fluid leakages in the meshing region, a low-friction material is added to the teeth of the starwheels, reducing clearances during the engagement process.

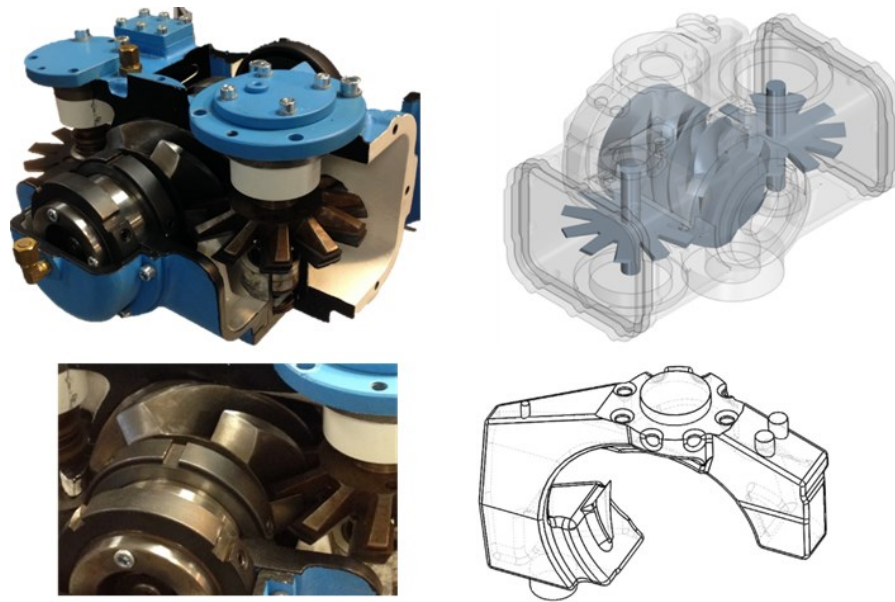


Figure 84: single screw expander. From top-left, clockwise: real-world geometry; 3D-CAD model; detail of the meshing region; CAD model of the admission duct

As already done for the other CFD studies reported in this thesis, the actual layout of the machine as depicted in [93] has been thoroughly simplified, since the representation of most of the geometric particulars was beyond the scope of the numerical analysis: from the actual geometry depicted in Figure 85, all the bearings, screw and starwheels shafts were simplified, as well as the gaskets; on the other hand, the housing has not been changed, in order to accurately predict the flow behavior from the main intake port of the machine to the screw through the admission duct, which was characterized by a curved shape: two branches end with two triangular suction ports, which have been designed to fill the screw rotor grooves in a proper way. One of the machine features which have not been simplified were the clearances: according to Ziviani et al. [94], the gaps between the main rotor (screw) and the housing are in the range between $30\ \mu\text{m}$ and $60\ \mu\text{m}$, while the ones between the main rotor and the starwheels lie between $20\ \mu\text{m}$ and $60\ \mu\text{m}$. From the top-right picture of Figure 84 are also visible the two starwheels meshing with the screw, while from the fluid model, Figure 85, the machine inlet port is recognizable, being highlighted in violet. The geometric characteristics of the expander are reported in Table 15.

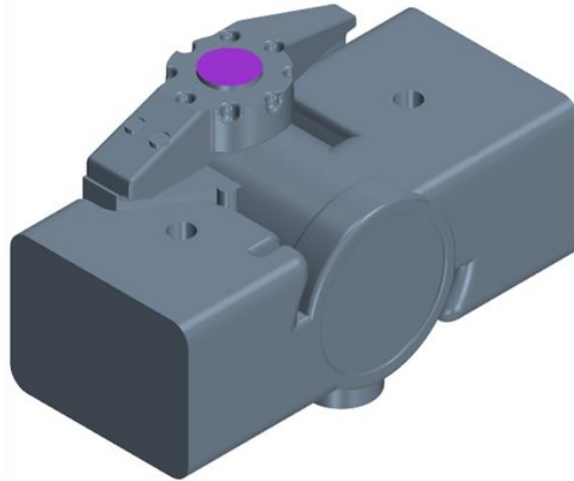


Figure 85: fluid model of the single-screw expander

Table 15: single screw expander geometric characteristics (from [34])

Property	Value
Engaging ratio [-]	11/6
Screw diameter [mm]	122
Starwheel diameter [mm]	132
Displacement [cm ³]	57.39
Built-in volume ratio [-]	5.3
Screw length [mm]	121

The present analysis has been conducted by injecting oil in through the main inlet port of the machine, the one violet-colored in Figure 85. For this reason, the two injectors already present in the expander geometry have not been used. Instead, a cone injector has been placed coaxially to the inlet in order to uniformly spread lubricant parcels in the gas flow. Following gas path, the mixture between refrigerant and oil sweeps the inlet duct up to the two admission ports depicted in Figure 86, where it is finally injected in the expansion chamber. As visible from this figure, the two ports are not symmetrical with respect to the screw, leading to a different behavior for both the oil droplets and fluid film thickness in the two branches of the duct: according to the reported geometry, the gas path up to the lower port is characterized by a couple more narrow bends than the one to the upper port.

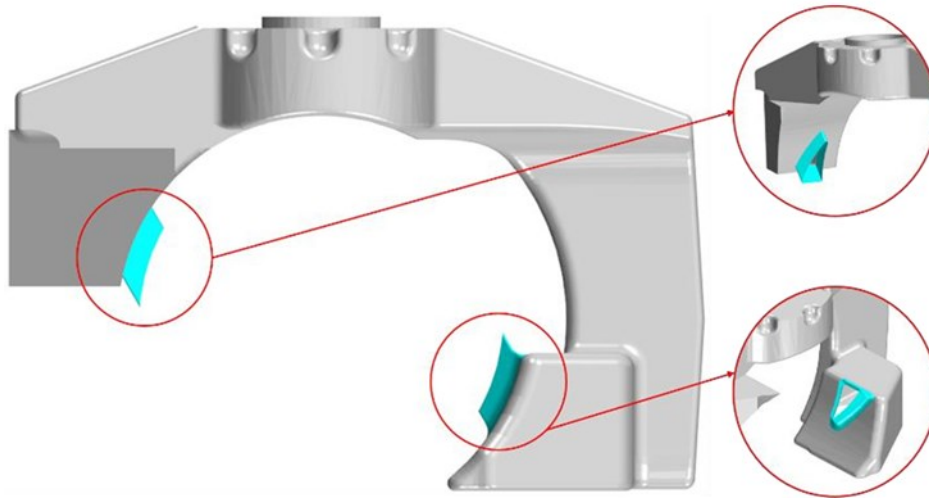


Figure 86: view of the inlet duct with the upper and lower inlet ports highlighted (cyan)

After the geometry simplification, the CAD model has been imported in the simulation software used to run the CFD simulations, namely STAR-CCM+[®]. The capability of this software in dealing with the moving parts of a single-screw machine will be shown in next paragraph, but while in the present analyses no rotation of the various starwheels and screw rotor have been modeled, the presence of dispersed liquid phase (oil) in a bulk flow of gas (refrigerant) poses another modeling challenge. To deal with this fact, the working fluid has been modeled as a real gas using the Redlich-Kwong equation of state. To track the oil droplets from the injection point up to the expansion chamber, the Eulerian approach (for the gas) has been coupled with the Lagrangian one (for the liquid): since liquid droplets were expected to form a film over certain expander surfaces, both the fluid film and impingement models were enabled, together with the one which took into account the oil stripping from some surfaces to other, based on face concavity.

The Redlich-Kwong equation of state models gas behavior by modifying the ideal gas law by introducing two coefficients a and b which are both function of the gas pressure and temperature at its critical point. The choice of modeling the refrigerant with a real-gas law was given by the fact that the physical conditions of R245fa at the inlet of the machine led to a compressibility factor Z equals to 0.83, indicating the unsuitableness of the ideal gas approach (which would have been appropriate if one had checked just the compressibility value at the outlet, which was $Z=1.01$). The real-gas flow of refrigerant receives the oil droplets modeled with the Lagrangian approach, which allows to track every single particle highlighting its behavior in terms of temperature, velocity, dimensions and so on. Since solving a set of conservation equations for each droplet would have been too expensive under the point of view of the allocated computational resources, the CFD tool adopted a statistical

method in which all the droplets are grouped in clusters, which are a collection of droplets sharing the same properties. To take into account the exchange of energy and momentum between the parcels and the refrigerant bulk flow, the two-way coupling model has been used, not to consider just the exchange of these quantities from the gas flow to the liquid droplets. The impingement model has been used to model the behavior of parcels when they hit the domain surfaces; in the case of a wet boundary, the liquid particle transfers its mass, momentum and kinetic energy to the oily surface. This could happen for both the droplets being dragged by the R245fa flow and the ones which drip on the underlying surfaces from boundaries characterized by a sharp edge. For this reason, to measure the growth of the lubricant film on the surfaces, it has been necessary to adopt also the fluid-film model implemented in the CFD tool. This model solves a set of conservation equations for mass, momentum and energy, together with the computation of the volume of liquid in each cell of the numerical grid. The result of these computations are the pressure, temperature, distribution and thickness of the fluid film. As introduced a few lines above, for the case presented in this paragraph the fluid film increases because of the parcels impinging the surfaces and decreases because of stripping from the surfaces. Film stripping is modeled thanks to a couple of numerical approaches: the liquid film break-up criterion derives from Friedrich et al. [95], while the diameter of the liquid droplets which derives from the liquid stripping is taken from Maroteaux et al. [96]. Liquid separates from the from a certain edge when the ratio of the inertial force to the gravitational force and surface tension is greater than one; this ratio also affects the number of liquid droplets ejected from the bulk flow when their velocity is the same as the fluid film one. The conjugate heat transfer between oil film, oil droplets and gas flow has been considered, while the heat transfer to the walls of the domain has been neglected, having these boundaries being modeled as adiabatic.

The values for the properties of the refrigerant and the boundary conditions are reported in Table 16. The transient simulation was set up with a time-step equals to $5e-7$ s which is linked to a unity value for the Courant number. Turbulence was modeled thanks to the Menter's [97] two-equations, shear-stress transport (SST) κ - ω model.

Table 16: model properties and boundary conditions

Property	Value	Property	Value
Refrigerant inlet temperature [K]	398.05	Lubricant droplets diameter [μm]	0.5 – 40
Refrigerant dynamic viscosity [Pa s]	1.3723e-5	Lubricant inlet velocity [m/s]	4
Refrigerant specific heat [J/kg K]	1102.3	Injector cone angle [rad]	2
Refrigerant thermal conductivity [W/m K]	0.021519	Injector streams [-]	7
Lubricant inlet temperature [K]	340	Engaging ratio [-]	11/6

As already mentioned, two different numerical analyses have been carried out. The first one was dedicated to the investigation of the oil droplets trajectories inside the inlet distributor and their bond with oil film distribution and thickness. The CAD model of Figure 86 was discretized with nearly half million hexahedral elements whose dimensions spanned from 0.5 mm to 2 mm, as showed in Figure 87. When considering the second type of analysis, which regarded the interaction between the screw rotor and the suction ports, the domain was still discretized with hexahedral elements, but with dimensions included in the range from 0.01 mm to 2 mm; the smallest dimensions of the elements accounted for the presence of the gaps between screw, starwheels and the housing, as reported in [94]. Because of this, the total number of elements reached the value of two millions, giving the mesh shown in Figure 88. Both the grids shown in the two pictures below have been chosen after the results of two different sensitivity analyses. For both cases, the combination between the flow characteristics and the grid elements dimensions led to y^+ values in the range 0.5 – 100: for this reason, an all- y^+ approach has been selected, solving the viscous sub-layer for the y^+ values below one and using wall functions for values outside the transition zone, zone which has been carefully avoided by checking y^+ values at the end of the simulations.

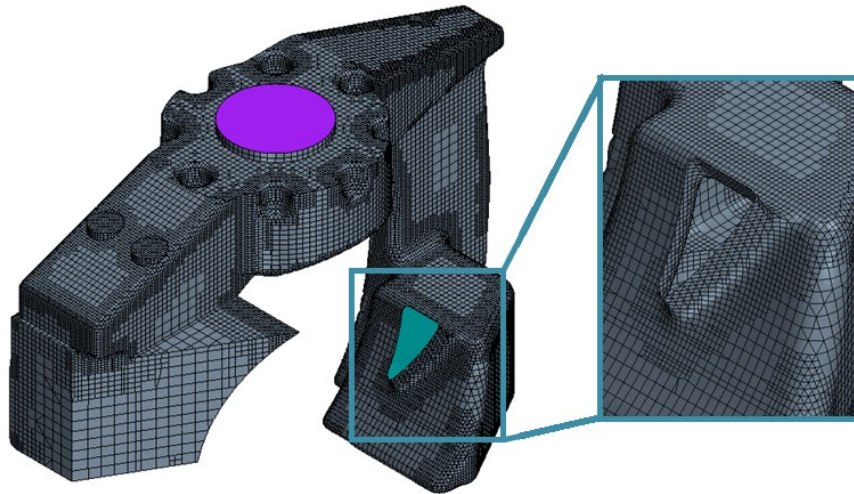


Figure 87: numerical grid of the inlet distributor, with the lower suction port grid magnified

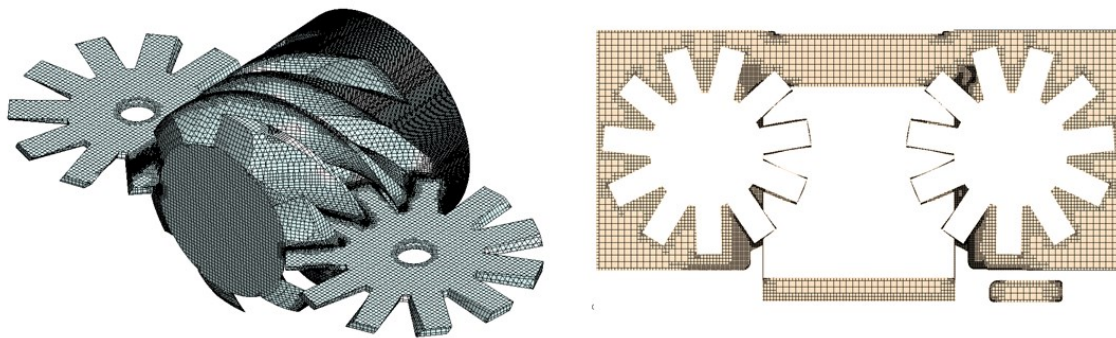


Figure 88: numerical grid of the rotating parts (left) and on a section plane normal to starwheels axes (right)

4.5.2 Results: Inlet distributor

The analysis of the inlet distributor has been carried out in order to show the different behaviors showed by oil droplets which differ from each other in terms of droplet diameter; three values have been considered: $0.50\ \mu\text{m}$, $5.0\ \mu\text{m}$ and $50\ \mu\text{m}$. This range was selected according to values reported in literature, for example the works from Stošić et al. [98] and De Paepe et al. [86].

The mass flow rate of refrigerant at the main inlet of the expander was set at $0.3\ \text{kg/s}$, according to the results reported in [87], while at the two admission ports a static pressure equals to $1.3\ \text{MPa}$ was imposed. A 10 % by weight of oil was injected at the main inlet port ($0.003\ \text{kg/s}$), according to the analysis reported in [34]: to run a transient analysis of the oil film evolution during time without affecting the robustness of the solution, the lubricant stream has been injected only after the convergence of the refrigerant flow field. Given these conditions, the results obtained for the three different diameters of the droplets are reported in Table 17. As it is possible to observe, the number of droplets which are able to reach the

suction ports it is a strong function of their diameter: the fact is that the path of droplets is strongly influenced by the particular shape of the inlet distributor. As it is possible to see in Figure 89, fluid streamlines shows that the lower inlet port area is affected by eddy structures given by the shape of the duct, while the upper port is placed immediately upstream of the right-angled curve of the duct. The curved shape of the walls above the lower port influence the trajectories of the droplets characterized by the smallest diameter, while this effect is less sensible for the 50 μm -size ones, because of their higher inertia, Figure 90. This analysis is important because, in an actual application, an oil injector does not provide droplets of constant diameter, but just a certain distribution in a certain range of dimensions (as reported in [98] and [86]). Thanks to the results reported below, it is possible to notice that smaller droplets were able to follow the bulk flow streamlines, but they provided a limited flow rate of oil at both the ports, since they impinged on the surfaces of the distributor far from the ports, driven by the refrigerant bulk flow; on the other hand, the same happened for the heaviest particles, but the driver is not the gas flow but their mass, which led to lubricant to impinge onto the surface placed beneath the injector and, by dripping along the distributor face, to enter the upper port. This dripping prevented the particles to enter the lower port, since a 90-degree bend is placed directly upstream the opening to the expansion chamber, leading the lubricant to fall on the underlying surface under the effect of gravity. To show how, after a 0.5 s, lubricant is spread on the distributor surfaces, Figure 91 is shown: it is clearly visible the phenomenon described few lines above, where the oil film started to flow from the surface in front of the injector and covered the surface above the upper inlet port while it did not reach the lower port. The interaction between the lubricant which is able to reach the ports and the screw rotor is shown in the paragraph below.

Table 17: oil droplets distribution

Oil droplet diameter [μm]	Oil droplets at the upper port [%]	Oil droplets at the lower port [%]
0.50	0.99	0.03
5.0	3.39	0.05
50	5.69	0.00

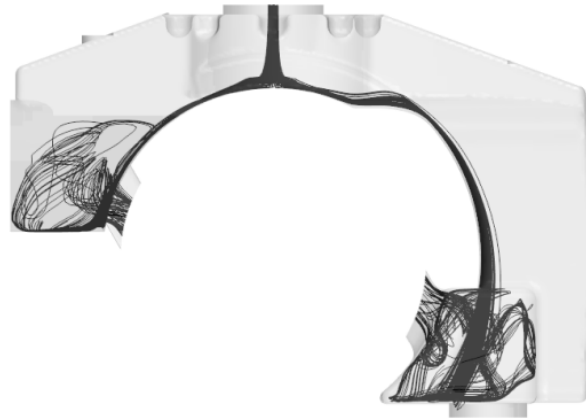


Figure 89: flow streamlines in the inlet distributor

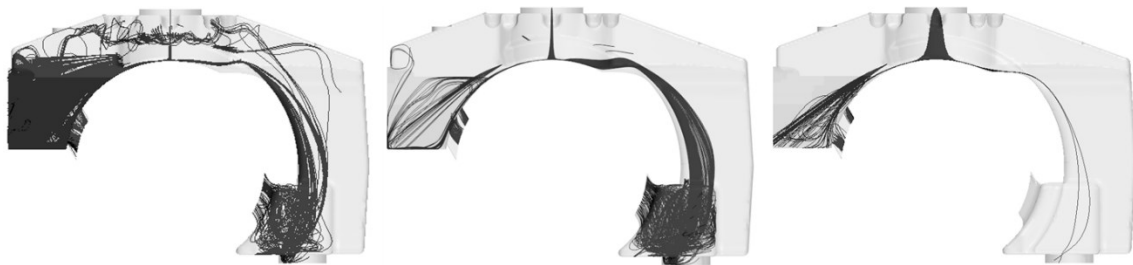


Figure 90: trajectories of the oil droplets. 0.50 μm (left), 5.0 μm (center) and 50 μm (right)

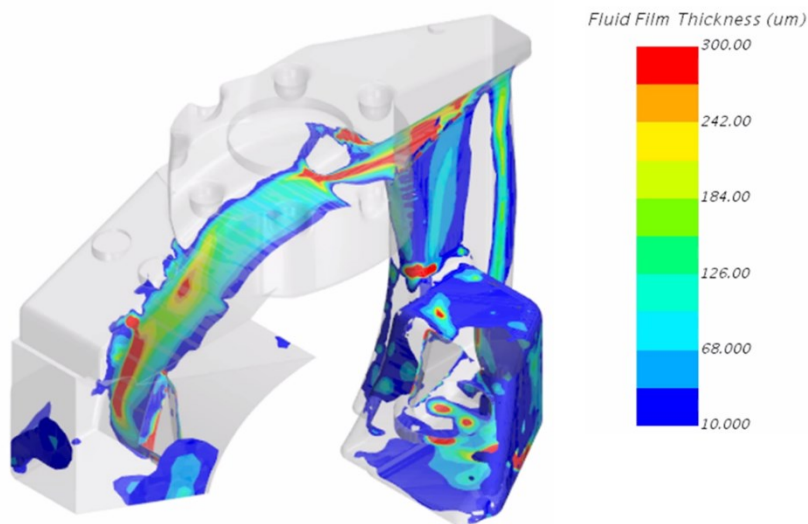


Figure 91: oil film thickness on the distributor surfaces after 0.5 s from injection start

4.5.3 Results: Oil – rotor interaction

Another result which was obtained thanks to the CFD analysis was the lubricant behavior when both the admission ports were completely obstructed by the screw rotor, occasion which happens for each revolution of this part. As already stated, when this configuration of the machine takes place, the amount of mixture which flows into the expansion chamber is only given by the clearances between the screw and starwheel rotors and the housing,

together with a non-negligible stagnation of the mixture trying to enter the machine and the resulting back pressure. The relative position of the screw rotor and the upper suction port for the studied condition is showed in Figure 92, with the port highlighted in red. For the case herein reported, a pressure of 1.3 MPa was imposed at the main inlet of the machine, while 0.3MPa is the value at the outlet, in agreement with data reported by Ziviani et al. [87], together with the screw rotational velocity of 3000 rpm and the one relative to starwheels linked to the engaging ratio, as reported in Table 16.

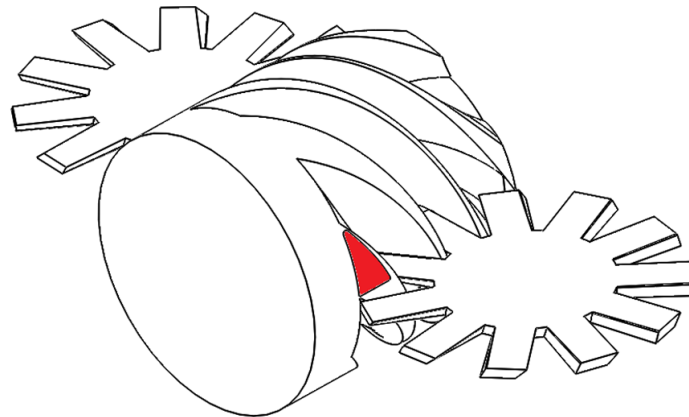


Figure 92: relative position between the screw rotor and the inlet port (red trace) for the considered instant

The first result to be shown is the lubricant film thickness on the screw rotor walls, for the case of droplets with a diameter of 50 μm . In Figure 93, the distribution of oil after 0.5 s is showed; it can be seen that on the lower part of the screw the film was thicker than other positions, but the maximum oil accumulation took place downstream the engagement zone: this is probably given by the oil droplets trajectories. These droplets escaped in the direction of the lower part of the main rotor because of the existing pressure gradient, as showed in Figure 94: the only part of the screw exposed to the inlet pressure was the one directly upstream of the inlet port, while the rest of the surface was subjected to lower pressure values, just a little greater than the discharge pressure of the entire machine. This explains also the presence of oil in the rear part of the screw: from Figure 94, the region near the inlet port was characterized by a massive pressure gradient, around 1.3 MPa, generated by the combination of both the stagnation caused by the screw and the gaps between the screw rotor and the housing.

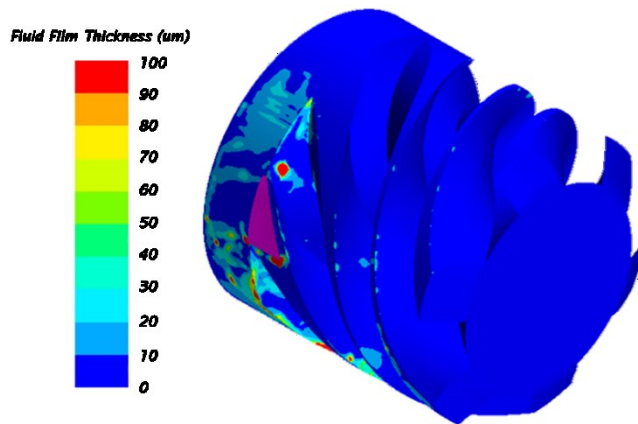


Figure 93: oil film thickness on the screw walls; the upper inlet port is highlighted in pink

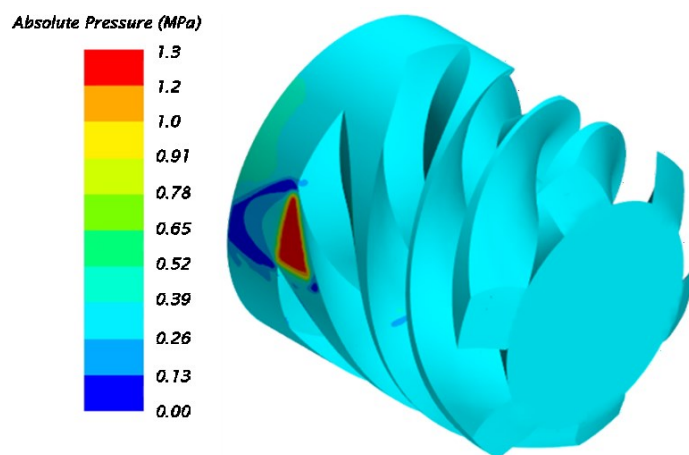


Figure 94: absolute static pressure on the main rotor surface

This was confirmed also by considering Figure 95. The streamlines show that when the refrigerant – oil mixture exits the upper inlet ports through the gaps, it is split in two directions, upstream and downstream the admission port. By checking the velocity magnitude of these streamlines, it is visible that the mixture being pushed in the rear part had a relatively slow velocity, below 10 m/s, while the one which flowed on the bottom of the screw up to the expander outlet port showed velocities up to 80 m/s. These lower speeds, combined with the small gap width between the screw and the housing, led to a certain sealing effect in the rear part of the machine (as visible from Figure 93, the average oil thickness on those surfaces was greater than 20 μm). On the other hand, in this way only a part of the injected mass of oil was pushed forward to the meshing region and, among this, an insufficient flow reached the coupling between the screw and the wheel. It is then clear that, by injecting oil at the main inlet port of the expander, inadequate lubrication is provided during a certain position of the main rotor. Another aspect which has to be considered is that this “sealing effect” can cause a sort of blockage, with the consequent increase in pressure

losses, if the working fluid flows with high velocity through sealed gap. For this reason, it is important to limit this effect in the rear part of the screw, upstream the admission port, not to limit flow of the working fluid toward the screw and the expansion chamber.

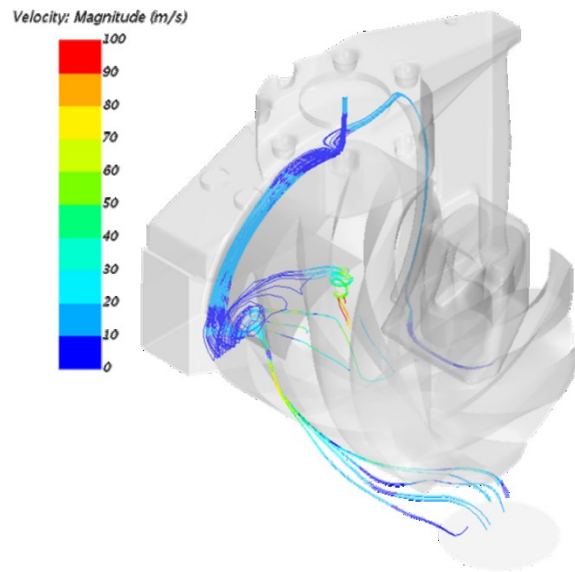


Figure 95: mixture streamlines inside the expander

Another useful piece of information which was possible to derive from transient simulations was the oil film evolution during time. Figure 96 shows the evolution of the lubricant film thickness during time, starting from the initial growth in the surface under the injector and ending with the oil stripping in the distributor branch leading to the upper inlet port. In the first moments, the oil film assumed a roughly circular shape linked to the geometry of the injector (solid cone) and it did not appear equally distributed with respect to the screw mid-plane. Thereupon, lubricant flowed to the upper port, whose feeding duct was steeper than the other one: the action of gravity force was dominant over the drag force given by the refrigerant being injected in the machine. For the very same reason, the oil droplets were not able of being distributed on every duct surface, but they accumulated on the lower ones. Finally, when oil film reached the inlet port, it has been split in two ways, one in the lower part of the screw and one behind the screw, has already reported a few lines above.

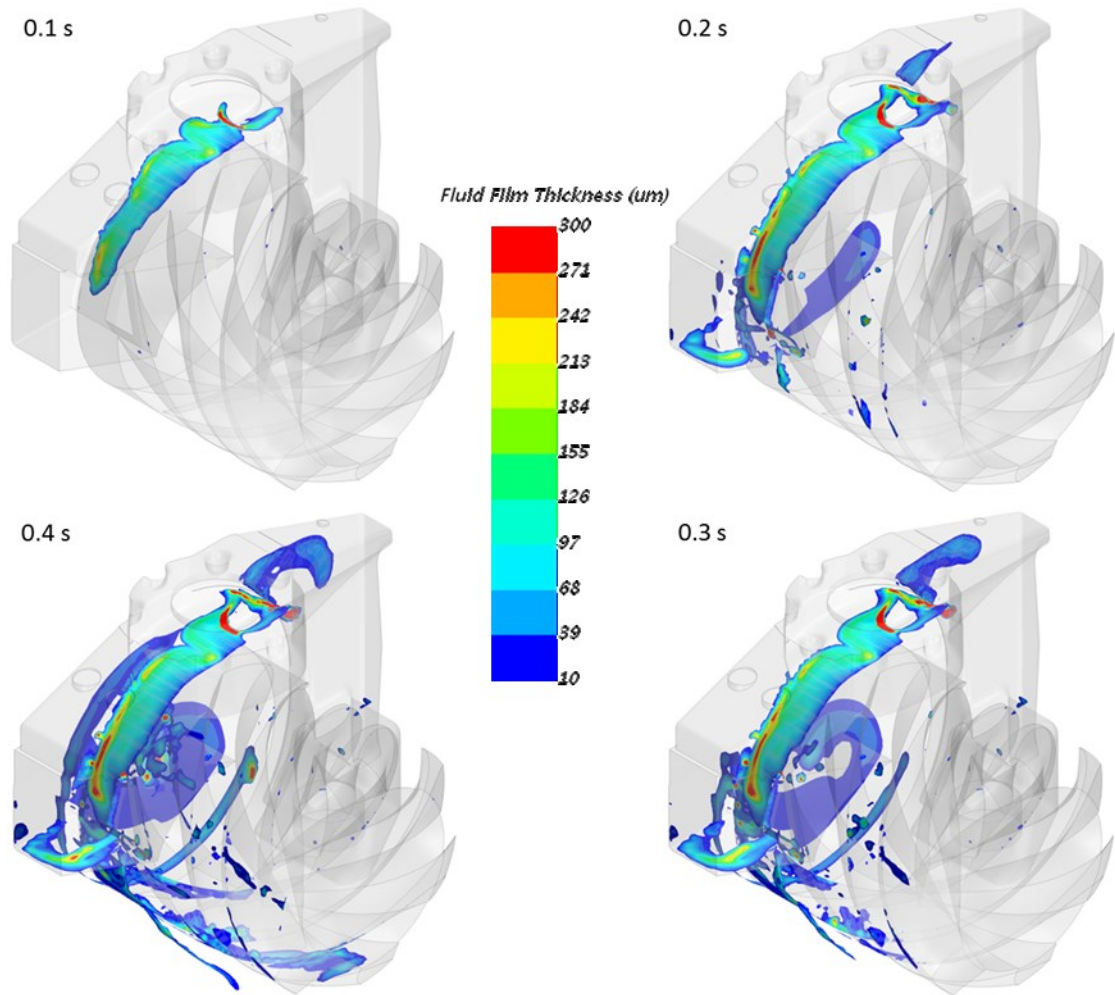


Figure 96: oil film evolution in the expander during time

4.6 Analysis of an oil-free single screw expander

In paragraph 4.5, the single-screw expander (SSE) device has been analyzed focusing on lubrication for a particular working condition. Since oil distribution was the main objective of the study, the performance of the machine in terms of shaft torque, pressure pulsations and more in general transient phenomena which take place inside the machine were neglected. To investigate also these phenomena, an approach based on 3D,CFD, transient simulations of the same machine has been adopted. The main complication in simulating a single screw machine is represented by the correct representation of the working chamber volumes, together with the modeling of the meshing region between the screw rotor and the starwheels. For these reasons, several approaches are reported in literature (as reported by Casari et al. in [99]), but the ones using CFD methods are scarce. It was then decided to study the expansion process taking place in such expanders by continuing to use STAR-CCM+[®] CFD tool. The investigated SSE was the same of paragraph 4.5, thus the considerations made by Ziviani et al. in [34] still remain valid, as the ones regarding steady-state simulations made by Suman et al. in [100]. Also the geometry and the fluid model depicted in both Figure 84 and Figure 85 remain valid for the current analysis; what differs are the numerical models adopted for the transient analysis.

4.6.1 Numerical model

To model the interaction between the main rotor and the starwheels, the CFD simulation was carried out using the overset mesh method; this modeling technique has already been illustrated in paragraph 4.3 for the scroll expander simulation, thus details were given in that occasion. Adapting this approach to the actual geometry of the SSE, the background region is represented by the housing, while three moving meshes are present, the couple relative to the two starwheels and the one for the screw rotor. This modeling technique has been applied with a polyhedral mesh, with prism layers near the boundary walls, which are useful to couple the four different regions of the simulation. In this respect, the dimensions of mesh elements have to be chosen as a compromise between a fine mesh, which leads to an unaffordable computational time, and a coarse grid which could lead the overset algorithm to fail when coupling the different regions. In fact, the overset criterion requires at least five elements in the overlap region for each sub-grid: since discretization error is minimized for elements of similar size, it is better to have small and regular-shaped prismatic cells in the overlapping meshes. Following this rule, a total number of elements slight above three million was obtained, with a minimum cell quality value required to obtain a robust and accurate solution well above the minimum value required by the software [80]. The mesh

which was obtained after a sensitivity analysis linked to the robustness of the overset coupling and fluid dynamic behavior is shown in Figure 97. To increase both the accuracy and robustness of the simulations, also the close proximity and overlap volume calculation models were enabled: the former prevents solver failure when overset regions intersect background physical boundaries, while the latter is needed to calculate with a greater accuracy the volume of the overset regions which partially overlap. To increase even more the robustness of the simulation, the zero-gap approach was enabled: with this approach, the requirement of five cells-per-grid in the overlapping region is no more mandatory; on the other hand, the gaps between the screw rotor and the starwheels are not modeled anymore, preventing the calculation of the leakage flow in this area. This happened because when the distance between the overset regions and the background one is below two layers of cells, these layers are removed. This feature has been used to model the meshing region between the main rotor and the two gaterotors because, in the real expander, low friction material is placed to seal the gaps thus the leakages in this area are assumed to be negligible. On the other hand, the actual clearance between the screw rotor and the housing has been entirely meshed, with the consequent refrigerant leakages solved.

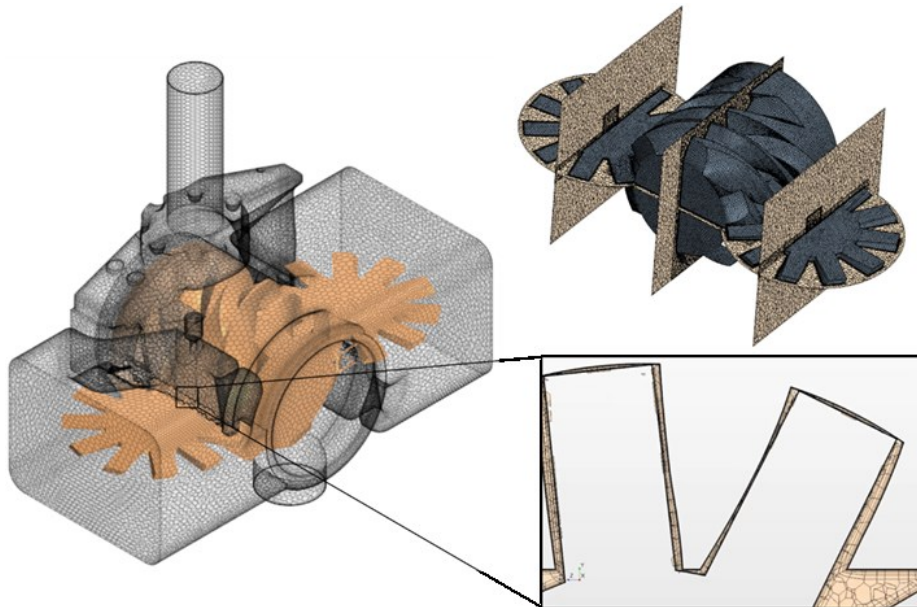


Figure 97: computational mesh, with a detail of the prism layers near the boundaries of the domain

The dimension of grid elements and the flow characteristics led to y^+ included in the range between 0.5 and 100; this fact suggested the choice of the “all- y^+ ” approach, in order to blend the solution of the viscous sublayer with the values derived from the application of the wall functions.

As in the case presented in paragraph 4.5, the refrigerant flow has been modeled as a real gas using the Redlich – Kwong equation of state, because of the compressibility factor at the inlet of the machine. After the flow initialization conducted by considering the working fluid as an ideal gas, quantities such as fluid density, dynamic viscosity, specific heat and thermal conductivity were defined using 6th-order polynomials as functions of temperature, defined in the range 370 K – 490 K for a fixed, mean pressure value of 0.7 MPa. In the relations depicted below, the polynomial coefficients are based on the value for R245fa refrigerant calculated by means of CoolProp library [52]:

$$\rho(T) = 4.09931 \cdot 10^3 - 51.4944 \cdot T + 2.75807 \cdot 10^{-1} \cdot T^2 - 7.95793 \cdot 10^{-4} \cdot T^3 + 1.29954 \cdot 10^{-6} \cdot T^4 - 1.13664 \cdot 10^{-9} \cdot T^5 + 4.15521 \cdot 10^{-13} \cdot T^6 \quad (3)$$

$$\mu(T) = 1.36941 \cdot 10^{-4} - 1.71320 \cdot 10^{-6} \cdot T + 9.41708E \cdot 10^{-9} \cdot T^2 - 2.71200 \cdot 10^{-11} \cdot T^3 + 4.41423 \cdot 10^{-14} \cdot T^4 - 3.85050 \cdot 10^{-17} \cdot T^5 + 1.40482 \cdot 10^{-20} \cdot T^6 \quad (4)$$

$$c_p(T) = 114289 - 1473.29 \cdot T + 8.01954 \cdot T^2 - 2.33812 \cdot 10^{-2} \cdot T^3 + 3.84972 \cdot 10^{-5} \cdot T^4 - 3.39070 \cdot 10^{-8} \cdot T^5 + 1.24708 \cdot 10^{-11} \cdot T^6 \quad (5)$$

$$\lambda(T) = 0.488758 - 6.56741 \cdot 10^{-3} \cdot T + 3.74448 \cdot 10^{-5} \cdot T^2 - 1.13603 \cdot 10^{-7} \cdot T^3 + 1.95527 \cdot 10^{-10} \cdot T^4 - 1.80420 \cdot 10^{-13} \cdot T^5 + 6.95612 \cdot 10^{-17} \cdot T^6 \quad (6)$$

The rotational speed of the main rotor was 3000 rpm and the one of the two gaterotors was set up accordingly; the time step adopted for the transient simulation was 1e-6 s. To initialize the domain, a static pressure of 0.7 MPa and a temperature of 320 K was imposed inside the housing. The boundary conditions were represented by a pressure of 1.2 MPa at the inlet section of the expander and one of 0.2 MPa at the exhaust port; the inlet temperature was set up to 390 K. About the domain surfaces, these were considered adiabatic and hydraulically smooth; all these operating conditions were realistic if compared to the one resulted from the experimental campaign whose results are showed in [34].

4.6.2 Results: Pressure field

From Figure 98, total pressure evolution on the screw rotor is shown for different angular positions. It is possible to see how the refrigerant pressure smoothly decreased from the triangular admission port to the outlet of the machine, from the left to the right of each snapshot, where pressure reached the value imposed at the outlet port, even if some region were affected by a slight under expansion. This was probably given by the combined effect of helix angle and shape of the groove, the latter position with respect to the outlet port and the actual pressure ratio imposed to the machine with respect to its geometric volume ratio.

When focusing the attention on the inlet port, it can be seen (from the snapshot taken at $\theta=0^\circ$) that the screw rotor surface opposite to the suction port is subjected to a huge pressure gradient, generated by the effect of both the gaps between the screw and the housing and the

fluid stagnation given by the screw groove. Other interesting results (showed in Figure 99) have been obtained by placing a virtual probe directly in front of the admission port; the average pressure measured at this port was different with respect to the one imposed at the main inlet of the SSE (1.2 MPa), because of the pressure losses induced by the inlet duct, which was responsible of the subdivision of the flow at the inlet of the machine in two streams, one for each duct branch up to the respective admission ports. Moreover, the screw rotation induced a dynamic behavior which influenced the instantaneous value of pressure. By observing the pressure trace, the combined action of the screw rotation and its groove shape yielded to a partial obstruction of the flow area for the working fluid entering the expansion chamber. This fact contributes to noise and vibration of the expander and has to be considered when designing the ORC system, in order to avoid resonances which could be detrimental for the performance of the entire cycle or the ones of the measurement system, as already reported in paragraph 3.3, where these it was shown how the flow pulsations induced by another rotating component of the cycle (the pump) influenced the behavior of the Coriolis flow meter, placed upstream the positive displacement machine.

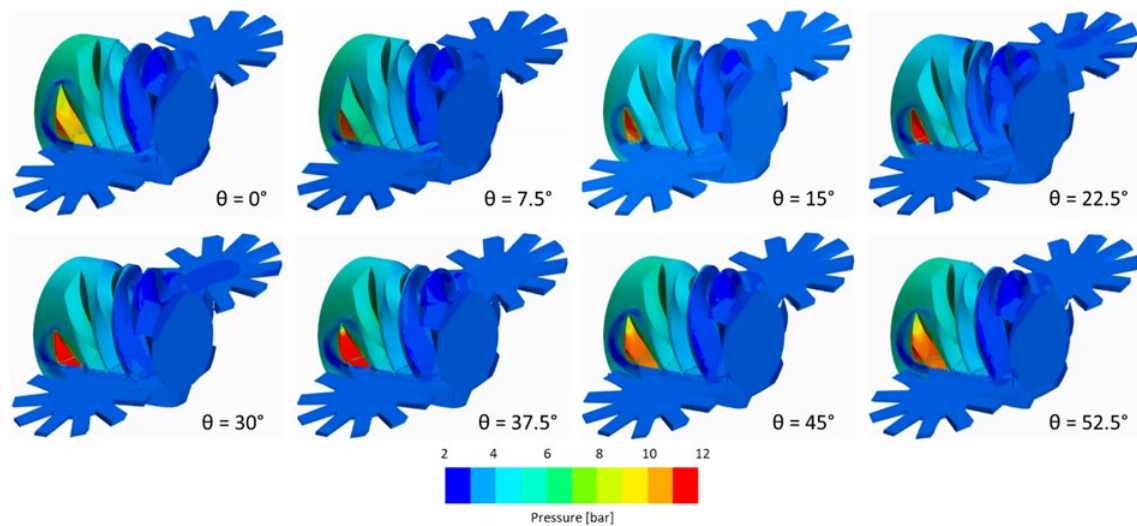


Figure 98: total pressure on the screw rotor for several angular positions

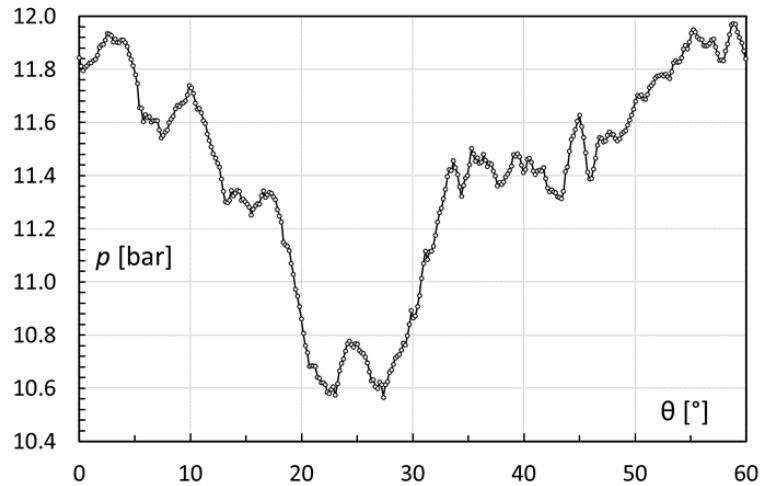


Figure 99: pressure profile at the upper suction port as a function of screw rotor angular position

The last result regarding the pressure field in the machine regarded how the expansion process took place in the expander, from the triangular inlet port up to the exhaust opening. To do so, six different virtual probes have been positioned in the points showed in Figure 100: the first is placed in the middle of the intake port, while the last is located at the end of the main rotor. For each of these points, static pressure was measured and, by combining these values, the trend reported in the right-hand side of Figure 100 was obtained. From this graph, it is visible how almost three quarters of the pressure decrease from the inlet to the outlet sections took place during the first twenty degrees of rotation of the screw rotor, before the pressure started decreasing in a much more gradual way up to its exhaust value. This behavior was certainly influenced by the dimension and position of the inlet port, as well as the shape of the groove. Furthermore, pressure evolution was influenced by the leakages in the high-pressure side of the domain. The clearances named “flank gap” and “tooth-head” in Figure 101 characterized the matching between the meshing parts, even if anti-friction material is added to the starwheels.

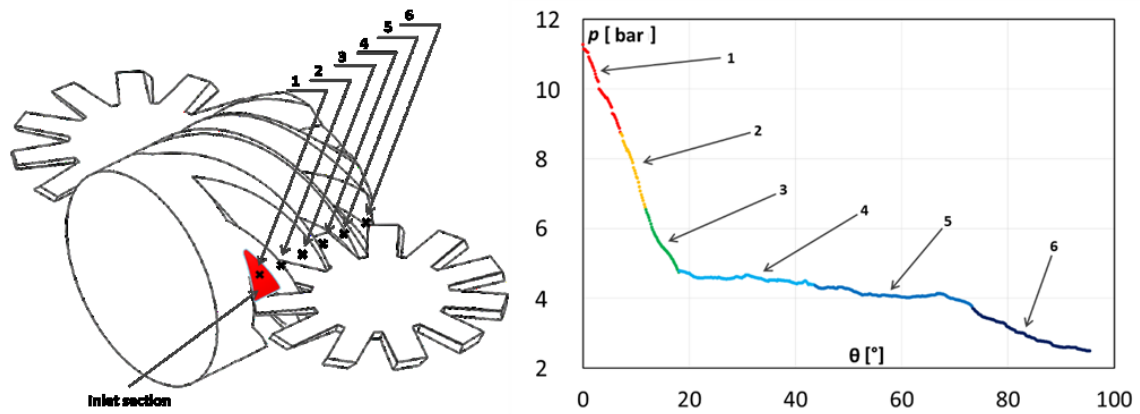


Figure 100: positions of the virtual probes (left) and resulting pressure trend during expansion as a function of rotor angular position(right)

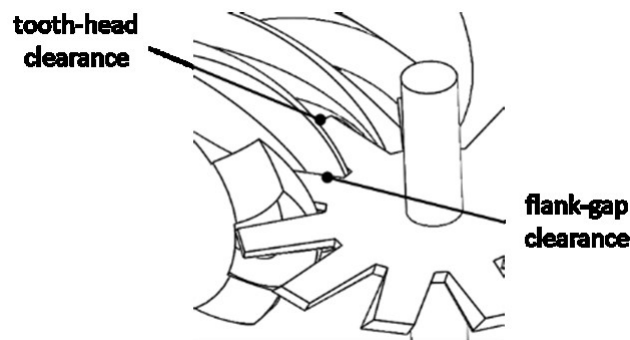


Figure 101: clearances in the meshing region

4.6.3 Results: Flow field

The study of the flow field inside the machine is of paramount importance to its bond to the pressure one; from Figure 100 it is visible how, in front of the inlet section, the pressure was just a little greater than 11.5 bar, meaning that also 0.5 bar were lost in the feeding duct. In fact, the section of a volumetric machine which is responsible for the connection between the rest of the system and the rotating part(s) is frequently responsible for sensible pressure losses which affect the global efficiency of the machine. For the single screw expander analyzed in this thesis, the feeding duct has to distribute the refrigerant entering the machine from the inlet section to the two admission ports located in two opposite sides of the machine. As reported in paragraph 4.5, the duct is not symmetric with respect to the rotational axis of the screw rotor, thus it is characterized by two branches of different length, which lead to different flow fields for the two admission ports, as reported in Figure 102 and Figure 103, in terms of velocity magnitude. By analyzing the first of these two pictures it is visible how, just in front of the admission port, recirculation took place, probably given by the combination of both the change in passage area and the variation in shape of the duct, which

determine non-uniform flow conditions in the terminal part of this distributor branch. A similar reasoning can be done for the longer branch: here, to the effects given by the variation of the cross-sectional area and the shape of the duct, also the presence of two bend imposed a certain non-uniformity in the flow. The admission port of the long duct was placed in the upper part of the section of the distributor facing the expansion chamber, with a certain free volume underneath it, contrary to what happens in the short branch, where a little fluid was allowed to recirculate beneath the inlet port. For this reason, the flow field inside the longer duct appeared to be more disturbed and more prone to recirculate than the one which passed through the shorter branch: the lower portion of the admission port was not fed as good as the port on the other side of the duct, with the birth of a counterclockwise vortex given by the stream of refrigerant which flows on the vertical part of the duct.

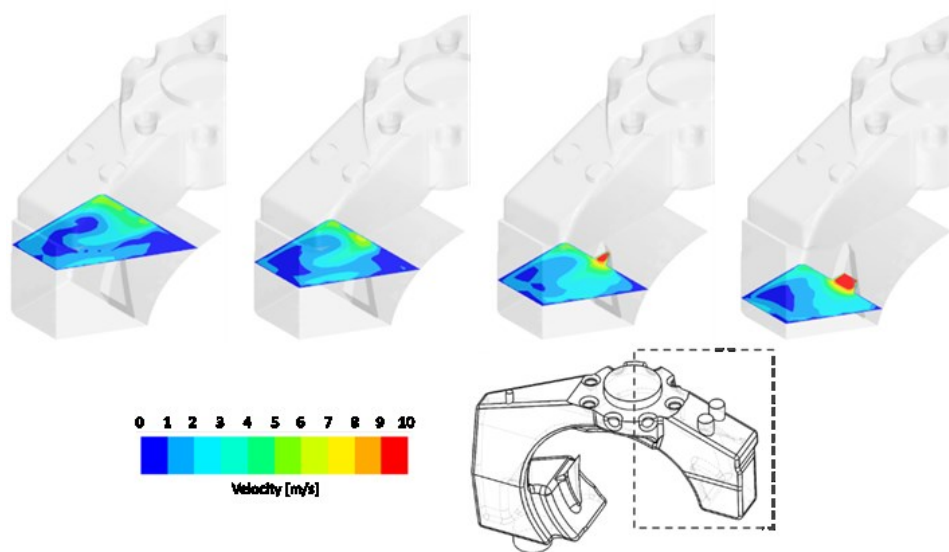


Figure 102: velocity magnitude of the refrigerant flowing to the upper admission port

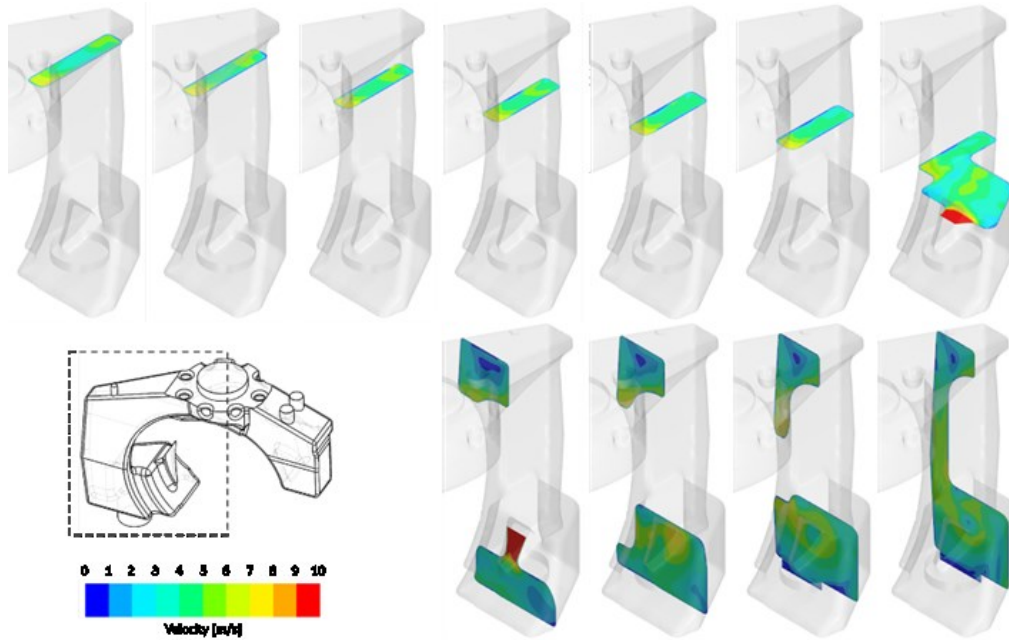


Figure 103: velocity magnitude of the refrigerant flowing to the lower admission port

Another interesting result is linked to the variability of the mass flow rate during the operation of the expander, as a function of the angular position of the screw rotor. In fact, as said a couple of pages above, the succession of teeth and grooves in front of the admission ports led to flow pulsations, as visible in Figure 104, whose frequency is linked to the number of the grooves and the rotational speed of the main rotor.

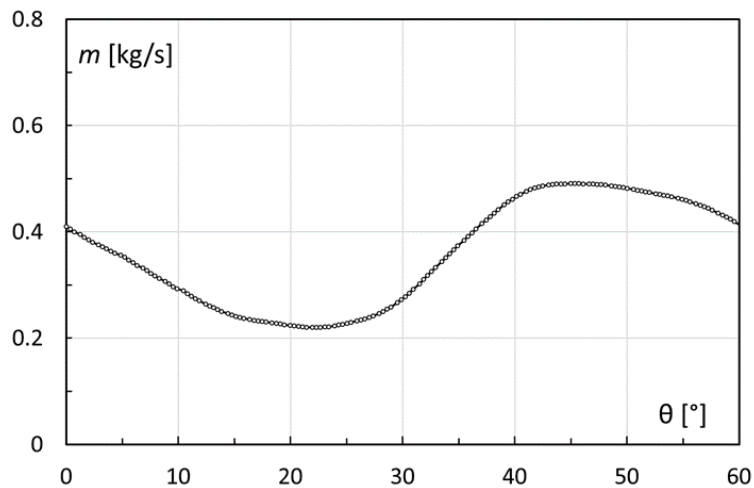


Figure 104: mass flow rate pulsation at the inlet of the machine as a function of the angular position of the screw rotor

The flow pulsated around the mean value of 0.36 kg/s, with a peak of 0.49 kg/s and a minimum value of 0.22 kg/s. By comparing this data with the one resulting from the characteristics reported in Table 15, a Volumetric Flow Matching ratio (VFM) higher than one resulted; in particular, with the data computed with the current model, the average VFM

was around two. So, when comparing these results with the ones coming from the experimental campaign showed in [87], it is clear that a couple of effects have not been considered: the sealing effect guaranteed by the lubricant and the difficulties for the numerical tool to detect the contact between the main rotor and the gaterotors, which guarantees itself a certain leakage-preventing action. To better understand how leakages impacted on the results of the numerical campaign, the most important clearances of the machine were analyzed.

Following the refrigerant path from the admission port of the expander, the first clearance to be met was the one between the screw rotor and the single screw expander housing, located at the triangular admission ports. This gap led to leakage of the working fluid behind the main rotor, with its consequent recirculation, and it is depicted in the left-hand side part of Figure 105. This is the same result which has been shown in paragraph 4.5: in that occasion, the oil was pushed in the same region of the expander and did not participate in lubricating the meshing zone. Another clearance through which the refrigerant escaped was the one showed in the right-hand side of the same figure of a few lines above; the gas passed through the gap between the groove and the housing, leading to unexpanded fluid to escape the domain via the outlet port. Also in this case, a layer of oil in the real machine would have limited this phenomenon, visible in Figure 106. From the picture on the left-hand side, it can be seen how velocity reached values greater than 200 m/s, since the gaps acted like nozzles through which the fluid expanded from an high pressure zone to a low pressure one, namely two adjacent grooves (right-hand side of Figure 106). This increases the flow rate of working fluid passing across the machine (without exchanging its energy to the screw), lowering the global performance of the single screw expander.

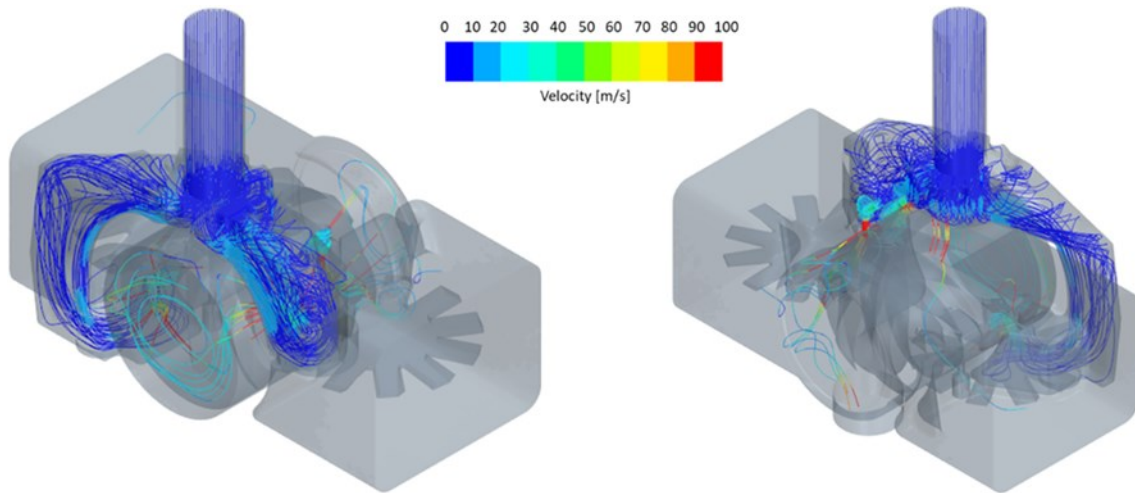


Figure 105: flow recirculation behind the main rotor (left) and across the clearance between the groove and the housing (right)

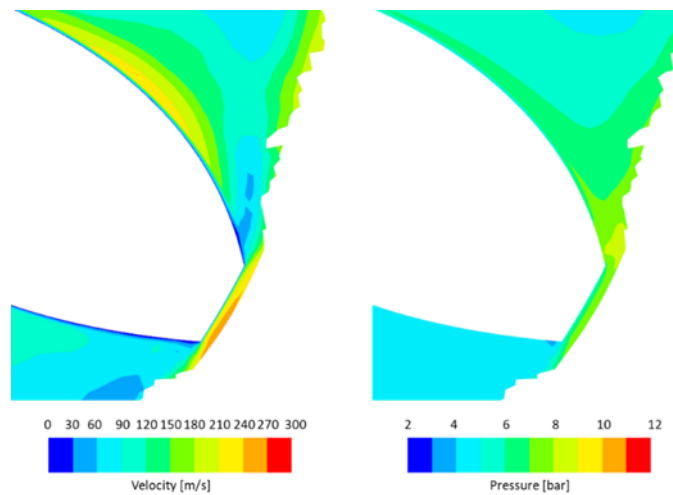


Figure 106: flow escaping through the clearance between the main rotor and the housing: velocity (left) and pressure (right) fields

About the performance of the machine, having run a transient simulation it has been possible to calculate the torque output at the shaft of the main rotor, by considering the pressure, dynamic and fluid friction forces acting on the screw. Since greater the pressure on the grooves, greater the torque, in Figure 107 the trend of the torque is superimposed with the pressure trend obtained by means of two numerical pressure probes placed at the two triangular admission ports. Torque instantaneous values fluctuated around their mean value of about $\pm 15\%$, which is in line with a smooth operation of the device taking advantage of the screw shaft power. As it is possible to see in both graphs, during a complete revolution of the screw rotor six pulsations in both pressure and torque took place; this was expectable, since the screw had six grooves which, during rotation, periodically occlude both the admission ports. When this happens, peak values for pressure are visible at both the ports,

which correspond to a minimum value for the torque measured at the shaft of the expander. When considering only the pressure graph, it is clearly visible how the values of pressure measured at the lower admission port (dashed lines) are different with respect to the ones detected at the upper one: the lower minimum value was given by the greater pressure losses which characterized the long admission duct, while the higher pressure peak was probably given by the dynamic effect provided by the higher amount of fluid present in the long branch, similarly to the ram effect which takes place in the feeding ducts of the water turbines, in hydroelectrical plants. For this reason, both the designs of the admission ports, in terms of size and position, and the one of the screw rotor (groove volume as a function of screw helix angle) have to be optimized to reduce pressure pulsations, which lead to vibration and noise [101].

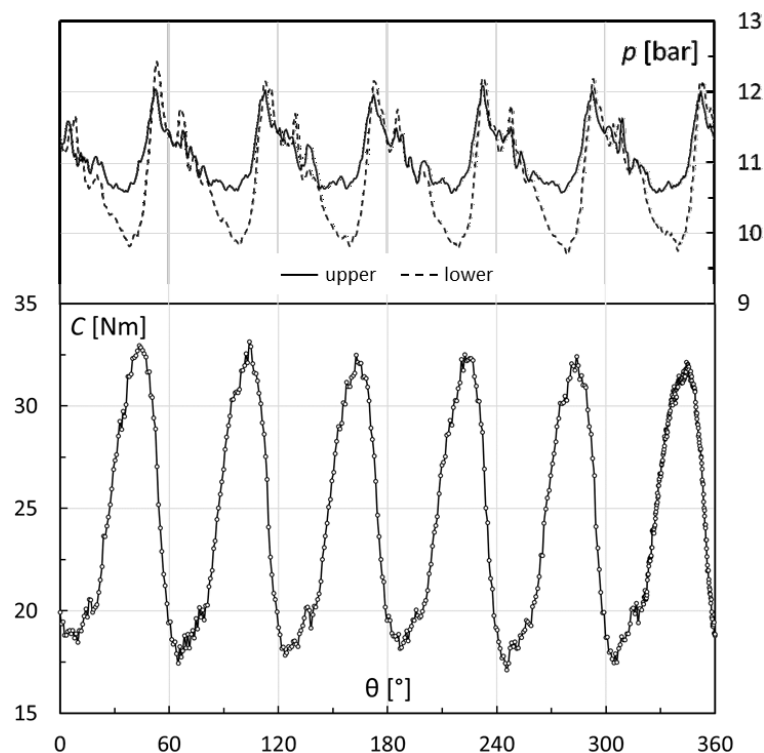


Figure 107: pressure trends at the admission ports (top) and torque (bottom) at the screw shaft as a function of the main rotor angular position

An alternative approach to Whole ORC Modeling

5.1 Introduction

As reported in chapter 3, several strategies are available when the modeling of an entire ORC system is required. The choice between three-dimensional, one-dimensional and lumped parameter simulations has to be made by considering the trade-off between the accuracy of the solution and the available computational resources: for this reason, it has not been possible to model a real, complete system with its actual components, but just a simplified scheme. It is then apparent that if both CFD simulations of the main components and their interaction want to be studied, a hybrid approach which couples these devices by means of 0D-modeled pipes, valves and fittings has to be considered. On second thought, another possibility to link the heat exchangers, the pump and the expander is simply to copy the fluid properties at the outlet of each of these devices and paste them at the inlet of the downstream machine. In doing so, effects such as pressure and thermal losses of the working fluid passing through pipes and valves are neglected, but a simulation capable of linking the various parts introducing a nearly zero computational cost can be attractive, because the propagation of the effects of varying boundary conditions from a component to another can be studied: an example can be the calculation of how the net torque available at the shaft of the expander is modified by a decrease of the heat flux to which the evaporator is subjected. With a traditional approach, the user should manually export and then import data between the simulations of adjacent machines, increasing the time required for the simulation and requiring the operator to focus on this task rather than carry out activities with a greater value. This is not the only advantage of adopting such a method (which, on the other hand, is not even novel: several software allow the so-called “co-simulation”, in which the two numerical tool are coupled and exchange data, as in the case of STAR-CCM+[®] and AMESim[®], see references [80] and [102]): by writing a script in an open source language, it is possible to easily adapt it to the characteristics of the dialoguing CFD tools while, if at a certain point the user wants to model also the behavior of the elements connecting the

machines, it is possible to do so by inserting models of such components, for example the ones in the library created by Bell [103].

Given this, a brief script has been written using Python 2.6.6 programming language [104]. The main objective of this work was to show the feasibility of this solution so, by reading it, it is clear that the script could have been optimized in different areas (such as memory allocation and parallelization). Nonetheless, it shows how two different software, developed by two different software houses, can be connected by means of an open source tool.

5.2 Software employed

As introduced in the previous paragraph, the Python script was used to transfer data from one component to another, each simulated with a different commercial tool. In order to do so, CFD packages had to satisfy a couple of requirements:

- The software had to show the capability of being controlled by means of a batch job (which is a series of commands that are executed by the software without human intervention [105]);
- Output data for each of the simulated machines had to be put in a file easily accessible with standard tools.

Given these two points, the software which have been used in the current analysis were Siemens STAR-CCM+[®] ver. 13.02 and Convergent Science CONVERGE ver. 2.4.29, which have also been used to simulate the single components whose analyses have already been shown in chapter 4. The Python script was used to grab data according to the scheme presented in Figure 108:

- The heat exchangers were supposed of being modeled with STAR-CCM+[®] following the path depicted in paragraph 4.2;
- CONVERGE was the tool that was chosen to model the expander.

As it is required for the WOM approach, also the behavior of these three components have to be modeled with transient simulations to take into account the effects which the variation of the working conditions of one device can have on the entire system; this means that the output properties for each device have to be stored and then accessed by the machine placed downstream, which will use this data as its new boundary conditions at the inlet: the exchanged properties between the various components are pressure and temperature at the inlet and outlet sections of each component. Focusing on the two software used in this case, the formats of the output and input files are reported in Figure 108.

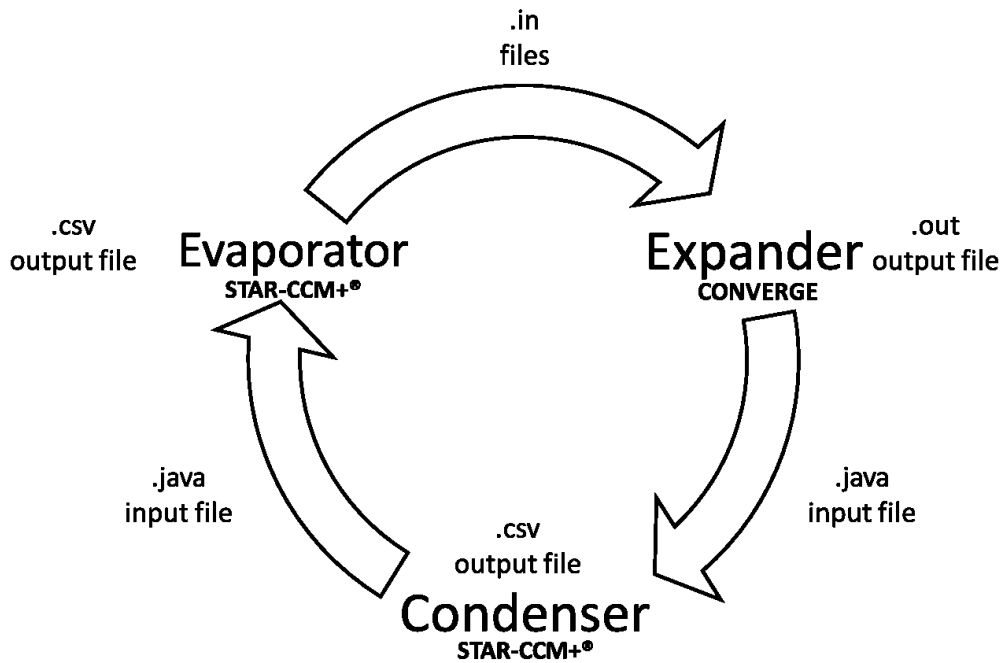


Figure 108: interactions between the CFD tools

The two *.java* files are the macros which are required to set-up the simulations in STAR-CCM+®: these two files have been generated with the macro recording function which is available in this CFD tool, and the script which was obtained was then modified to better adapt to the automated algorithm. Their structure, for both the condenser and the evaporator, is the same: the differences stay in the temperature and pressure of the phase entering the device (vapor for the condenser and liquid for the evaporator). The other difference was in the name of the file containing the output data: for each heat exchanger two *.csv* files were generated, one containing the value of temperature and the other the one for pressure at the outlet of the device. The *.java* script which has been used to command condenser simulation is reported in appendix B.

The two other file extensions which are visible in Figure 108 are *.in* and *.out*, and are linked to the part of the analysis carried out with CONVERGE; starting from the latter, the average pressure and temperature at the inlet of the condenser are taken from the *mass_avg_flow.out* and *area_avg_flow.out* files: it is necessary to read both of these scripts because the heat exchangers require, as inlet boundary condition, the static temperature and total pressure, so the first has to be read from the *.out* file containing the area averaged values of the parameters at the outlet of the expander, while the latter can be found in the *mass_avg_flow.out*. When focusing on the input quantities, these have to be imported in a different way than the one adopted for the condenser and evaporator simulations. While, for the heat exchangers, it was

possible to import both the boundary conditions at the inlet and simulation time step within the same file (the Java macro), in this case pressure and temperature at the inlet had to be imported through the *boundary.in*, while the simulation time-chosen with the Python script had to be defined with the *inputs.in* file. Another peculiar aspect of CONVERGE is the simulation restart. In the current approach, a serial run has been chosen to model the three components, meaning that the simulation of the evaporator is run first, followed by the one of the expander and then the solution of the flow field inside the condenser is calculated before exporting its outlet data to the inlet of the evaporator. In doing so, the *.csv* files created by STAR-CCM+[®] are updated at each iteration by adding a new line just below the ones already inserted in the previous iterations. In this way, the history of all the temperature and pressure values computed for each time-step are available even when the execution of the Python script is interrupted. On the other hand, in CONVERGE this does not happen, by default. If the simulation is not flagged as a *restart* in *inputs.in*, the software will overwrite the values calculated during the previous time-step and stored in the two “*flow_avg.out*” files. This fact will prevent the user to have all the pressure and temperature values computed up to the current time-step, so data post-processing would be impossible. To overcome this fact, it has been necessary to flag the simulation as a *restart* one: in this way, for each time-step CONVERGE generate and save on disk different *.out* files, which are then available to the user.

5.3 Python script

In this paragraph, the details on how data included in *.java* and *.out* files are manipulated for being included in the input files of the various devices are shown. The initial condition from which the script starts is given by the liquid state at the outlet of the condenser, so it is necessary to initialize both the *.csv* files at the outlet of this device with its pressure and temperature values. The Python script, which has been designed and tested on a calculator running Linux CentOS distribution release 6.5, acts as follows:

1. Liquid pressure and temperature values at the outlet of the condenser are read from its *.csv* file;
2. These values are increased of a user-defined quantity to account for the presence of the pump (for the script reported in appendix A, pressure is increased of 10 bar and temperature of 1 K);
3. The temperature of the walls of the evaporator is defined;
4. The new values for temperature and pressure of the liquid, plus the temperature of the evaporator walls are imported in the *.java* evaporator macro, launching its

simulation. Before doing so, the time-step value included in the macro is checked against the one defined in the Python main script and, if different, is replaced with the latter. This check between the time-step value defined in the Python script and the ones included in the *.java* and *.in* files is always done before starting the simulation;

5. After one time-step, the simulation stops and the values of pressure and temperature at the outlet port of the evaporator are read and used to define the state of the vapor at the inlet of the expander by copying them in the *boundary.in* file;
6. The *inputs.in* file is set-up to let CONVERGE execute a single-step simulation, before running it;
7. Pressure and temperature values at the exhaust port of the expander are read from the *mass_avg_flow.out* and *area_avg_flow.out* files, defining the refrigerant conditions at the inlet of the condenser by inserting them in the *.java* condenser macro, before running its simulation;
8. Simulation time is then incremented of a quantity equals to one time-step and the cycle continues up to the user-defined end time.

By reading the list above and by recalling what has been said in paragraph 5.1, it is visible that in the current version this approach simply exports thermodynamic quantities from the outlet of a certain device to the inlet of the downstream component. An improvement would be to consider any physic phenomena (such as heat losses in the pipes, pressure drops across valves and measuring instruments and so on) and modify the Python script accordingly. Even with this greater level of detail, the time required to perform an analysis of the system would be far lesser than running a 3D, CFD simulation for the entire cycle.

In this respect, let's consider the scroll expander simulation depicted in paragraph 4.4: that machine has been designed to deal with a mass flow rate of 0.0275 kg/s. At the outlet of the expander, the vapor has to be brought to the recuperator or the condenser by means of a pipe: by considering a 20 mm-diameter, 1 m long tube, together with vapor having the same physical properties of the one discharged by the machine introduced a few lines above, the time required for the fluid to reach the heat exchanger is slightly more than 0.1 s. By simulating such a duct with a CFD tool, it would require more than 30 minutes of simulation runtime, considering a time step of 5e-5 s and a computational time of 1 s per time-step. It is then clear how simulating each pipe in the system to obtain a full-3D, WOM simulation is quite time-consuming, since this runtime must be multiplied for each pipe in the cycle.

At this point, it can be argued that in this way the simulation of the entire system loses information about the heat exchange which takes place between the duct full of working fluid and the environment. This can give some cause of concern with those systems whose expander is operating with vapor in a state not so far from the saturated vapor curve, because of the characteristics of the heat source. This could lead the expander to operate with a certain percentage of liquid-phase fluid also at its inlet port, in addition to the more probable liquid presence at the end of the expansion. It is clear how this phenomenon is detrimental in terms of both cycle efficiency and expander mechanical integrity, thus it would be beneficial to take into account also the inevitable heat losses of the vapor exiting the evaporator in the duct towards this machine. To do so, it is possible to modify the proposed 0D, Python approach to consider also duct properties, as its thermal behavior and the head losses of the fluid through it, creating a cycle model less expensive, under the computational point of view than a full-3D one but still capable of providing accurate information, thanks to the combined lumped parameter-CFD approach.

By considering this coupling between the 0D and the 3D modeling techniques, it can be seen how the simulation method introduced in this chapter can be of use also to consider the mutual interaction between the system components. For example, still referring to the case of a few lines above, this method can be used to bring on a study on how cycle efficiency varies by gradually decreasing the thermal input at the evaporator. This exchanger and the expander are linked thanks to the Python script and by running several simulations, each one with different values for the heat input, it is possible to analyze the behavior of the expander for a vapor quality, for example, which tends forward one, realizing a flashing cycle. At the same time, it is possible to observe when liquid phase starts to accumulate at the end of the expansion process, in proximity of the exhaust port. By connecting also the condenser to these components, always with the Python script, the resulting variation in liquid level inside this heat exchanger can be assessed. It is clear, then, how the proposed approach can be used both to tune the control system of the cycle, in case of off-design conditions, and in the design phase of the cycle itself, when different configurations have to be analyzed in order to find the best compromise between system layout, working conditions and cost.

Conclusions

Organic Rankine cycle (ORC) systems are a way to convert thermal power into mechanical, or electrical, one using an organic fluid in place of water, which is employed in conventional Rankine cycle. This allows to exploit thermal sources characterized by low temperature and low available thermal power, such as the heat rejected from the flue gases of an engine or a turbine. While systems characterized by a power of the order of hundreds or thousands of kW are already diffused in the global market, the ones which produce a net power output of the order of 10 kWe still represent a niche, mainly because of their high cost-per-kW, which prevents their diffusion in the market composed by small activities and private house landlords. On the other hand, in the last years the interest in these micro systems is increasing because of environmental concerns and to improve the efficiency of power production. For this reason, it is important to understand how to improve the performance of the systems belonging to this power range and, to do so, two paths can be followed: one is by studying system behavior on an experimental test rig, the other is by running simulations of the components of which the performance has to be assessed. However, there are times in which an experimental test stand cannot be set up or when, for example, it is not possible or safe to study off-design conditions of a system component. Because of this, Computational Fluid Dynamics (CFD) simulations can be of aid in predicting how a certain device behaves when subjected to certain operating conditions. One problem of such approach is that, usually, it is possible to simulate just a single component at a time, not being able to study the mutual interaction between the cycle components during system operation.

Trying to overcome this issue, in the present thesis a numerical method has been proposed but first, the results of a preliminary measurement campaign which has been conducted on a prototypal micro-ORC system have been reported. This test campaign allowed to understand which is one of the phenomena which has the most detrimental effects on system power output, namely fluid leakage across the gaps of the expander. The prototypal, expansion machine was a scroll expander since, for small power output (as in the case here reported, where the expected output power was 1 kWe), positive displacement expanders show some

advantages over dynamic machines, such as a lower cost, a lower rotational speed and a greater capability in handling a certain mass fraction of liquid at the end of the expansion phase. Because of the expander prototypal nature, it has not been possible to test the machine at the nominal rotational speed of 3600 rpm, but its behavior has been studied up to the speed of 2700 rpm. Even if the machine has been tested in this limited range of speeds, it has been possible to notice how the limited electric power generated by the expander is probably given by the great amount of fluid which leaks from the flank and axial gaps, information given by a value for the filling factor greater than two for the highest rotational speed.

With this result in mind, in the current thesis it has then been proposed a method to simulate, by means of CFD analyses, the behavior of an entire ORC system. At first, to assess the feasibility of such a simulation in terms of obtainable results and required computational power, a simplified cycle have been proposed, which represents the Whole ORC modeling (WOM) concept. Thanks to this simplified model, it has been possible to notice how all the properties of interest, such as pressure and temperature distributions in the heat exchangers can be calculated but, more importantly, also the effects of the pipes connecting the various devices, such as the pressure losses, can be taken into account with a reasonable computational time to run the simulation. Since this model provided encouraging results, this concept was further developed to simulate a portion of a real cycle, without simplifying the geometry of the various components. In doing so, it has been possible to study the effects of pressure pulsations induced by the pump on the components placed upstream and downstream to it, namely the Coriolis mass flow meter and the liquid regenerator. Thanks to the WOM approach, it was also possible to compare the frequency of the force acting on the Coriolis flow meter with its resonance one, giving an important information to the system designer. It is then clear how the WOM method as a great potential in indicating the interaction between the various system devices, but there are cases in which the available computational resources are not sufficient to model also the behavior of the fluid flowing inside the ducts connecting the various system components, or cases in which the user is not interested in this type of modeling and need an easier approach to numerically “connect” the various components. In fact, CFD simulations are also useful to study in great detail the phenomena which happens inside the various components of the cycle, such fluid recirculation or leakages. For this reason, several numerical simulations of the single components have been run, and the results have been shown in this thesis. Two types of expanders have been studied, the single-screw machine and the scroll expander, and a model of an evaporator has been implemented to study the heat exchange taking place through it.

This latter simulation showed how CFD can give information such as the mass fraction of liquid at the outlet port of the evaporator, condition that can happen if the temperature of the heat source steeply decreases and the ORC control system does not detect this variation. Moreover, the information about the state of the refrigerant at the outlet of the exchanger can be transferred to the expander, also when adopting the non-full 3D WOM approach. In fact, information such the one just reported, or as the mass fraction of oil entering the machine to lubricate it, can be used to set up the simulation of the expander. In this thesis, both the simulations of the scroll expanders have been run without injecting any type of liquid, showing how the absence of this phase lead to great values for the leakage flow through the axial and flank gaps. In the case of the Oldham-ring scroll expander, not having run a multiphase simulation, it has been possible to use the available computational power to model also the movement of the Oldham ring, which partially and constantly occluded part of the outlet port during a complete revolution of the moving spiral. In this way, fluid recirculation at the exhaust of the machine has been observed, together with great values for the Filling Factor, because of the absence of oil modeling. This is true also in the case of the simulated single-screw expander: when studied without the oil injection, pressure evolution inside the expander was influenced by the presence of these unsealed gaps. In order to analyze the behavior of the single-screw expander when lubricant is injected as droplets of different dimensions through the inlet of the machine, a simulation was run modeling the interaction between the liquid phase and the refrigerant with the Eulerian – Lagrangian model. This simulation has shown how both the geometry of the machine and the size of the oil particles influences the way in which the oil is able to enter the expansion chamber, conditioning expander behavior.

All the properties measured at the outlet of the simulated machines and heat exchanger can be used as the inlet boundary conditions of each component placed downstream of them thanks to the last WOM approach which has been shown in this work. A Python script has been written to do so, during runtime, for simulations run also with different CFD software, in order to couple the various components of the cycle without the need of user intervention and when the effect of pipes, valves and fittings on the fluid flow is not required of being modeled.

In the future, the WOM approach based on the Python can be improved by introducing the 0D modeling of these components, to take into account the concentrated or distributed head losses for the fluid flowing between the main cycle components. Another improvement could be to parallelize the execution of the various simulations, but the resulting computational

load on the numerical host has to be carefully assessed, not to decrease the performance with respect to the case of a serial run.

Acknowledgements

I want to thank my supervisor, Professor Michele Pinelli, for having given me the opportunity to improve my knowledge in this field of mechanical engineering.

I've been lucky to spend almost six months of my life studying at the Purdue University, so a big thank goes to Professors Eckhard Groll and Davide Ziviani, who made it possible. And of course, to my labmates: Cai, Danielle, Lennart, Leon, Nick, Riley and Xueyang.

I thank all the guys of the Fluid Machinery research group, especially Alessio and Nicola, who pushed (and pulled) me to go on with my work and the other mates who shared these years as a PhD student with me: Devid, Giulia and Lucia.

Last but not least, my family and my girlfriend Beatrice, who have always been there through good and bad times. Thank you.

References

- [1] International Energy Agency, CO2 emissions from fuel combustion, 2017.
- [2] IEA, [Online]. Available: <https://www.iea.org/statistics/co2emissions/>. [Viewed 1 10 2019].
- [3] NOAA, «Climate Change: Atmospheric Carbon Dioxide,» [Online]. Available: <https://www.climate.gov/news-features/understanding-climate/climate-change-atmospheric-carbon-dioxide>. [Viewed 4 10 2019].
- [4] O. Bailey e E. Worrell, «Sustainable development through waste heat recovery,» *American Journal of Environmental Sciences*, vol. 6, n. 1, pp. 83-89, 2010.
- [5] BSC, Inc., Waste Heat Recovery: Technology and Opportunities in U.S. Industry, 2008.
- [6] L. Tocci, T. Pal, I. Pasmazoglou e B. Franchetti, «Small Scale Organic Rankine Cycle (ORC): a Techno-Economic Review,» *Energies*, vol. 10, n. 413, 2017.
- [7] F. Ofeldt, «Engine». Brevetto US611792A, 1898.
- [8] H. Tabor e L. Bronicki, «Small turbine for solar energy power package,» in *Proc. U.N. Conf. On New Sources of Energy*, Rome, 1961.
- [9] BorgWarner, «Converting Waste Heat into Electrical Energy: BorgWarner's Organic Rankine Cycle,» [Online]. Available: <https://www.borgwarner.com/newsroom/press-releases/2018/09/13/converting->

- waste-heat-into-electrical-energy-borgwarner-s-organic-rankine-cycle. [Viewed 23 10 2019].
- [10] G. Żywica, T. Kaczmarczyk, E. Ichnatowicz e T. Turzy, «Experimental investigation of the domestic CHP ORC system in transient operating conditions,» *Energy Procedia*, vol. 129, pp. 637-643, 2017.
- [11] M. Farrokhi, S. Noie e A. Akbarzadeh, «Preliminary experimental investigation of a natural gas-fired ORC-based micro-CHP system for residential buildings,» *Applied Thermal Engineering*, vol. 69, pp. 221-229, 2014.
- [12] G. Qiu, Y. Shao, J. Li, H. Liu e S. Riffat, «Experimental investigation of a biomass-fired ORC-based micro-CHP for domestic applications,» *Fuel*, n. 96, pp. 374-382, 2012.
- [13] Nucleo Investigativo Antincendi, «Le cause d'incendio e/o di esplosione nelle caldaie e generatori di calore in ambienti domestici,» 2016.
- [14] M. Orosz e R. Dickes, «Solar thermal powered Organic Rankine Cycles,» in *Organic Rankine Cycle (ORC) Power Systems*, Elsevier, 2017, pp. 564-606.
- [15] K. Lovegrove e W. Stein, *Concentrating Solar Power Technology*, Elsevier, 2012.
- [16] S. Quoilin, *Sustainable energy conversion through the use of Organic Rankine Cycles for waste heat recovery and solar applications*, 2011.
- [17] S. Lecompte, H. Huisseune, M. van der Broek, B. Vanslambrouck e M. De Paepe, «Review of organic Rankine cycle (ORC) architectures for waste heat recovery,» *Renewable and Sustainable Energy Reviews*, n. 47, pp. 448-461, 2015.
- [18] G. Bianchi, R. McGinty, D. Oliver, D. Brightman, O. Zaher, S. Tassou, J. Miller e H. Jouhara, «Development and analysis of a packaged Trilateral Flash Cycle system for low grade heat to power conversion applications,» *Thermal Science and Engineering Progress*, vol. 4, pp. 113-121, 2017.
- [19] B. Saleh, G. Koglbauer, M. Wendland e J. Fischer, «Working fluids for low-temperature organic Rankine cycles,» *Energy*, vol. 32, n. 7, pp. 1210-1221, 2007.

- [20] N. Yamada, M. Watanabe e A. Hoshi, «Experiment on pumpless Rankine-type cycle with scroll expander,» *Energy*, vol. 49, pp. 137-145, 2013.
- [21] P. Gao, L. Wang, R. Wang, L. Jiang e Z. Zhou, «Experimental investigation on a small pumpless ORC (organic rankine cycle) system driven by the low temperature heat source,» *Energy*, vol. 91, pp. 324-333, 2015.
- [22] Multiple Authors, *Organic Rankine Cycle (ORC) Power Systems - Technologies and Applications*, Elsevier, 2017.
- [23] R. K. Shah e D. P. Sekulic, *Fundamentals of Heat Exchanger Design*, John Wiley & Sons, Inc., 2003.
- [24] M. Khan e A. Fartaj, «A review on Microchannel Heat Exchangers and Potential Applications,» *International Journal of Energy Research*, vol. 35, 2011.
- [25] L. Branchini, A. De Pascale e A. Peretto, «Systematic comparison of ORC configurations by means of comprehensive performance indexes,» *Applied Thermal Engineering*, vol. 61, n. 2, pp. 129-140, 2013.
- [26] J. Bao e L. Zhao, «A review of working fluid and expander selections for organic Rankine cycle,» *Renewable and Sustainable Energy Reviews*, 2013.
- [27] F. Hellstrom, «Numerical computations of the unsteady flow in a radial turbine,» Royal Institute of Technology, Stockholm, 2008.
- [28] V. Lemort e A. Legros, «Positive displacement expanders for Organic Rankine Cycle system,» in *Organic Rankine Cycle (ORC) Power Systems*, Elsevier, 2017, pp. 360-395.
- [29] E. Georges, S. Declaye, O. Dumont, S. Quoilin e V. Lemort, «Design of a small-scale organic Rankine cycle engine used in a solar power plant,» *International Journal of Low-Carbon Technologies*, pp. 1-8, 2013.

- [30] T. Matsumoto e I. Chabu, «Study of losses in permanent magnet couplings due to highly conductive walls,» in *2014 International Conference on Electrical Machines (ICEM)*, Berlin, 2014.
- [31] J. Wennemar, «Dry screw compressor performance and application range,» in *Thirty-eighth turbomachinery symposium*, Houston, TX, 2009.
- [32] D. Richfield, Artist, [Art]. CC BY-SA 4.0, 2016.
- [33] B. Zimmern e G. C. Patel, «Design and Operating Characteristics of the Zimmern Single Screw Compressor,» in *International Compressor Engineering Conference*, West Lafayette, IN, 1972.
- [34] D. Ziviani, S. Gusev, S. Lecompte, E. Groll, J. Braun e W. Horton, «Characterizing the performance of a single-screw expander in a small-scale organic Rankine cycle for waste heat recovery,» *Applied Energy*, vol. 181, pp. 155-170, 2016.
- [35] Y.-Q. Zhang, Y.-T. Wu, G.-D. Xia, C.-F. Ma, W.-N. Ji, S.-W. Liu, K. Kang e F.-B. Yang, «Development and experimental study on organic Rankine cycle system with single-screw expander for waste heat recovery from exhaust of diesel engine,» *Energy*, vol. 77, pp. 499-508, 2014.
- [36] O. Badr, P. O'Callaghan, M. Hussein e S. Probert, «Multi-vane expanders as prime movers for low-grade energy organic Rankine-cycle engines,» *Applied Energy*, vol. 16, n. 2, pp. 129-146, 1984.
- [37] G. Jacazio, B. Piombo, A. Romiti e A. Sola, «The optimisation of the performance of vane-type air motors,» in *Proceedings of the Fifth World Congress on Theory of Machines and Mechanisms*, Montreal, 1979.
- [38] G. Zywica, T. Zygmunt Kaczmarczyk e E. Ihnatowicz, «A review of expanders for power generation in small-scale organic Rankine cycle systems: Performance and operational aspects,» *J Power and Energy*, pp. 1-16, 2016.

- [39] R. Daccord, J. Melis, T. Kientz, A. Darmedru, R. Pireyre, N. Brisseau e E. Fontaneau, «Exhaust heat recovery with Rankine piston expander,» in *ICE Powertrain Electrification and Energy Recovery*, 2013.
- [40] S. Quoilin, M. Van Der Broek, S. Declaye, P. Dewallef e V. Lemort, «Techno-economic survey of Organic Rankine Cycle (ORC) systems,» *Renewable and Sustainable Energy Reviews*, vol. 22, pp. 168-186, 2013.
- [41] R. Bracco, D. Micheli, R. Petrella, M. Reini, R. Taccani e G. Toniato, «Micro-Organic Rankine Cycle systems for domestic cogeneration,» in *Organic Rankine Cycle (ORC) Power Systems*, Elsevier, 2017, pp. 633-633.
- [42] I. Kenneth Smith, N. Stosic, A. Kovacevic e R. Langson, «Cost effective small scale ORC systems for power recovery from low enthalpy geothermal resources,» in *Geothermal Resources Council*, 2007.
- [43] S. Declaye, Design, optimization and modeling of an organic Rankine cycle for waste heat recovery, Liège: Université de Liège, 2009.
- [44] S. Clemente, D. Micheli e R. Radu, «Experimental tests on a gear pump for organic Rankine cycle applications,» in *Proceedings of The 3rd edition of the International Conference on Microgeneration*, Napoli, 2013.
- [45] B. Aoun, Micro combined heat and power operating on renewable energy for residential building, ECOLE NATIONALE SUPERIEURE DES MINES DE PARIS, 2008.
- [46] T. Hung, «Waste heat recovery of organic Rankine cycle using dry fluids,» *Energy Conversion and Management*, n. 42, pp. 539-553, 2001.
- [47] V. Maizza e A. Maizza, «Unconventional working fluids in organic Rankine-cycles for waste energy recovery systems,» *Applied Thermal Engineering*, n. 21, pp. 381-390, 2001.
- [48] J. Larjola, «Electricity from industrial waste heat using high-speed organic Rankine cycle (ORC),» *ELSEVIER Int. J. Production Economics*, n. 41, pp. 227-235, 1995.

- [49] ECHA, «Inclusion of substances of very high concern in the Candidate List for eventual inclusion in Annex XIV,» Helsinki, 2018.
- [50] P. Mago, K. Srinivasan, L. Chamra e C. Somayaji, «An examination of exergy destruction in organic Rankine cycles,» *International Journal of Energy Research*, vol. 32, n. 10, pp. 926-938, 2008.
- [51] A. Lavernia, *Micro-Scale Waste Heat Recovery from Stationary Internal Combustion Engines by Sub-Critical Organic Rankine Cycle Utilizing Scroll Machinery*, West Lafayette: Purdue University, 2018.
- [52] I. Bell, J. Wronski, S. Quoilin e V. Lemort, «Pure and Pseudo-pure Fluid Thermophysical Property Evaluation and the Open-Source Thermophysical Property Library CoolProp,» *Ind. Eng. Chem. Res.*, vol. 53, n. 6, pp. 2498-2508, 2014.
- [53] L. R. Inglis, «Air flow amplifier». Brevetto US4046492A, 21 01 1976.
- [54] Brauer Clamps USA, «Brauer Airmovers: Airmovers Explained,» [Online]. Available: <http://www.brauerclampsusa.com/php/airmoveroverview.php>. [Viewed 28 10 2019].
- [55] E. Winandy, C. Saavedra e J. Lebrun, «Experimental analysis and simplified modeling of a hermetic scroll refrigeration compressor,» *Applied Thermal Engineering*, vol. 22, pp. 107-120, 2002.
- [56] Baldor Reliance, «EM3550 datasheet,» 2010.
- [57] R. Bracco, S. Clemente, D. Micheli e M. Reini, «Experimental tests and modelization of a domestic-scale ORC (OrganicRankine Cycle),» *Energy*, vol. 58, pp. 107-116, 2013.
- [58] R. Zanelli e D. Favrat, «Experimental Investigation of a Hermetic Scroll Expander-Generator,» in *International Compressor Engineering Conference*, Purdue, 1994.

- [59] W. Donghong, L. Xuesheng, L. Zhen e G. Jianming, «Dynamic modeling and simulation of an Organic Rankine Cycle (ORC) system for waste heat recovery,» *Applied Thermal Engineering*, n. 28, pp. 1216-1224, 2008.
- [60] R. Dickes, O. Dumont, R. Daccord, S. Quoilin e V. Lemort, «Modelling of organic Rankine cycle power systems in off-design conditions: an experimentally-validated comparative study,» *Energy*, n. 123, pp. 710-727, 2017.
- [61] Z. Miao, J. Xu e K. Zhang, «Experimental and modeling investigation of an organic Rankine cyclesystem based on the scroll expander,» *Energy*, n. 134, pp. 35-49, 2017.
- [62] S. Quoilin, V. Lemort e J. Lebrun, «Experimental study and modeling of an Organic Rankine Cycle using scroll expander,» *Applied Energy*, n. 87, pp. 1260-1268, 2010.
- [63] B. Xu, D. Rathod, S. Kulkarni, A. Yebi, Z. Filipi, S. Onori e M. Hoffman, «Transient dynamic modeling and validation of an organic Rankine cyclewaste heat recovery system for heavy duty diesel engine applications,» *Applied Energy*, n. 205, pp. 260-279, 2017.
- [64] W. R. Huster, Y. Vaupel, A. Mhamdi e A. Mitsos, «Validated dynamic model of an organic Rankine cycle (ORC) for wasteheat recovery in a diesel truck,» *Energy*, n. 151, pp. 647-661, 2018.
- [65] M. Ancona, M. Bianchi, L. Branchini, A. De Pascale, F. Melino, V. Orlandini, S. Ottaviano, A. Peretto , M. Pinelli, P. Spina e A. Suman, «A Micro-ORC Energy System: Preliminary Performance and Test Bench Development,» *Energy Procedia*, n. 101, pp. 814-821, 2016.
- [66] M. Bianchi, L. Branchini, A. De Pascale, V. Orlandini, S. Ottaviano, M. Pinelli, P. R. Spina e A. Suman, «Experimental Performance of a Micro-ORC Energy System for Low Grade Heat Recovery,» *Energy Procedia*, vol. 129, pp. 899-906, 2017.
- [67] M. Bianchi, L. Branchini, A. De Pascale, V. Orlandini, S. Ottaviano, A. Peretto, F. Melino, M. Pinelli, P. Spina e A. Suman, «Experimental Investigation with Steady-State Detection in a Micro-ORC Test Bench,» *Energy Procedia*, n. 126, pp. 469-476, 2017.

- [68] C. Hirt e B. Nichols, «Volume of fluid (VOF) method for the dynamics of free boundaries,» *Journal of Computational Physics*, vol. 1, n. 39, pp. 201-225, 1981.
- [69] P. Spalart e S. Allmaras, «One-Equation Turbulence Model for Aerodynamic Flows,» in *30th Aerospace Sciences Meeting and Exhibit*, Reno, USA, 1992.
- [70] E. Lemmon, M. McLinden e M. Huber, «NIST Standard Reference Database 23 - NIST Thermodynamic and Transport Properties REFPROP, Version 7.0,» 2002.
- [71] N. Casari, E. Fadiga, M. Pinelli, S. Randi e A. Suman, «Pressure Pulsation and Cavitation Phenomena in a Micro-ORC System,» *Energies*, vol. 12, 2019.
- [72] D. del Campo, R. Castilla, G. Raush, P. Gamez Montero e E. Codina, «Numerical Analysis of External Gear Pumps Including Cavitation,» *Journal of Fluids Engineering*, vol. 8, n. 134, 2012.
- [73] M. Battarra e E. Mucchi, «Incipient cavitation detection in external gear pumps by means of vibro-acoustic measurements,» *Measurement*, n. 129, pp. 51-61, 2018.
- [74] G. Vetter e S. Notzon, «Effect of pulsating flow on Coriolis mass flowmeters,» *Flow Measurement and Instrumentation*, n. 5, pp. 263-273, 1994.
- [75] R. Cheesewright, C. Clark e Y. Hou, «The response of Coriolis flowmeters to pulsating flows,» *Flow Measurement and Instrumentation*, n. 15, pp. 59-67, 2004.
- [76] T. Wang e R. Baker, «A review of developments over the past 20 years, and an assessment of the state of the art and likely future directions.,» *Flow Measurement and Instrumentation*, n. 40, pp. 99-123, 2014.
- [77] E. Mucchi, G. Dalpiaz e A. Rivola, «Dynamic behavior of gear pumps: Effect of variations in operational and design parameters,» *Meccanica*, n. 46, pp. 1191-1212, 2011.
- [78] M. Bianchi, L. Branchini, N. Casari, A. De Pascale, F. Melino, S. Ottaviano, M. Pinelli, P. Spina e A. Suman, «Experimental analysis of a micro-ORC driven by

- piston expander for low-grade heat recovery,» *Applied Thermal Engineering*, n. 148, pp. 1278-1291, 2019.
- [79] Simerics, Inc., PumpLinx's User Manual - V 4.6.4, Bellevue, WA, USA, 2018.
- [80] Siemens, STAR-CCM+ 13.02 User's Manual, 2018.
- [81] A. Suman, S. Randi, N. Casari, M. Pinelli e L. Nespoli, «Experimental and Numerical Characterization of an Oil-Free Scroll Expander,» *Energy Procedia*, vol. 129, pp. 403 - 410, 2017.
- [82] Ansys, Inc., ANSYS Fluent Theory Guide, Release 15.0, 2013.
- [83] A. Suman, C. Buratto, N. Aldi, M. Pinelli, P. Spina e M. Morini, «A Comparison Between Two Different CFD Approaches of a Real Scroll Expander for Micro-ORC Applications,» in *3rd International Seminar on ORC Power Systems*, 2015.
- [84] S. Randi, N. Casari, E. Fadiga, A. Suman, M. Pinelli, E. Groll, D. Ziviani e B. Shaffer, «Verification of a 3D-CFD model of an Oldham ring scroll expander,» in *5th International Seminar on ORC Power Systems*, Athens, 2019.
- [85] S. Randi, A. Suman, N. Casari, M. Pinelli e D. Ziviani, «Numerical analysis of oil injection effects in a single screw expander,» in *International Conference on Screw Machines*, Dortmund, 2018.
- [86] M. De Paepe, W. Bogaert e D. Mertens, «Cooling of oil injected screw compressors by oil atomisation,» *Applied Thermal Engineering*, vol. 25, n. 17-18, pp. 2764-2779, 2005.
- [87] D. Ziviani, S. Gusev, S. Lecompte, E. Groll, J. Braun, W. Horton, M. van der Broek e M. De Paepe, «Optimizing the performance of small-scale organic Rankine cycle that utilizes a single-screw expander,» *Applied Energy*, vol. 189, pp. 416-432, 2017.
- [88] T. Bein e J. Hamilton, «Computer Modeling of an Oil Flooded Single Screw Air Compressor,» in *International Compressor Engineering Conference*, West Lafayette, 1982.

- [89] T. Hotta, T. Inoue, M. Matsuda e M. Ueda, «Measurement of Oil Film between Swash Plate and Shoe for Swash Plate Type Compressor,» in *International Compressor Engineering Conference*, West Lafayette, 2004.
- [90] K. Minami, H. Hattori e M. Hayano, «Lubrication analysis of rotary compressors for HFC refrigerants,» in *International Compressor Engineering Conference*, West Lafayette, 1998.
- [91] B. Whitman, B. Johnson, J. Tomczyk e E. Silberstein, *Refrigeration and air conditioning technology*, Cengage Learning, 2012.
- [92] V. Zhelezny, Y. Semenyuk, S. Ancherbak, A. Grebenkov e O. Beliayeva, «An experimental investigation and modelling of the solubility, density and surface tension of 1, 1, 1, 3, 3-pentafluoropropane (R-245fa)/synthetic polyolester compressor oil solutions,» *Journal of Fluorine Chemistry*, vol. 128, n. 9, pp. 1029-1038, 2007.
- [93] D. Ziviani, I. Bell, M. De Paepe e M. van der Broek, «Mechanistic model of an oil-flooded single-screw expander,» in *International Compressor Engineering Conference*, West Lafayette, 2016.
- [94] D. Ziviani, A. Suman, J. Gabrielloni, M. Pinelli e M. De Paepe, «CFD Approaches Applied to A Single-Screw Expander,» in *International Compressor Engineering Conference*, West Lafayette, 2016.
- [95] M. Friedrich, H. Lan, J. Wegener, A. Drallmeier e B. Arnaly, «A Separation Criterion With Experimental Validation for Shear-Driven Films in Separated Flows,» *Journal of Fluids Engineering*, vol. 130, n. 5, 2008.
- [96] F. Maroteaux, D. Llory, J.-F. Le Coz e C. Habchi, «Liquid Film Atomization on Wall Edges—Separation Criterion and Droplets Formation Model,» *journal of Fluids Engineering*, vol. 124, n. 3, pp. 565-575, 2002.
- [97] F. Menter, «Two-equation eddy-viscosity turbulence models for engineering applications,» *AIAAJ*, vol. 32, n. 8, 1994.

- [98] N. Stošić, L. Milutinović, K. Hanjalić e A. Kovačević, «Investigation of the influence of oil injection upon the screw compressor working process,» *International Journal of Refrigeration*, vol. 15, n. 4, pp. 206-220, 1992.
- [99] N. Casari, A. Suman, D. Ziviani, M. van der Broek, M. De Paepe e M. Pinelli, «Computational models for the analysis of positive displacement machines: real gas and dynamic mesh,» *Energy Procedia*, vol. 129, pp. 411-418, 2017.
- [100] A. Suman, D. Ziviani, J. Gabrielloni, M. Pinelli, M. De Paepe e M. van der Broek, «Different Numerical Approaches for the Analysis of a Single Screw Expander,» *Energy Procedia*, vol. 101, pp. 750-757, 2016.
- [101] K. Edge e J. Darling, «Cylinder Pressure Transients in Oil Hydraulic Pumps with Sliding Plate Valves,» *Proceedings of the Institution of Mechanical Engineers, Part B: Journal of Engineering Manufacture*, vol. 200, n. 1, pp. 45-54, 1986.
- [102] Siemens, AMESim Rev 13 Reference guide, Roanne, 2014.
- [103] C. Bell, «fluids: Fluid dynamics component of Chemical Engineering Design Library (ChEDL),» 2016-2018. [Online]. Available: <https://github.com/CalebBell/fluids>. [Viewed 11 10 2019].
- [104] G. van Rossum, «Python tutorial, Technical Report CS-R9526,» Centrum voor Wiskunde en Informatica (CWI), Amsterdam, 1995.
- [105] Indiana University, «About batch jobs,» [Online]. Available: <https://kb.iu.edu/d/afrx>. [Viewed 15 10 2019].
- [106] T. Ho, Advanced Organic Vapor Cycles for Improving Thermal Conversion Efficiency in Renewable Energy Systems, University of California, Berkeley, 2012.
- [107] V. Lemort, I. Teodorese e J. Lebrun, «Experimental study of the integration of a scroll expander into a heat recovery Rankine cycle,» in *18th International Compressor Engineering Conference*, West Lafayette, 2006.

[108] M. Astolfi, «Technical options for Organic,» in *Organic Rankine Cycle (ORC) Power Systems*, 2017, pp. 76-98.

Appendix A – Python script

Note: file paths have been shortened.

```
#!/usr/bin/python

import csv
import re
import fileinput
import subprocess

n=0
t=0.0
dt=1e-5
endTime=2e-5
while t < endTime:

    #reading pressure and temperature values at the outlet of the
    condenser
    with open('../pliqout.csv','r') as pliqOut:
        csv_reader=csv.reader(pliqOut)
        line_count=0
        for row in csv_reader:
            if line_count==0:
                line_count+=1
            else:
                pliq_out=float(row[1])
                line_count+=1
    with open('../Tliqout.csv','r') as TliqOut:
        csv_reader=csv.reader(TliqOut)
        line_count=0
        for row in csv_reader:
            if line_count==0:
                line_count+=1
            else:
                Tliq_out=float(row[1])
                line_count+=1

    #setting evaporator wall temperature
    wallT=480

    #simulating pump
    pliq_in=(pliq_out+1e6)/1e5
    Tliq_in=Tliq_out+1

    dtStr=str(dt)
    wallT_str=str(wallT)
```

```

    pliq_in_str=str(pliq_in)
    Tliq_in_str=str(Tliq_in)

    dt_evapString="..."
    wallT_evapString="..."
    pIn_evapString="..."
    TIn_evapString="..."

    dt_evapNew=re.sub("setValue","setValue("+dtStr+");",dt_evapString)
    wallT_evapNew=re.sub("setValue","setValue("+wallT_str+");",wallT_evapString)
    pIn_evapNew=re.sub("setValue","setValue("+pliq_in_str+");",pIn_evapString)
    TIn_evapNew=re.sub("setValue","setValue("+Tliq_in_str+");",TIn_evapString)

    evap_macro='evap_macro.java'

    #replacing values for pressure and temperature of the working
    fluid, plus wall temperature and time-step
    for line in fileinput.input(evap_macro, inplace=True):
        if pIn_evapString in line:
            print(pIn_evapNew).rstrip('\n')
        elif TIn_evapString in line:
            print(TIn_evapNew).rstrip('\n')
        elif wallT_evapString in line:
            print(wallT_evapNew).rstrip('\n')
        elif dt_evapString in line:
            print(dt_evapNew).rstrip('\n')
        else:
            print (line).rstrip('\n')

    #launching the evaporator simulation
    subprocess.call("../Evaporator.sim",shell=True)

    #reading pressure and temperature values at the outlet of the
    evaporator
    with open('../pressuregasout.csv','r') as pgas_evOut:
        csv_reader=csv.reader(pgas_evOut)
        line_count=0
        for row in csv_reader:
            if line_count==0:
                line_count+=1
            else:
                pgas_expIn=row[1]
                line_count+=1
    with open('../temperaturegasout.csv','r') as Tgas_evOut:
        csv_reader=csv.reader(Tgas_evOut)
        line_count=0
        for row in csv_reader:
            if line_count==0:
                line_count+=1
            else:
                Tgas_expIn=row[1]
                line_count+=1

```



```

boundary='boundary.in'
inputs='inputs.in'

pgas_expIn_String=str(pgas_expIn)
Tgas_expIn_String=str(Tgas_expIn)

exp_pres_init_string="pressure    ..."
exp_temp_init_string="temperature  ...  "

p_inlet_exp_new=re.sub("pressure    ...", "pressure    ...
["+pgas_expIn_String+"]", exp_pres_init_string).rstrip(['\n'])
T_inlet_exp_new=re.sub("temperature  ...", "temperature
..." + Tgas_expIn_String + "", exp_temp_init_string)

#changing pressure and temperature values at the inlet of the
expander
for line in fileinput.input(boundary, inplace=True):
    if exp_pres_init_string in line:
        print(p_inlet_exp_new).rstrip('\n')
    elif exp_temp_init_string in line:
        print(T_inlet_exp_new).rstrip('\n')
    else:
        print (line).rstrip('\n')

start_time_init_string="start_time    ..."
end_time_init_string="end_time    ..."

et=t+dt
starttimeStr=str(t)
endtimeStr=str(et)

start_time_new=re.sub("start_time", "" + starttimeStr + "
start_time", start_time_init_string)
end_time_new=re.sub("end_time", "" + endtimeStr + "
end_time", end_time_init_string)

textwrite_init_string="twrite_files    ..."
textwrite_new=re.sub("twrite_files", "" + dtStr + "
twrite_files", textwrite_init_string)

restart_init_string="restart_number    ..."
res_flag_init_string="restart_flag    ..."
restartnumStr=str(n)
oneval=str(1)
zeroval=str(0)

restart_new=re.sub("restart_number", "" + restartnumStr + "
restart_number", restart_init_string)

#checking if the simulation is a new run or a restart
if n<>0:
    res_flag_new=re.sub("restart_flag", "" + oneval + "
restart_flag", res_flag_init_string)
else:
    res_flag_new=re.sub("restart_flag", "" + zeroval + "
restart_flag", res_flag_init_string)

```

```

#replacing the values in the inputs.in file
for line in fileinput.input(inputs, inplace=True):
    if start_time_init_string in line:
        print(start_time_new).rstrip('\n')
    elif end_time_init_string in line:
        print(end_time_new).rstrip('\n')
    elif textwrite_init_string in line:
        print(textwrite_new).rstrip('\n')
    elif restart_init_string in line:
        print (restart_new).rstrip('\n')
    elif res_flag_init_string in line:
        print (res_flag_new).rstrip('\n')
    else:
        print (line).rstrip('\n')

#running the expander simulation
subprocess.call("... converge-2.4.24-mpich",shell=True)

#reading pressure and temperature values at the outlet port of
the expander
if t==0:
    with open("area_avg_flow.out", "r") as AreaexpOutData:
        lines=expOutData.readlines()
        tempResult=[]
        for x in lines:
            tempResult.append(x.split()[12])
else:
    with open("area_avg_flow%s.out" % (n), "r") as
AreaexpOutData:
        lines=expOutData.readlines()
        tempResult=[]
        for x in lines:
            tempResult.append(x.split()[12])

if t==0:
    with open("mass_avg_flow.out", "r") as MassexpOutData:
        lines=expOutData.readlines()
        presResult=[]
        for x in lines:
            presResult.append(x.split()[10])
else:
    with open("mass_avg_flow%s.out" % (n), "r") as
MassexpOutData:
        lines=expOutData.readlines()
        presResult=[]
        for x in lines:
            presResult.append(x.split()[10])

condMacro='cond_macro.java'

pgas_cond_in_str=str(presResult[5])
Tgas_cond_in_str=str(tempResult[5])

dt_condString="..."
pin_condString="..."
Tin_condString="..."

```

```

        dt_condNew=re.sub("setValue","setValue("+dtStr+");",dt_condString)
        pin_condNew=re.sub("setValue","setValue("+pgas_cond_in_str+")",pin_condString)
        Tin_condNew=re.sub("setValue","setValue("+Tgas_cond_in_str+")",Tin_condString)

        #replacing the values for pressure and temperature in the condenser macro
        for line in fileinput.input(condMacro, inplace=True):
            if pin_condString in line:
                print(pin_condNew).rstrip('\n')
            elif Tin_condString in line:
                print(Tin_condNew).rstrip('\n')
            elif dt_condString in line:
                print(dt_condNew).rstrip('\n')
            else:
                print (line).rstrip('\n')

        #running condenser simulation
        subprocess.call("../Condenser.sim",shell=True)

        t=t+dt
        n=n+1
        #user message
        print ("-----")
        print ("End of iteration number %s, next simulation time %s s"
%(n-1,t))
        print ("-----")

```


Appendix B – Java script

Note: file paths have been shortened.

```
// Written by Saverio Randi, based on STAR-CCM+ 13.02.011 macro
package macro;

import java.util.*;

import star.common.*;
import star.base.neo.*;
import star.energy.*;
import star.flow.*;

public class cond_macro extends StarMacro {

    public void execute() {
        execute0();
        // ../Condenser.sim
    }

    private void execute0() {

        Simulation simulation_0 =
            getActiveSimulation();

        Region region_0 =
            simulation_0.getRegionManager().getRegion("Region");

        Boundary boundary_0 =
            region_0.getBoundaryManager().getBoundary("Body 1.inlet");

        PhaseConditions phaseConditions_0 =
            ((PhaseConditions)
            boundary_0.get(PhaseConditionsManager.class).getPhaseConditions("gas"));

        StaticTemperatureProfile staticTemperatureProfile_0 =

        phaseConditions_0.getPhaseValueManager().get(StaticTemperatureProfile.class);

        staticTemperatureProfile_0.getMethod(ConstantScalarProfileMethod.class).getQuantity().setValue(5.2315000e+02);

        TotalPressureProfile totalPressureProfile_0 =
```

```

        boundary_0.getValues().get(TotalPressureProfile.class);

totalPressureProfile_0.getMethod(ConstantScalarProfileMethod.class
).getQuantity().setValue(2.5000000e+05);

    ResidualPlot residualPlot_0 =
        ((ResidualPlot)
simulation_0.getPlotManager().getPlot("Residuals"));

ImplicitUnsteadySolver implicitUnsteadySolver_0 =
    ((ImplicitUnsteadySolver)
simulation_0.getSolverManager().getSolver(ImplicitUnsteadySolver.c
lass));

implicitUnsteadySolver_0.getTimeStep().setValue(1e-05);

    residualPlot_0.open();

simulation_0.getSimulationIterator().step(1);

    residualPlot_0.close();

    MonitorPlot monitorPlot_1 =
        ((MonitorPlot) simulation_0.getPlotManager().getPlot("Outlet
Pressure "));

    monitorPlot_1.export(resolvePath("../pliqout.csv"), ",");

    MonitorPlot monitorPlot_0 =
        ((MonitorPlot) simulation_0.getPlotManager().getPlot("Outlet
Temperature "));

    monitorPlot_0.export(resolvePath("../Tliqout.csv"), ",");

simulation_0.saveState("../Condenser.sim");
}
}

```